CDF/ANAL/EXOTIC/CDFR/10769
Version 1.5
February 24, 2012

A search for the Higgs boson in the all-hadronic channel using 9.45 fb^{-1} of CDF data

Ankush Mitra,Yen-Chu Chen,Song-Ming Wang [1]
Academia Sinica, Taiwan

Francesco Devoto [2]
Helsinki University, Finland

Abstract

This note documents the search for the Higgs boson in the all hadronic $W/ZH \to q\bar{q}b\bar{b}$ and $Hqq \to qqb\bar{b}$ mode. The search is performed on 9.45fb^{-1}of data recorded at CDF. As no signal was observed, 95% confidence limits are quoted for Higgs masses from 100 GeV/c^2 to 150 GeV/c^2.

[1]mitra@fnal.gov,chenyc@fnal.gov, smwang@fnal.gov
[2]francesco.devoto@helsinki.fi

Contents

1 Introduction

The Higgs boson plays a central role in the Standard Model as it endows particles with mass. Searches for the Higgs boson at CDF have concentrated on channels using combinations of leptons, jets and missing-Et. These channels have small background but also small Higgs signal yields. An alternative approach is to use the all jet final state which has the largest signal yield but has the challenge of modelling and suppressing a large QCD multijet background.

We search for a Higgs boson decaying to two bottom-quark jets ($b\bar{b}$) accompanied by two additional quark jets (qq') for Higgs masses $100 \leq m_H \leq 150\,\mathrm{GeV}/c^2$. The search is most sensitive to a Higgs boson with mass $< 135\,\mathrm{GeV}/c^2$ where the Higgs boson decay to $b\bar{b}$ is dominant [1]. The two production channels studied in this search are the associated production and vector boson fusion (VBF). The associated production, $p\bar{p} \to VH \to qq' + b\bar{b}$, where V is a W/Z vector boson which decays to a pair of quarks. The VBF channel, $p\bar{p} \to qq'H \to qq' + b\bar{b}$, where incoming partons each radiate a V and fuse to form a Higgs boson. Both production processes are illustrated in Fig. 1.

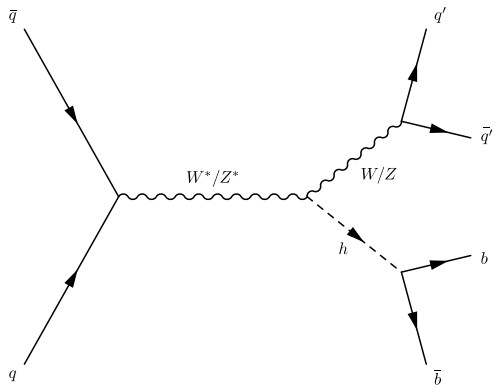

(a) Production and decay mode of the $VH \to b\bar{b}qq$ channel

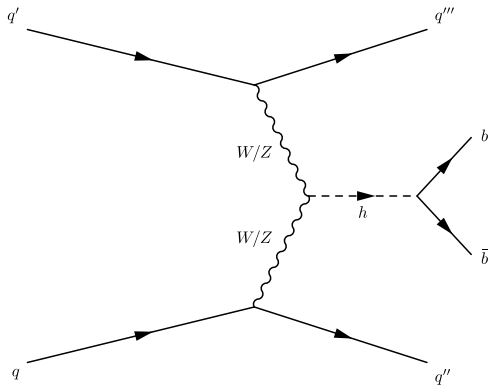

(b) Higgs boson production via vector boson fusion process.

Figure 1: Feynman diagrams for the two Higgs production channels studied in this ananlysis: Associated Vector Boson Production & Vector Boson Fusion.

This note describes the third iteration of the all-hadronic Higgs search using $9.45\,\mathrm{fb}^{-1}$of $p\bar{p}$ collision data at $\sqrt{s} = 1.96\,\mathrm{TeV}$ recorded by the CDF detector. Articles on the previous $2\,\mathrm{fb}^{-1}$and $4\,\mathrm{fb}^{-1}$search can be found at [2] [3] and references therein.

The additions and improvements to the analysis are:

- all CDF Run II data is analyzed which doubles the analyzed dataset from $4\,\mathrm{fb}^{-1}$to $9.45\,\mathrm{fb}^{-1}$.
- the b-jet energy resolution is improved using a neural network which combines information from the tracker, displaced vertex and calorimeter (Sec. 3).
- the QCD background prediction has been improved which allows more variables to be included in the neural network discriminant (Sec. 5).
- the jet moments, $\langle\eta\rangle$ and $\langle\phi\rangle$ are combined into a single jet-width measurement $\langle R\rangle$. The jet-width from the calorimeter and now the tracker are included. The corrections to remove kinematic and detector bias from the $\langle R\rangle$ measurement have been improved.
- a single unified signal region is used, rather than separate regions for VH and VBF, which improves the acceptance for Higgs boson.
- the neural network (NN) is improved by training a dedicated NN for each production process and then combining each network into a super-discrminant.

Table 1: Definition of the different versions of TOP_MULTI_JETand VH_MULTIJETand the recorded integrated luminosity. The integrated luminosity for TOP_MULTI_JETv-12 is the period before VH_MULTIJETwas added to the CDF trigger table.

	L1	L2	L2 Calorimeter Cluster algorithm	L3	Integrated Luminosity [fb^{-1}]
TOP_MULTIJET_v1-9	JET_20	L2_FOUR_JET15_SUMET175	PACMAN	4 Jet-15	2.364
TOP_MULTIJET_v-12	JET_20	L2_FOUR_JET15_SUMET175	L2CONE	4 Jet-15	0.643
VH_MULTIJET	JET_20	L2_THREEJET20_SUMET130	L2CONE	NULL	6.439

Table 2: The MC corrections for the multijet triggers. Any MC event passing the trigger is weighted by the MC scale factor.

Trigger	MC Scale Factor
TOP_MULTIJET_v-9	0.959 ± 0.034 (3.55%)
TOP_MULTIJET_v-12	1.024 ± 0.036 (3.55%)
VH_MULTIJET	1.014 ± 0.036 (3.55%)

2 Data and Trigger

The data for this analysis were collected by two triggers: TOP_MULTI_JET and VH_MULTIJET. They are designed to select events with 4 high p_T jets with large Sum-Et which are characteristic of an all hadronic Higgs event. The first $3.0\,\text{fb}^{-1}$of CDF data was collected by TOP_MULTI_JET trigger and the remaining $6.4\,\text{fb}^{-1}$ by VH_MULTIJET. The definition of the triggers and the recorded integrated luminosity are given in table 1.

The efficiency of the multijet triggers are senstive to the topology of the event which precludes the use of standard techniques of measuring the trigger turn-on from data; one has to rely on Monte Carlo (MC) simulation. A study of the multijet triggers was performed and a set of corrections were derived to correct the MC as documented in CDF Note 9954 [4]. This trigger study was repeated using a larger dataset and the latest version of STNTUPLE which includes the following changes:

- CDF Note 9954 includes a correction for L2 calorimeter cluster energy to compensate for a bug in TRIGSIM. This correction is no longer required as STNTUPLE now applies these correction on-the-fly.
- TOP_MULTI_JET_v1-8 and TOP_MULTI_JET_v-9 are no longer treated separately to simplify the trigger analysis. The trigger conditions for TOP_MULTI_JET_v-9 are applied to TOP_MULTI_JET_v1-8.
- the analysis event selection imposes a SumEt cut of $220\,\text{GeV}/c^2$ which is tighter than the L1_JET10 and L1_JET20 cut. So no dedicated L1 correction is required.
- the systematic uncertainty is measured using JET_70 and QCD-MC Pt60 rather than JET_20 and QCD-MC Pt18 as more events pass the trigger study quality cuts and thus a better measure of the systematic uncertainty.

The MC scale-factors used to weight MC events passing the trigger emulation are given in table 2.

2.1 Event Selection

2.1.1 PreTag Selection

The following criteria was applied for events to be considered in this analysis:

- The event must be in the QCD with Silicon Good Run List V45
- The event must have fired the TOP_MULTI_JET or VH_MULTI_JET trigger. For MC, the corrected trigger decision is used.
- The $|Z|$ position of the highest $P_T$class($\geq$12) vertex must be less than 60 cm.
- Event must have zero leptons (leptons are electrons and muons).
- The event's MET (missing transverse energy) significance [3] must be less than 6.
- The event must have 4 or 5 jets, where a jet is defined as:
  - 0.4 cone L7-corrected jet-Et $> 15.0\,\mathrm{GeV}$
  - 0.4 cone raw jet-Et $> 10.0\,\mathrm{GeV}$
  - Jet $|\eta| < 2.4$
- The jets passing the selection are ordered by descending b-jet corrected Et and any fifth jet is no longer used.
- The scalar L7-Et sum of the four leading jets (SumEt) $> 220\,\mathrm{GeV}/c^2$

2.1.2 B-Tagged Event Selection

Two b-tagging algorithms are used in this analysis:

- Tight SecVtx (SecVtx)
- 1% JetProb (JetProb)

If a jet is tagged by both b-tagging algorithms, SecVtx takes priority as it has a lower mistag rate. The two b-tagging algorithms are paired to define two b-tagging categories:

- SS: Exactly two jets are SecVtx tagged
- SJ: Exactly one jet is SecVtx tagged and exactly one jet is JetProb tagged.

The events which satisfy either b-tag category are labelled as b_1, b_2, q_1, q_2 where $b(q)$ are the tagged(untagged) jets and $E_T^{b_1/q_1} > E_T^{b_2/q_2}$.

Events with exactly 1 SecVtx tagged jet are used for the QCD background prediction.

- events with exactly 1 SecVtx tagged jet is used to predict the QCD SS background
- events with exactly 1 SecVtx tagged jet and zero JetProb tagged jets are used to predict the QCD SJ background

Further details on the QCD background prediction can be found in section 5.

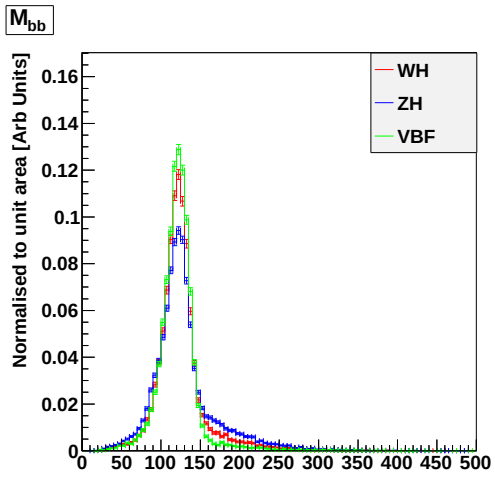

(a) m_{bb} distribution

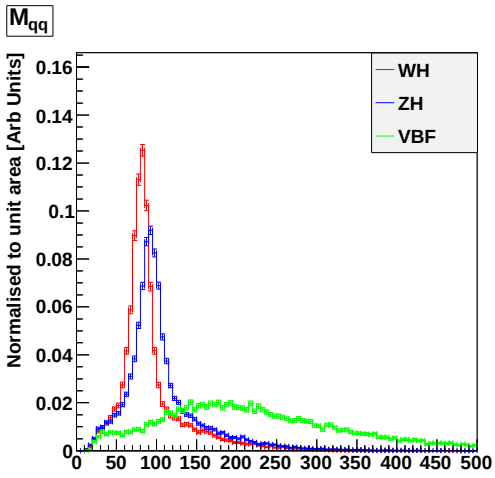

(b) m_{qq} distribution

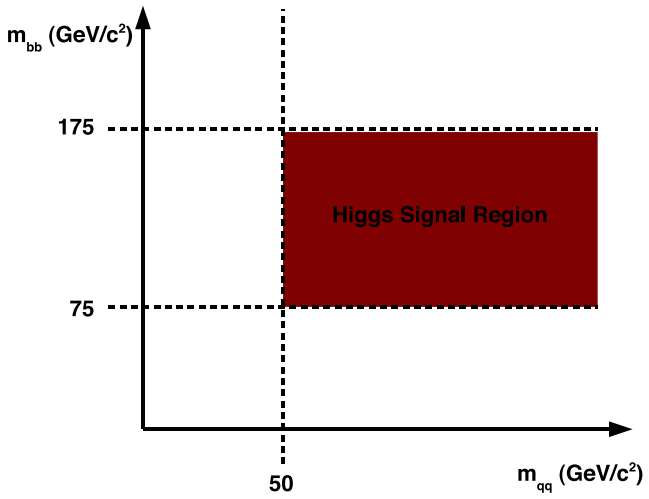

(c) Higgs Signal Region

Figure 2: m_{bb} and m_{qq} distributions for m_H=120 GeV/c^2. These distributions are used to define the Higgs signal region.

2.1.3 Signal Regions for the Analysis

The signal region is defined by the mass of the two b-tagged jet (m_{bb}) and the two untagged jets (m_{qq}). The VH channel has two mass resonances from the $H \rightarrow b\bar{b}$ decay and $V \rightarrow qq'$. The VBF channel only shares the m_{bb} resonance. But VBF has a distinct topology as the two untagged jets are far apart in η which gives a broad m_{qq} spectrum. So we define the Higgs signal region as

$75.0 < m_{bb} < 175.0\text{GeV}/c^2$ and $m_{qq} > 50.0\,\text{GeV}/c^2$ (Fig. 2).

2.1.4 Backgrounds

The backgrounds considered in this analysis are:

- QCD Multi-jets : this is the dominant background as it consists of about 98% of the total background
- Top quark pair production
- Single Top quark production
- W and heavy-flavor jets production (W+HF)
- Z plus jets production, where Z decays into $b\bar{b}$ and $c\bar{c}$ (Z+JET).
- Diboson production : WW, WZ, ZZ

The QCD multi-jet will be estimated from a data driven based technique. The non-QCD backgrounds will be estimated from simulation.

2.2 Signal and background Monte-Carlo samples

The signal and background Monte-Carlo (MC) samples were generated using a combination of Pythia[5] and Alpgen [6] (See table 3). The generated events were then passed through the CDF detector simulation and then scale factors for the trigger and b-tagging are applied to correct the MC.

- A scale factor is applied to account for the difference in b-tagging efficiency measured in data and MC. The scale factor for a single tight SecVtx tag is 0.950 ± 0.050, and the scale factor for a 1% JetProb tag is 0.690 ± 0.040 [7]. Therefore the effective scale factor for SS category is 0.902 ± 0.067, and the effective scale factor for SJ category is 0.655 ± 0.051.
- events which pass the trigger emulation are scaled by the trigger dependent scale factors given in table 2. The triggers used by the MC are in the same proportion as the luminosity recorded by each trigger. Thus the first 24.9% of each MC sample uses TOP_MULTI_JET_v-9, , the next 6.8% uses TOP_MULTI_JET_v-12 and the remainder of the sample uses VH_MULTIJET.

All the background events were generated as fully-inclusive except the signal and the Z+jets sample. The fully inclusive Z+jets cross-section is large and the majority of the events would not pass the trigger. A filter was used to select events which were likely to pass the trigger and event selection. The filter was devised at the generator level to select events with b/c partons, have 3 jets with $E_T >$ 5 Gev and a Sum-$E_T >$ 60 GeV. Further details on the filter can be found in section 13.1. The VH signal samples were generated with Pythia where the Higgs was forced to decay to $b\bar{b}$ and the W/Z was forced to decay to hadrons.

The Higgs signals (associated production and VBF) are all generated with Pythia and the goodrun listed used is up to period 17 (runlist_p0-p8_p10-p12_p15-p17_2008-12-17.txt) which consists of low, medium and high luminosity profiles. The $t\bar{t}$ MC samples used in this analysis (ttop75, otop49) also contain the low, medium and high luminosity profiles.

2.3 Expected Signal and Backgrounds

Tables 5 and 6 summarise the number of signal and background events expected in $9.45\,\text{fb}^{-1}$ and the final number of events used in the analysis. The non-QCD backgrounds are estimated from MC and assuming the cross-sections given in table 4. The difference of data and the sum of non-QCD backgrounds is assumed to QCD. The QCD multijet background makes up 98% of the total background and is modeled from data which is documented in section 4.

[3] MET significance = MET/$\sqrt{\text{Total Transverse Energy}}$

Table 3: Generators used for Non-QCD background samples

Channel	Generator
$t\bar{t}$	Pythia
Single Top - S channel	Pythia
Single Top - T channel	Pythia
WW	Alpgen+Pythia
WZ	Alpgen+Pythia
ZZ	Alpgen+Pythia
$W + b\bar{b}$	Alpgen+Pythia
$W + c\bar{c}$	Alpgen+Pythia
$Z \to b\bar{b}/c\bar{c} + jj$	Pythia

Table 4: The cross-sections for the non-QCD backgrounds and the sources used.

Process	Cross-section	Source
$t\bar{t}$	7.04 pb	CDF Note 10606 [8]
Single Top S channel	1.05 pb	CDF Note 10606 [8]
Single Top T channel	2.1 pb	CDF Note 10606 [8]
WW	11.34 pb	CDF Note 10606 [8, 9]
WZ	3.47 pb	CDF Note 10606 [8, 9]
ZZ	3.62 pb	CDF Note 10606 [8, 9]
$W + b\bar{b}$	24.7 pb	(Alpgen+Pyhtia LO x 1.4 K_NLO)
$W + c\bar{c}$	40.64 pb	(Alpgen+Pythia LO x 1.4 K_NLO)
$Z \to b\bar{b}/c\bar{c} + jj$	700.26 pb	(Pythia LO x 1.4 K_NLO)

Table 5: Table of WH, ZH and VBF Signal sources. The last two columns on the right are the total number of events which pass the trigger, event selection, have two b-tags and have been scaled by the MC corrections.

	σ /pb	$\sigma\times$ BR /pb for $q\bar{q}b\bar{b}$	Number of VH/VBF events in 9.45fb^{-1}	Used in analysis SS	SJ
WH 100	0.2811	0.1503	1419	17.8	6.4
WH 105	0.2387	0.1247	1178	16.7	6.1
WH 110	0.2037	0.1026	969	15.5	5.6
WH 115	0.1745	0.0832	786	14.3	5.2
WH 120	0.1501	0.0659	622	13.0	4.6
WH 125	0.1295	0.0506	478	10.9	3.8
WH 130	0.1120	0.0374	353	9.0	3.1
WH 135	0.0972	0.0266	251	7.0	2.5
WH 140	0.0846	0.0180	170	5.1	1.8
WH 145	0.0737	0.0115	109	3.5	1.2
WH 150	0.0644	0.0068	64	2.2	0.8
ZH 100	0.1627	0.0900	850	13.8	4.4
ZH 105	0.1395	0.0754	712	12.9	4.1
ZH 110	0.1202	0.0626	591	12.5	4.1
ZH 115	0.1039	0.0512	484	11.1	3.6
ZH 120	0.0902	0.0409	387	9.9	3.2
ZH 125	0.0785	0.0317	300	8.3	2.7
ZH 130	0.0685	0.0237	223	6.8	2.2
ZH 135	0.0600	0.0170	160	5.3	1.7
ZH 140	0.0527	0.0116	109	3.9	1.3
ZH 145	0.0463	0.0075	71	2.6	0.9
ZH 150	0.0408	0.0045	42	1.7	0.6
VBF 100	0.0973	0.0770	727	10.2	3.4
VBF 105	0.0898	0.0694	655	9.9	3.5
VBF 110	0.0828	0.0617	583	10.0	3.4
VBF 115	0.0765	0.0539	509	9.3	3.3
VBF 120	0.0707	0.0459	434	8.8	3.0
VBF 125	0.0653	0.0378	357	7.8	2.6
VBF 130	0.0605	0.0299	282	6.6	2.3
VBF 135	0.0560	0.0226	214	5.5	1.8
VBF 140	0.0519	0.0163	154	4.2	1.5
VBF 145	0.0480	0.0111	105	3.0	1.0
VBF 150	0.0445	0.0070	66	2.0	0.7

Table 6: Table of Backgrounds: The number of expected events for each background source after passing the trigger requirements and are accepted by the event selection cuts for the signal region. The estimations are calculated for integrated luminosity of 9.45 fb^{-1}. The difference between Data and non-QCD is assumed to be QCD.

	Higgs Signal region	
	SS	SJ
$t\bar{t}$	1032.2 ± 155.9	383.9 ± 56.8
Single Top S channel	110.5 ± 18.5	37.8 ± 6.2
Single Top T channel	44.0 ± 7.3	25.5 ± 4.2
$W + b\bar{b}$	77.0 ± 40.0	28.5 ± 14.8
$W + c\bar{c}$	8.3 ± 4.3	7.4 ± 3.6
$Z(\rightarrow b\bar{b}/c\bar{c})$ + Jets	872.6 ± 452.0	337.6 ± 174.5
ww	5.6 ± 0.8	5.6 ± 0.8
wz	19.7 ± 2.9	7.9 ± 1.1
zz	21.4 ± 3.1	7.9 ± 1.1
total non-QCD	2191.3 ± 480.3	842.1 ± 184.3
Data	87272	46818
QCD	85080.7	45975.9

3 bjet energy Neural Network correction

The di-jet invariant mass has a straight correlation to jet energy measurament and to optimize the di-jet mass we need to improve the resolution of jet energy measurament. These improvements will help to improve other parts of the analysis, such as the QCD modeling and jet shaping; both depend on the jet-E_T. A Neural Network (NN) is trained to correct the measured b-jet energy to the b-parton energy.

The tool used for the NN is the ROOT class TMultiLayerPerceptron. The choice of the variables to train the NN carry information of the jet energy. Two different NN were trained using SecVtxTag and JetProb events and two sets of variables was identified for them. We had 9 variables for SecVtxTag events:

- the Jet E_t after the Level 7 correction,
- the Jet P_t after Level 7 correction,
- the Jet Raw E_t,
- the transverse mass of Level 7 correction[4],
- the decay length of the jet in 2-dim and its uncertainty,
- the P_t of secondary vertex,
- the maximum P_t of the track inside the jet cone,
- the sum of all tracks inside the jet cone,

and 6 variables for JetProb events:

- the Jet E_t after the Level 7 correction,
- the Jet P_t after Level 7 correction,
- the Jet Raw E_t,
- the transverse mass of Level 7 correction,
- the decay length of the jet in 2-dim and its uncertainty.

The Jet-Tracks follows the criteria:

- Tracks inside the jet cone $\Delta R(track, jet) \leq 0.4$
- $\sharp COTHits > 5$
- $COT\chi^2/NDF < 2.0$
- $1GeV < TrackP_t < 100GeV$

The NN was trained with b tagged jets matched to b-partons. The match criteria is defined as ΔR between the b-jet and the b-parton is ≤ 0.4.

- Learning Method: Stochastic algorithm.
- Number of Training Cycles: 100.

[4]The jet transverse mass is define as $P_t/P * M$.

- Number of Hidden Layers: 18/12 for SecVtxTag/JetProb events.

The NN correction function is trained to estimate the ratio between the energy of b-parton and the b-jet.

We started to train, for each sample (VBF, WH and ZH), a dedicated NN. After the training we compared the resolution[5] for each mass at Level 7 and after the NN correction, the results are in figure 3.

To identify the best NN performance, we applied to each sample the others NN. We obtained the best performance with the VBF NN, so we decided to use that one for the analysis (fig. 4).

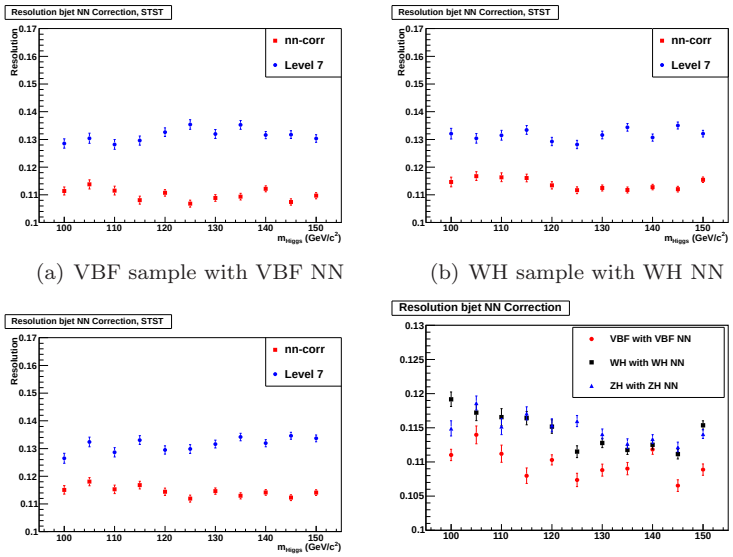

(a) VBF sample with VBF NN

(b) WH sample with WH NN

(c) ZH sample with ZH NN

(d) Overlap of NN resolution

Figure 3: The resolution for each mass point at Level 7 correction (blue) and NN correction (red) for a) VBF, b) WH and c) ZH samples with its own NN train. d) Overlap of resolution after the NN correction.

Figure 5 shows how the ratio between the energy of b-parton and the b-jet varies with the NN inputs before and after the jet energy correction.

Figure 6 is shows the comparision of mass distribution before and after NN correction; we have an improvmet of value of M_{bb}, the mean value shift to $\sim 124\,\mathrm{GeV}/c^2$, the RMS value reduces by $5-6\%$ and the resolution increase by $\sim 12-13\%$.

[5]The resolution is define as the ratio between RMS and mean value.

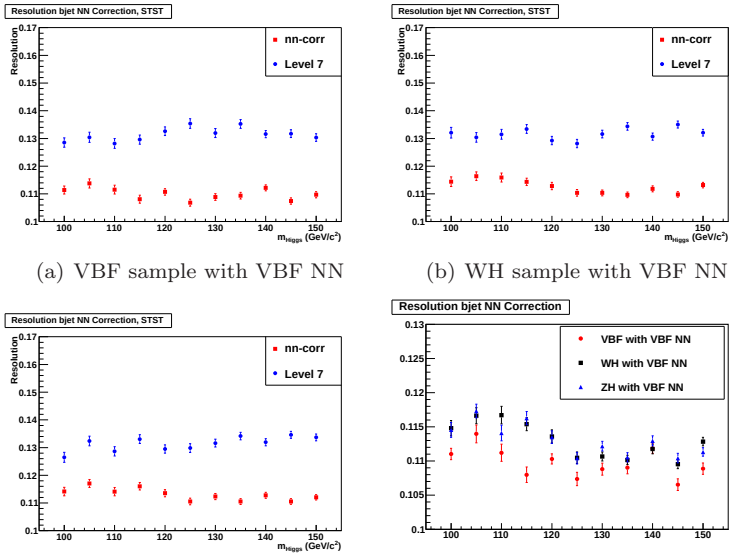

(a) VBF sample with VBF NN (b) WH sample with VBF NN

(c) ZH sample with VBF NN (d) Overlap of NN resolution

Figure 4: The resolution for each mass point at Level 7 correction (blue) and NN correction (red) for a) VBF, b) WH and c) ZH samples with VBF NN train. d) Overlap of resolution after the VBF NN correction.

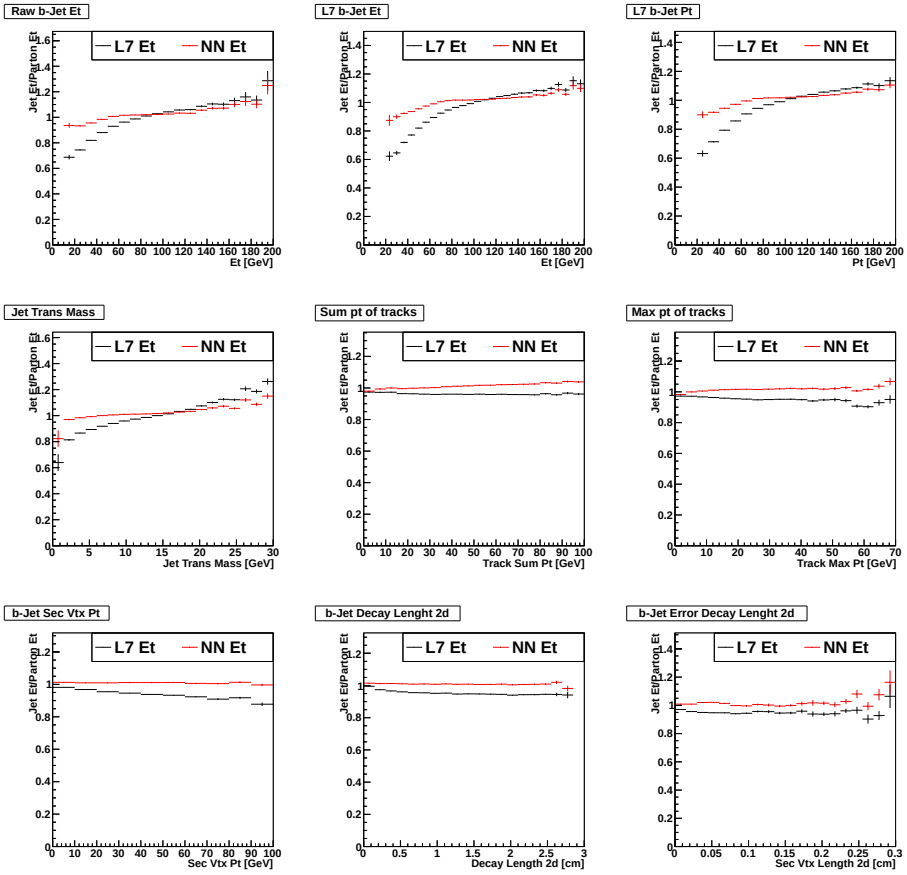

Figure 5: NN input variables.

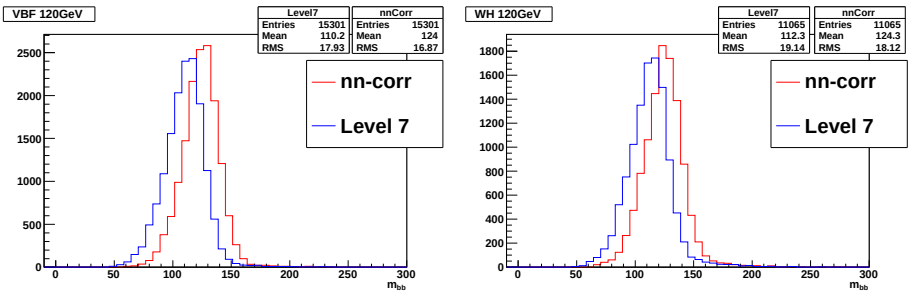

(a) VBF

(b) WH

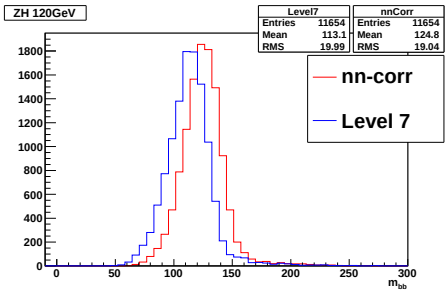

(c) ZH

Figure 6: Comparison of M_{bb} distribution at Level7 and NN Correction for a) VBF, b) WH and c) ZH sample with $M_H = 120GeV$.

4 Jet Width

The untagged q-jets from QCD are a mixture of quark and gluon jets whereas the q jets from the Higgs signal are quark jets. On average, gluon jets tend to be broader than quark jets. Thus the width of a jet can be used to discriminate quarks from gluons and so improve the separation of the QCD multijet background from the Higgs signal.

The 4fb^{-1} analysis used the precomputed values of $\langle\phi\rangle$ and $\langle\eta\rangle$ [2, 3] which is a measure of the jet-width along the ϕ and η axis. We have now combined these two measures into a single value and we now include the jet-width measured by the tracker The definitions of the jet width measured by the calorimeter ($\langle R\rangle_{CAL}$) and tracker ($\langle R\rangle_{TRK}$) are given in equation 1.

$$\langle R\rangle_{CAL} = \sqrt{\sum_{\text{towers}} \left[\frac{E_t^{\text{tower}}}{E_t^{\text{jet}}} \left(\Delta R(tower, jet)\right)^2 \right]} \tag{1a}$$

$$\langle R\rangle_{TRK} = \sqrt{\sum_{\text{tracks}} \left[\frac{P_t^{\text{track}}}{P_t^{\text{jet}}} \left(\Delta R(track, jet)\right)^2 \right]} \tag{1b}$$

where

$$\Delta R(tower, jet) \equiv \sqrt{(\text{tower } \eta - \text{jet } \eta)^2 + \Delta\phi(\text{tower } \phi, \text{jet } \phi)^2} \tag{2a}$$

$$\Delta R(track, jet) \equiv \sqrt{(\text{track } \eta - \text{jet } \eta)^2 + \Delta\phi(\text{track } \phi, \text{jet } \phi)^2} \tag{2b}$$

and $\Delta\phi$(tower/track ϕ,jet ϕ) is smallest angular difference between tower/tack ϕ and jet ϕ. All calorimeter towers inside the jet cone of ΔR < 0.4 are used in the $\langle R\rangle_{CAL}$ calculation. All tracks within the jet cone of ΔR < 0.4 are selected for $\langle R\rangle_{TRK}$ where a track is defined as:

- $1\,\text{GeV}/c <$ Track $P_T < 1\,\text{TeV}/c$
- Track $\chi^2/NDF < 5.0$
- Track $z_0 =$ track collection mean $z_0 \pm 1\,\text{cm}$

In this section E_T refers to L7 corrected E_T.

4.1 Comparison of jet-widths between data and MC simulation

We expect quark-jets and gluon-jets to have different widths. However the width of the jet is also affected by the jet-E_T jet-η and the number of vertices (NVtx). We also expect the MC jet-width will need to be calibrated to match the jet-width measured in data. As we only measure the jet-width of untagged, light-flavored jets, we require a high purity sample of light flavored jets. In the 4fb^{-1} analysis [2, 3], we used the jets from a hadronic W decay from a sample of $t\bar{t}$ in the leptons+jets decay channel. The data sample to select the $t\bar{t}$ events are from the high-Pt electron and muon datasets (from p0 to p28), and the MC samples are generated with Pythia (tt0p75+ot0p49). The $t\bar{t}$ candidates are selected with these cuts :

- At least one class 12 (or better) vertex
- $|z - \text{vertex}| < 60\,\text{cm}$
- 1 CEM electron ($Et > 20$ GeV), or 1 CMUP/CMX muon ($Pt > 20$ GeV)
- ≥ 4 jets ($Et(L7) > 20$ GeV, $|\,\eta\,| < 2.0$
- $MET > 25$ GeV, $Ht > 250$ GeV

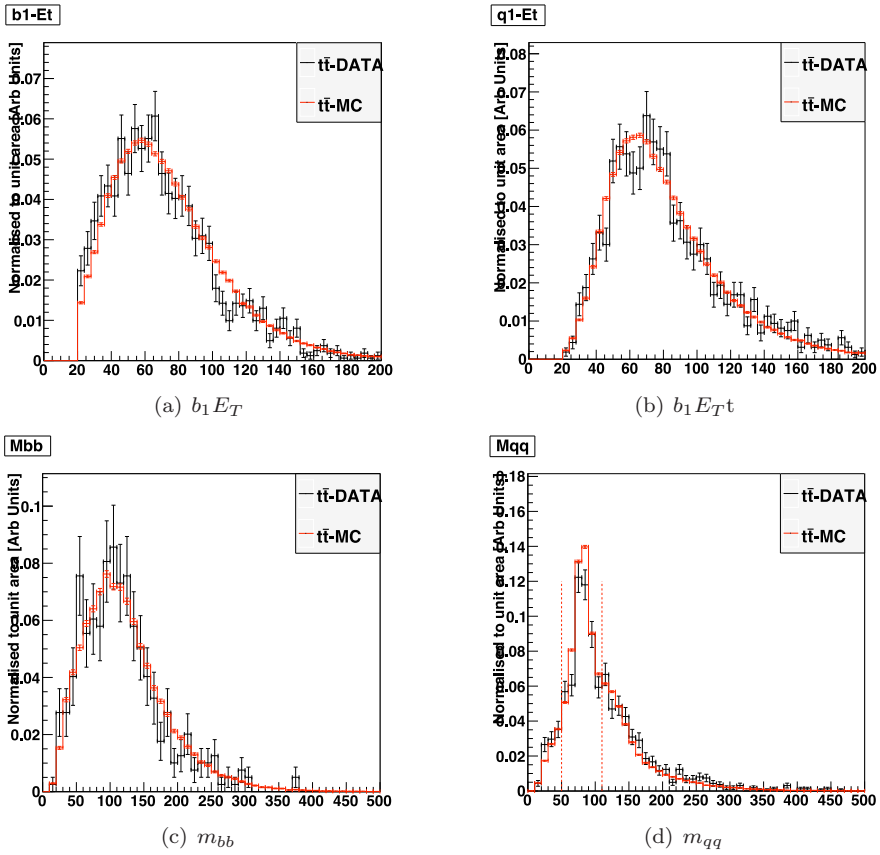

(a) $b_1 E_T$ (b) $b_1 E_T$t

(c) m_{bb} (d) m_{qq}

Figure 7: Comparison of the kinematic distributions of the selected $t\bar{t}$ candidates in the data to the $t\bar{t}$ events from simulation. The red dashed line for m_{qq} indicate the region used to select W candidates.

- ≥ 1 tight SecVtx tagged b-jet

Similar cuts are used in CDF 9462 [10] which measured the fraction of $t\bar{t}$ events with Njet=4,5 as $\sim 86\%$.

The plots in figure 7 shows the comparison of the kinematic distributions of the selected $t\bar{t}$ candidates in the data to the $t\bar{t}$ events from simulation. One sees good agreement between the data and MC which indicates that the fraction of real $t\bar{t}$ events in the data is large. For the jet shape studies, we select untagged jets which are in the W boson mass window defined as $50 < m_{qq} < 110\,\mathrm{GeV}/c^2$.

The plots comparing $\langle R \rangle_{CAL}$ and $\langle R \rangle_{TRK}$ distributions between data and MC for the $t\bar{t}$ events are shown in figure 8. Although the shapes between data and simulation are quite similar there is a small difference. The data is 86% $t\bar{t}$ and the remaining 14% is $W{+}b\bar{b}(\sim 4.2\%)$, $W{+}c\bar{c}(\sim 2.3\%)$, Wc, mistag, non-W, Z+jets, di-boson and single-top [10]. The inclusion of these additional backgrounds could account for the observed difference in the jet-widths. In the $4\,\mathrm{fb}^{-1}$analysis [2], this test was carried out and could not account for the observed difference between the data and simulation jet-widths.

As mentioned previously, the jet-width is also affected by the jet-E_T, jet-η and NVtx. The variation of the jet width is illustrated in figure 9. The calorimeter measured jet-width varies strongly with jet-E_T, jet-η and NVtx. The tracker measured jet-width shares a similar dependency on jet-E_T but has a weaker dependence on jet-η and NVtx.

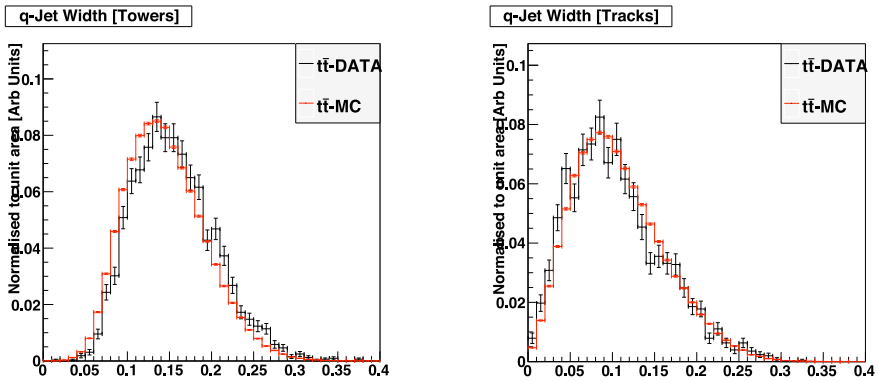

(a) $\langle R \rangle_{CAL}$ (b) $\langle R \rangle_{TRK}$

Figure 8: Comparing the $\langle R \rangle_{CAL}$ and $\langle R \rangle_{TRK}$ distributions between data and simulation for selected $t\bar{t}$ events.

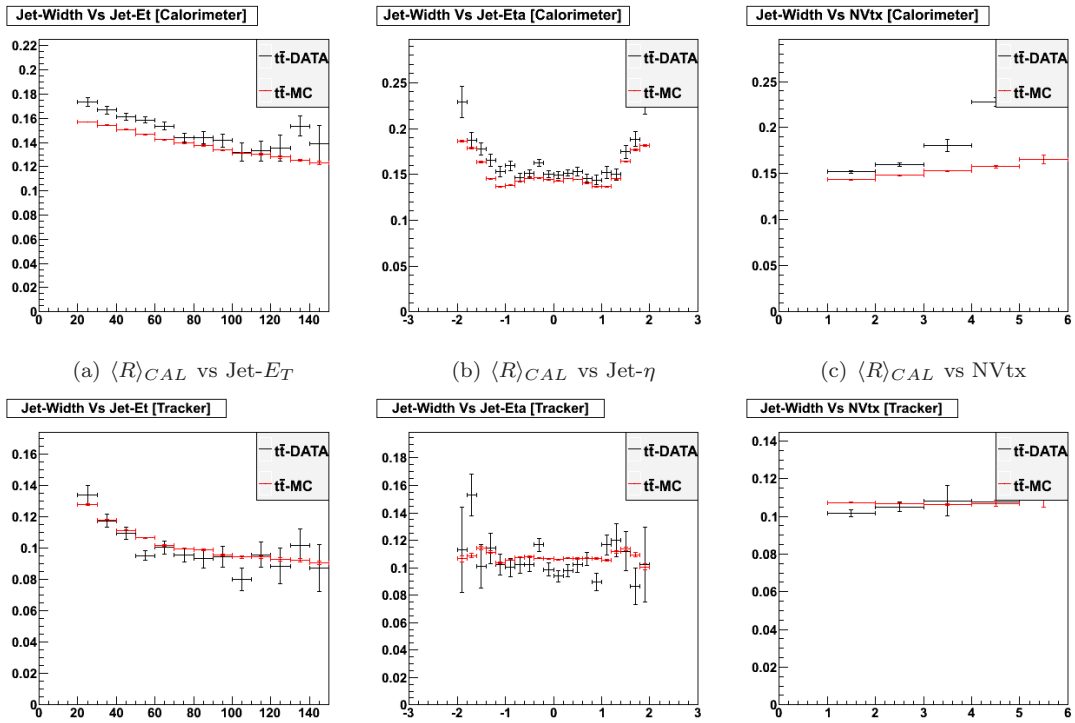

(a) $\langle R \rangle_{CAL}$ vs Jet-E_T (b) $\langle R \rangle_{CAL}$ vs Jet-η (c) $\langle R \rangle_{CAL}$ vs NVtx

(d) $\langle R \rangle_{TRK}$ vs Jet-E_T (e) $\langle R \rangle_{TRK}$ vs Jet-η (f) $\langle R \rangle_{TRK}$ vs NVtx

Figure 9: Profile histograms showing the variation of the $\langle R \rangle_{CAL}$ and $\langle R \rangle_{TRK}$ with jet-E_T, jet-η and NVtx

4.2 Parameterizing the jet-width dependence: removal of kinematic and detector biases

The jet-width depends on jet-E_T, jet-η and NVtx. In the $4\,\text{fb}^{-1}$analysis, the dependence was found by manually fitting functions of the jet-wdith against each dependence. We now train a neural network (NN) to extract a function which describes the jet width dependence as a function of jet-E_T, jet-η

and NVtx. We train a separate NN for data, MC, $\langle R\rangle_{CAL}$, $\langle R\rangle_{TRF}$. Using the NN fit functions, we can rescale the measured jet-width to a common reference point to remove the kinematic and detector biases. The common reference point is the jet-width from data for jet-E_T=50 GeV/c^2, jet-η=0 and NVtx=1.

- $\langle R\rangle_{CAL}$ reference point ($\langle R\rangle_{CAL}^{Ref}$) = 0.154
- $\langle R\rangle_{TRK}$ reference point ($\langle R\rangle_{TRK}^{Ref}$) = 0.108

We also use the same reference point for MC as this ensures the same width is measured for data and MC. The functions to rescale the measured jet-widths are shown in equation 3. $\langle R\rangle_{CAL}^{Data/MC}$($\langle R\rangle_{TRK}^{Data/MC}$) is the measured data/MC calorimeter(tracker) jet width and $\langle R\rangle_{CAL}^{Data/MC\prime}$($\langle R\rangle_{TRK}^{Data/MC\prime}$) is the data/MC calorimeter(tracker) jet width rescaled to the common reference point.

$$\langle R\rangle_{CAL}^{Data\prime} = \langle R\rangle_{CAL}^{Data} \times \frac{\langle R\rangle_{CAL}^{Ref}}{f_{CAL}^{Data}(\text{jet-}E_T, \text{jet-}\eta, \text{NVtx})} \tag{3a}$$

$$\langle R\rangle_{CAL}^{MC\prime} = \langle R\rangle_{CAL}^{MC} \times \frac{\langle R\rangle_{CAL}^{Ref}}{f_{CAL}^{MC}(\text{jet-}E_T, \text{jet-}\eta, \text{NVtx})} \tag{3b}$$

$$\langle R\rangle_{TRK}^{Data\prime} = \langle R\rangle_{TRK}^{Data} \times \frac{\langle R\rangle_{TRK}^{Ref}}{f_{TRK}^{Data}(\text{jet-}E_T)} \tag{3c}$$

$$\langle R\rangle_{TRK}^{MC\prime} = \langle R\rangle_{CAL}^{MC} \times \frac{\langle R\rangle_{TRK}^{Ref}}{f_{TRK}^{MC}(\text{jet-}E_T)} \tag{3d}$$

The function $f_{CAL}^{Data/MC}(\text{jet-}E_T, \text{jet-}\eta, \text{NVtx})$ is the NN data/MC jet width paramterization. The calorimeter jet-width dependence on jet-η changes rapidly at the transition from the central to the plug calorimeter ($|\eta| > 1.0$) (Fig. 9). It was found a single NN was not able to adquately fit for this transition. Instead two NN were required to paramterize the calorimeter jet-width: a parameterization for the central calorimeter $f_{CCAL}^{Data/MC}$ and the plug calorimeter $f_{PCAL}^{Data/MC}$.

$$f_{CAL}^{Data/MC}(\text{jet-}E_T, \text{jet-}\eta, \text{NVtx}) = \begin{cases} f_{CCAL}^{Data/MC}(\text{jet-}E_T, \text{jet-}\eta, \text{NVtx}) & |\text{Jet-}\eta| \leq 1.0 \\ f_{PCAL}^{Data/MC}(\text{jet-}E_T, \text{jet-}\eta, \text{NVtx}) & |\text{Jet-}\eta| > 1.0 \end{cases} \tag{4}$$

$f_{TRK}^{MC}(\text{jet-}E_T)$ is the NN data/MC jet width paramerization and is only a function of jet-E_T as the tracker jet width only had a weak dependence on jet-η and NVtx. The rescaled jet-wdiths are shown in Fig. 10 and shows all dependence on jet-E_T, jet-η and NVtx have been removed. Any difference in the jet-width can now be assumed to be due to the type of parton initiating the jet.

After applying the corrections, the $t\bar{t}$ MC jet-width distribution agrees better with the $t\bar{t}$ data. This is quantified by the change in the χ^2/NDF of the the MC and data jet-width distributions which reduces from 10.16(2.23) to 1.96(1.29) for the calorimeter(tracker) jet width (Fig. 4.2).

4.3 Systematic uncertainty of jet width for MC

The systematic uncertainty is estimated by adding an offset to the corrected MC jet-width and re-computing the χ^2/NDF of the data and adjusted MC jet width distribution. A range of offsets are examined and the χ^2/NDF($t\bar{t}$-MC,$t\bar{t}$-Data) curve is plotted in Fig. 4.3. The systematic uncertainty is defined as the offset required to change the χ^2/NDF by ± 1.

- Calorimeter jet width uncertainty: $\pm$0.004 ($\pm$2.6%)
- Tracker jet width uncertainty: $\pm$0.006 ($\pm$5.5%)

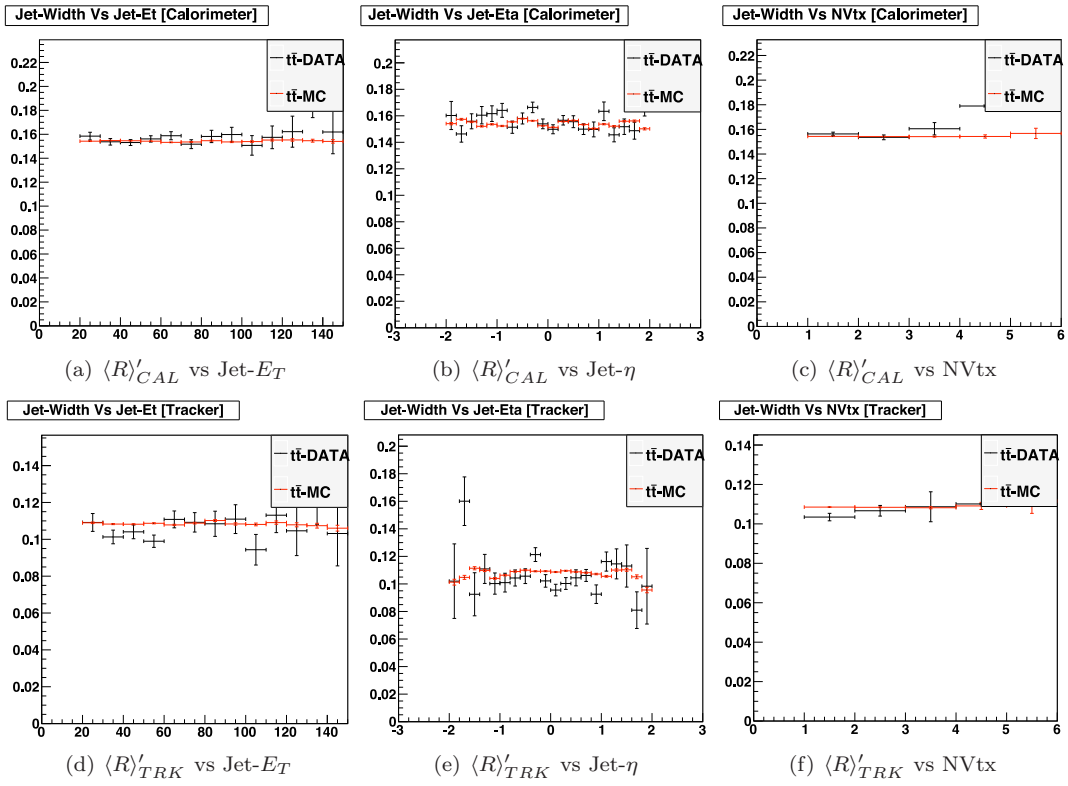

(a) $\langle R\rangle'_{CAL}$ vs Jet-E_T (b) $\langle R\rangle'_{CAL}$ vs Jet-η (c) $\langle R\rangle'_{CAL}$ vs NVtx

(d) $\langle R\rangle'_{TRK}$ vs Jet-E_T (e) $\langle R\rangle'_{TRK}$ vs Jet-η (f) $\langle R\rangle'_{TRK}$ vs NVtx

Figure 10: Profile histograms showing the variation of the $\langle R\rangle_{CAL}/\langle R\rangle'_{TRK}$ with jet-E_T, jet-η and NVtx. After applying the corrections, the jet-width is no longer dependent on jet-E_T, jet-η and NVtx.

The studies performed on the jet widths have only examined $t\bar{t}$ samples. The Higgs signal MC jet-width are compared with the $t\bar{t}$-MC to check both sample give the same jet width. Figure 4.3 show profile histograms of the corrected jet width of untagged jets against jet-E_T, jet-η and NVtx. We see no difference between the $t\bar{t}$ MC and the Higgs MC and thus no sample dependence on the jet-width parameterization.

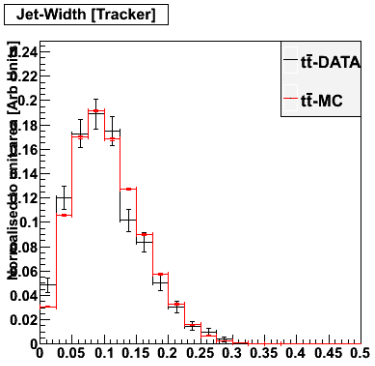

(a) $\langle R \rangle_{CAL}$: no corrections

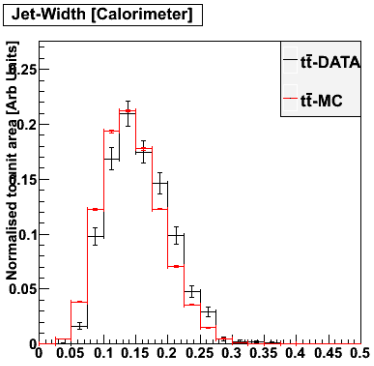

(b) $\langle R \rangle_{TRK}$: no corrections

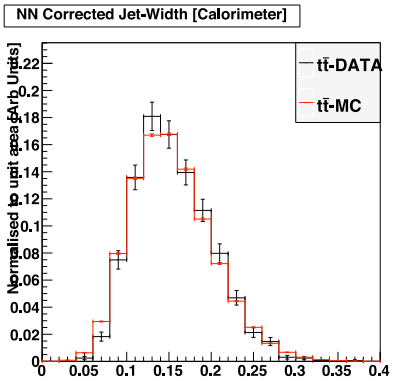

(c) $\langle R \rangle'_{CAL}$: after corrections

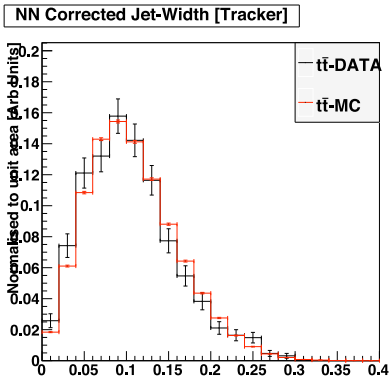

(d) $\langle R \rangle'_{TRK}$: $aftercorrections$

Figure 11: Jet width distributions before/after corrections are applied. Before any corrections, the $\chi^2/NDF = 10.16(2.23)$ for the calorimeter(tracker) jet width. After the corrections are applied, the χ^2/NDF reduces to 1.96(1.29) for the calorimeter(tracker) jet width.

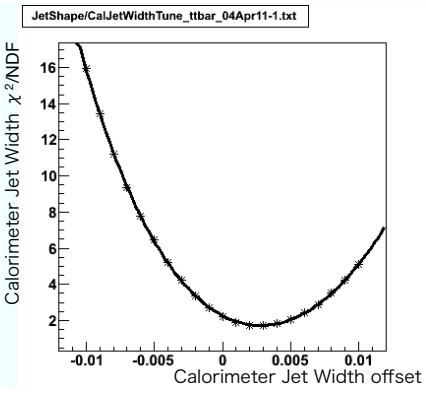

(a) χ^2/NDF vs calorimeter jet width offset

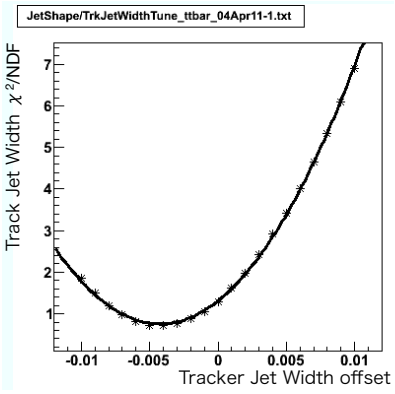

(b) χ^2/NDF vs tracker jet width offset

Figure 12: A range of offsets are added to the corrected MC jet-width and the variation of χ^2/NDF is plotted. The offset required to change the χ^2/NDF by ± 1 is used to define the uncertainty. The uncertainty is $\pm 0.004(0.006)$ for the corrected calorimeter(tracker) jet-width.

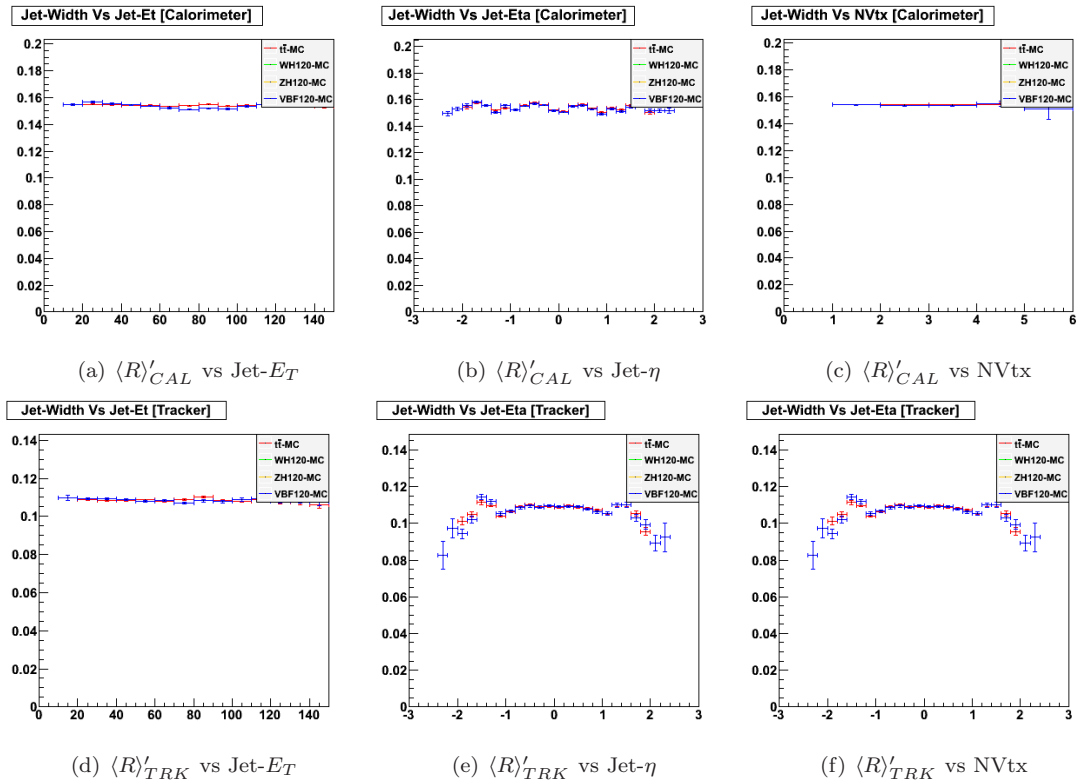

(a) $\langle R \rangle'_{CAL}$ vs Jet-E_T (b) $\langle R \rangle'_{CAL}$ vs Jet-η (c) $\langle R \rangle'_{CAL}$ vs NVtx

(d) $\langle R \rangle'_{TRK}$ vs Jet-E_T (e) $\langle R \rangle'_{TRK}$ vs Jet-η (f) $\langle R \rangle'_{TRK}$ vs NVtx

Figure 13: Comparison of $t\bar{t}$ and Higgs signal jet-widths. There is no variation between the samples.

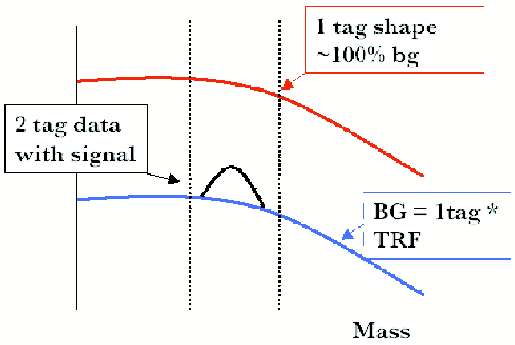

(a) TRF Principal: The red-line corresponds to the 1-tag distribution which is ≈100% background. The 2-tag background is assumed to be a scaled version of the 1-tag (background) distribution (blue line). The TRF is derived from the regions outside the signal peak.

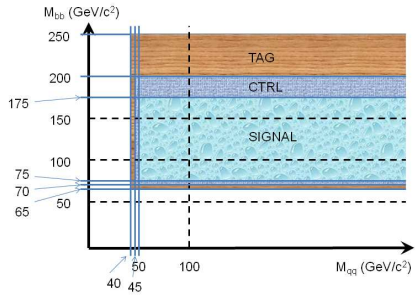

(b) Mbb-Mqq plane to define the TAG (brown) and CTRL (blue) regions.

Figure 14: The Tag-Rate function and the m_{bb}-m_{qq} plane

5 QCD Background Prediction: Tag-Rate-Function (TRF)

The critical component to this analysis is an accurate prediction of the QCD background as it is the dominant background. In this analysis a data driven model was devised to predict the two-tagged background from the background-rich one-tagged data. The assumption is the two-tagged background distribution is a scaled replica of the one-tagged distribution (figure 14). The scale factor which deduced from the one-tag data is a multi-dimentional function, called the Tag Rate Function (TRF). The TRF is the probability of a jet being b-tagged in the event that already has one other jet tagged as a b-jet. The probability is measured in a kinematic region that has very little contribution from the Higgs signal, the TAG region. This is applied to the one tagged events in the signal region to predict the double b-tagged QCD background. As a systematic, another TRF is derived from the control (CTRL) region. This is also applied to the 1-Tag data in the signal region to give an alternative background predicition. The difference of these two background predictions is applied as a systemtic error.

The key issue of this method is to make sure that the technique can correctly predict the shapes of the kinematic distributions of the double b-tagged QCD multi-jet events which will be used later in the NN training to separate the Higgs signal from the QCD background. This TRF method does not necessary predict the right normalization of the double b-tagged QCD background.

To measure the TRF, events having one or two tagged jets are considered. The events having three or more jets tagged are rejected. For each event one tagged jet is taken as Tag jet, then loop through the other three jets to probe for their tagging condition, they are taken as Probe jet in turn [6]. If a Probe jet is taggable this event is logged in the denominator. If the Probe jet is also tagged then the event is logged in the numerator. For the events having two tagged jets, each jet is taken as Tag jet in turn. The assumption here is that if a jet can be tagged it must be taggable. This is true for SecVtx b tagging. But it is not quite true for b tagging using jet probability. So we enforce this condition in the TRF measuring.

The TRF is parameterised as a function of three parameters which are:

- ΔR of Tag-Probe jet pair

[6] Jet-Et $> 15\,\text{GeV}$, $|\eta| < 2.4$, Number of good SecVtx (JetProb) tracks ≥ 2 when considering if the jet is SecVtx (JetProb) tagged

- E_T of the Probe jet
- pseudorapidity of the Probe jet ($|\eta|$)

$$TRF(\Delta\eta_{bb}, E_t, |\eta|) = \frac{\text{Number of } 2-\text{Tag events}(\Delta\eta_{bb}, E_t, |\eta|)}{\text{Number of events with } \geq \text{ 1 tight SecVtx tagged jet}(\Delta\eta_{bb}, E_t, |\eta|)} \quad (5)$$

The TRFs are measured separately for SS and SJ double b-tagged categories. For the SJ category, events with only one tight SecVtx tagged jets are considered in the measurement of the TRF(SJ).

The data used to derive the TRFs come from examining data outside the signal region (figure 14) in the M(bb)-M(qq) plane. The signal region is defined by $75 < M(bb) < 175$ GeV/c^2 and $M(qq) > 50$ GeV/c^2 mass window. Two regions outside the signal region are defined:

- CTRL region: an open-surrounding area around the signal region; $70 < M(bb) < 200$ GeV/c^2 and $M(qq) > 45$ GeV/c^2, except the signal region.
- TAG region: an open-surrounding area around the CTRL region; $65 < M(bb) < 250$ GeV/c^2 and $M(qq) > 40$ GeV/c^2, except the CTRL region and signal region.

The default TRF uses data from the TAG region. The CTRL region is used to derive systematic errors (figure 14). In the TRF deriving the contribution of $t\bar{t}$ and Z plus jets are subtracted.

The kinematic distributions of the predicted double b-tagged events in the signal region are compared to the observed double b-tagged events for the SS category. These comparison plots are shown in figure 15-20 from the SS events. The plots for SJ events are shown in 21-26.

Not all variable in the comparison shows consistency. One example is the $cos\theta$(helicity) of the higher energy b jet in the two b system. This variable shows some difference in between the Higgs and QCD events. However it can't be described by the TRF, see Figure 27, thus we can't use this variable in the analysis.

5.1 Tunning the Modeling of the Mass $M(qq)$

The TRF generated via this method does predict well the shapes of various kinematic variables except a few. Some of the well described variables, such as jet shape related variables, are shown in Fig. 15-27. A few variables are not well described but important to this analysis are $M(bb)$ and $M(qq)$. Possible reasons for the miss matching are the following. The ratio of 2 b tagged over 1 b tagged events is assumed to be flat. This assumption is true in large scale but not quite so in local area in the $M(bb)$, $M(qq)$ phase space. The other reason is that while developping the TRF both 1 b tagged and 2 b tagged events contribute to the denominator . While in predicting 2 b events in the signal region only 1 b tagged events are used. This creates slightly inconsistency in the composition of the denomenator. These are limitations of the method. We can only choose the variables that well described to proceed with the analysis so we need to correct for $M(qq)$ and hopefully the $M(bb)$ shape will follow.

To correct for $M(qq)$, we measure the correction function by applying the TRF to the one tagged events in the TAG region and measure the ratio of the predicted double b-tagged events to the observed b-tagged events as a function of the mass $M(qq)$. The correction function is then applied in the signal region when we are predicting the double b-tagged events in the signal region. As a systematic check, we also measured another correction function for $M(qq)$ in the CONTROL region and apply the correction function in predicting the 2 b-tagged events, in the signal region, while using the TRF from the CONTROL region. The difference in the predictions between using the TRF's (with their corresponding correction function) mesured from the TAG region and from the CONTROL region is part of the source of systematic uncertainty of the modeling.

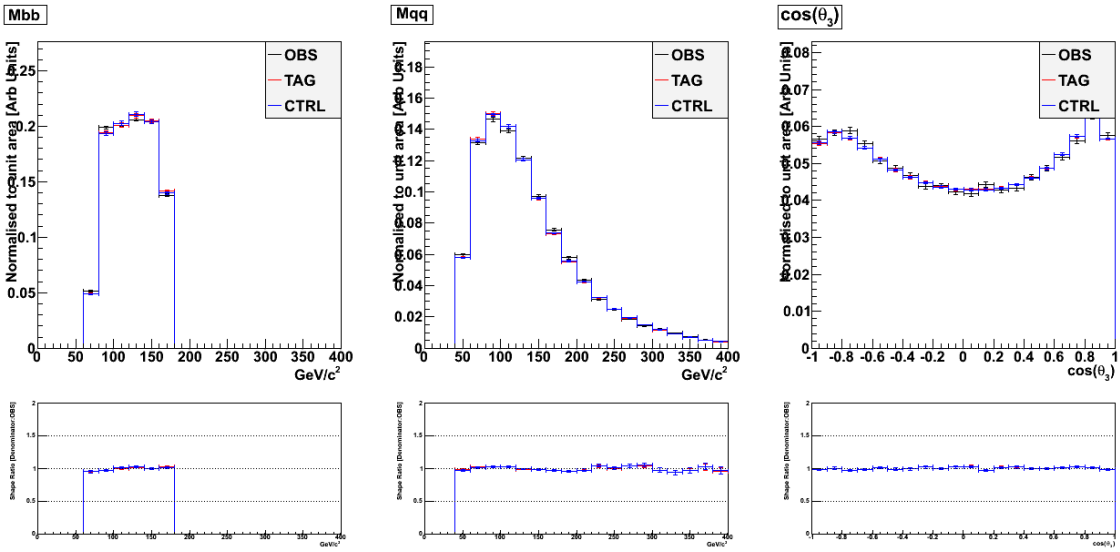

Figure 15: The kinematic distributions of the predicted double b-tagged events in the signal region are compared to the observed double b-tagged events for the SS category. The left side plot shows the invariant mass of the two b tagged jets system, $M(bb)$. The middle plot shows the invariant mass of the two not b tagged jets system, $M(qq)$. The right side plot shows the $cos\theta_3$ The red hashed histograms are the predicted double b-tagged events, and the black points are the observed double b-tagged events.

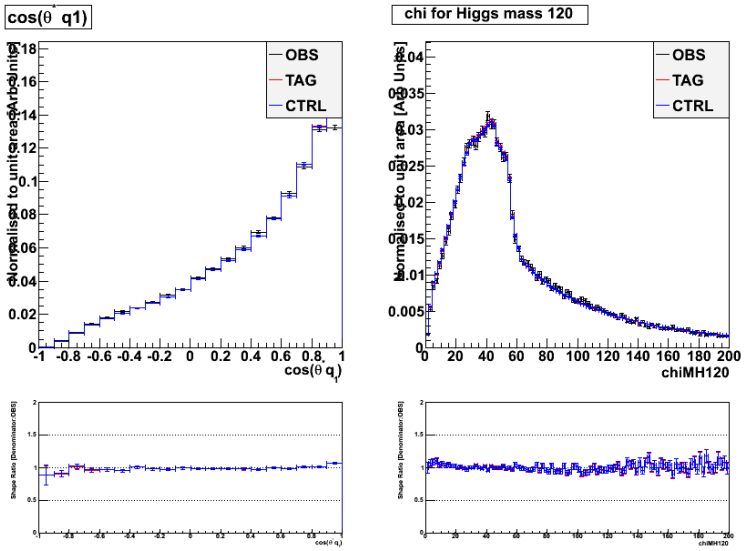

Figure 16: The kinematic distributions of the predicted double b-tagged events in the signal region are compared to the observed double b-tagged events for the SS category. Shown in left side is the *cosine* of the helicity angle of the most energetic not b tagged jet. Shown in the right side is the *chi* value comparing the $M(bb)$ to the assumed Higgs mass at 120 GeV/c^2 and the $M(qq)$ to the Z or W boson mass, depending on which difference is smaller. The red hashed histograms are the predicted double b-tagged events, and the black points are the observed double b-tagged events.

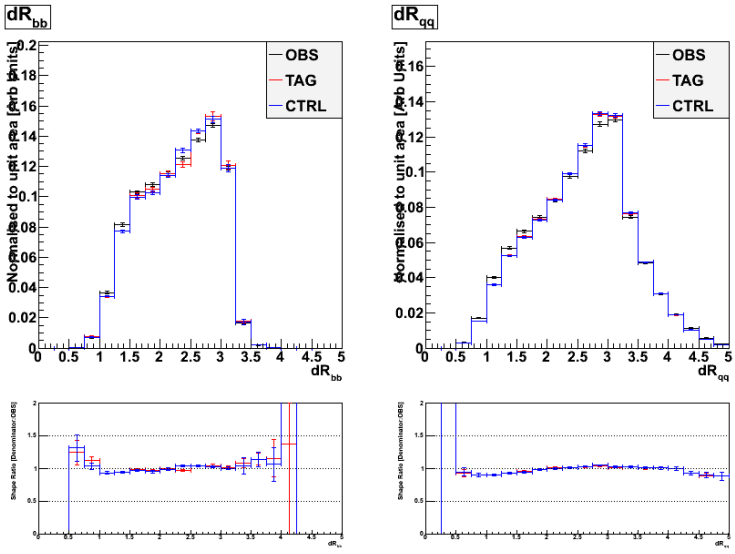

Figure 17: The kinematic distributions of the predicted double b-tagged events in the signal region are compared to the observed double b-tagged events for the SS category. Left side plot is dR_{bb}. Right side plot is dR_{qq}. The red hashed histograms are the predicted double b-tagged events, and the black points are the observed double b-tagged events.

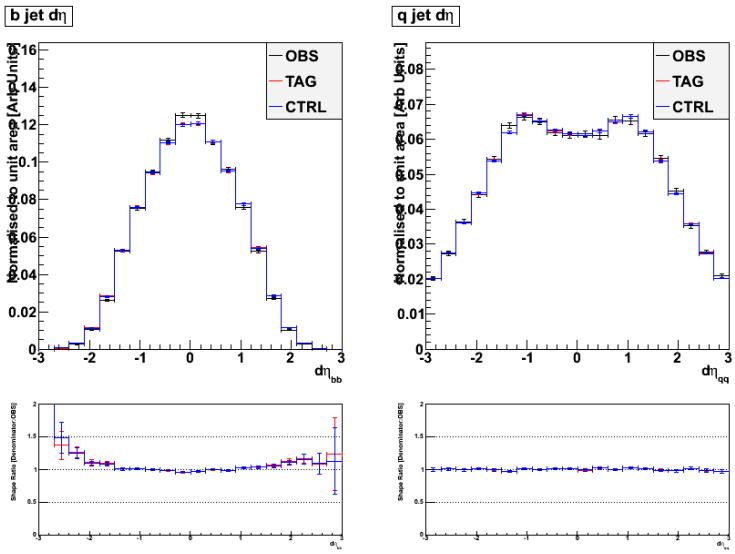

Figure 18: The kinematic distributions of the predicted double b-tagged events in the signal region are compared to the observed double b-tagged events for the SS category. Left side plot is $\mathrm{d}\eta_{bb}$. Right side plot is $\mathrm{d}\eta_{qq}$. The red hashed histograms are the predicted double b-tagged events, and the black points are the observed double b-tagged events.

5.2 Influence of the Higgs Signal to the TRF

If a Higgs signal exists, it would contribute to the TRF. Although at the predicted Higgs cross-section, the contribution of the Higgs signal to the TRF would be minimal.

To test the method, some Higgs events are injected into the regular data; from which we derive

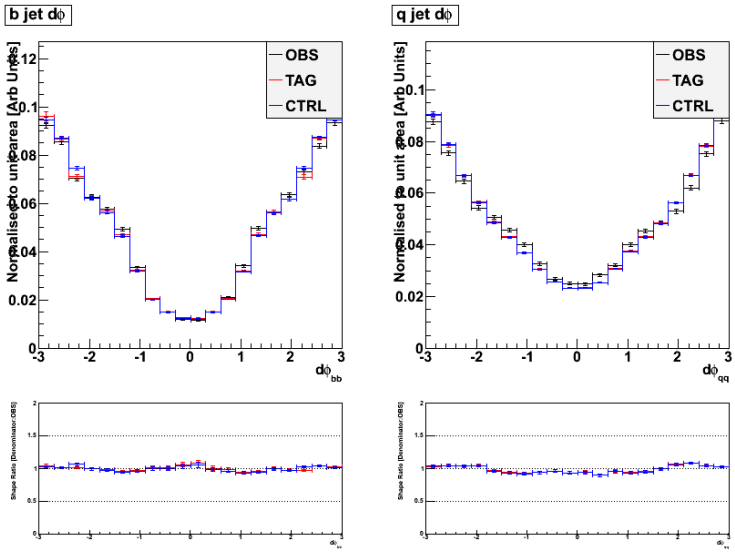

Figure 19: The kinematic distributions of the predicted double b-tagged events in the signal region are compared to the observed double b-tagged events for the SS category. Left side plot is dϕ_{bb}. Right side plot is dϕ_{qq}. The red hashed histograms are the predicted double b-tagged events, and the black points are the observed double b-tagged events.

another TRF and compare the new one with the nominal TRF. Two cases were tried; one has 14 times more of the Standard Model Higgs of mass 125 GeV/c^2, the T14 sample. Figure 28 shows the $M(bb)$ distribution of the nominal (upper left plot) samples and from the T14 samples (upper right plot). The ratio of the two is shown in the bottom, which has a small rise in the mass region around 125 GeV/c^2 as expected. The second samples has 100 times more of the Standard Model Higgs, the T100 samples. Figure 29 shows the $M(bb)$ from both nominal the T100 samples and the ratio of the two has larger rising in the mass range of 125 GeV/c^2 than the case of T14 as expected.

With added Higgs events new TRF's are derived and used to predict the background in the signal region. Comparing the prediction of the TRF from the T14 samples against the prediction using the nominal TRF, we see no significant difference. For the variables that are b quark pair related there are very tiny fluctuations. The most relavant example is $M(bb)$, see Figure 30. For the histograms of the variables that are light quark pair related no fluctuation is seen, one important example is $M(qq)$, see Figure 31. Similar situation is seen using the TRF from the T100 samples, see Figures 32, 33.

With added Higgs samples there is only tiny change in the TRF, which has no significant change in the prediction. This shows that the TRF is reliable and stable in predicting the background in reasonable range of Higgs cross section. Up to 100 times more the method is still sound.

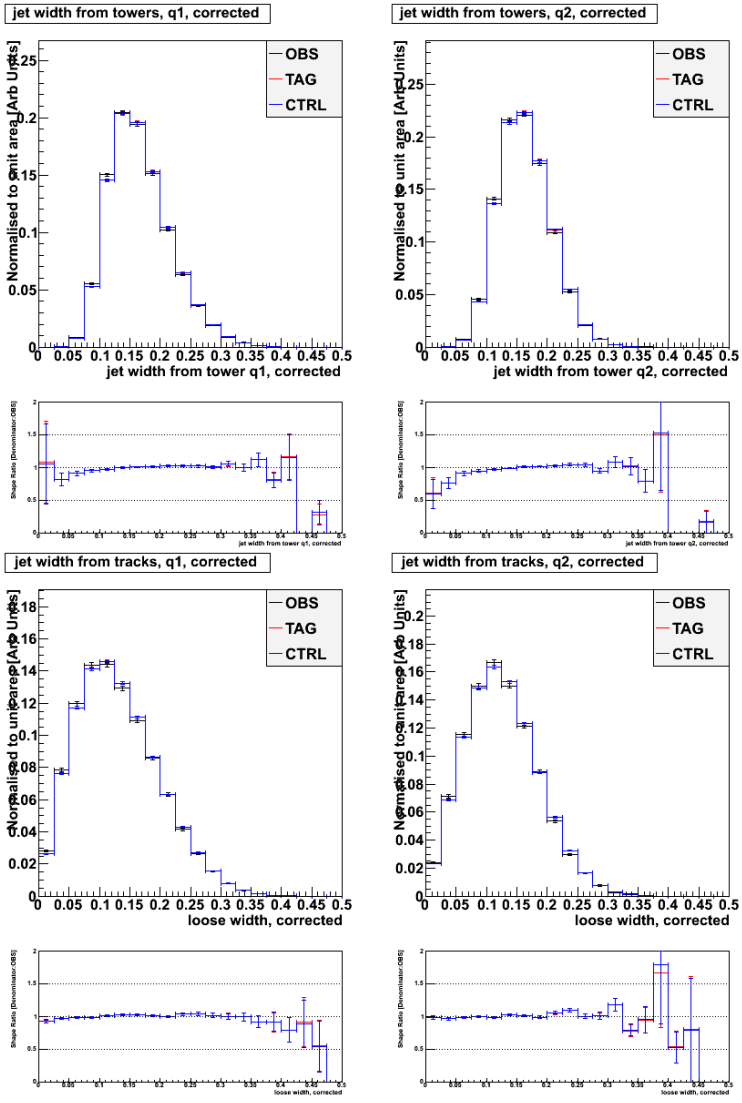

Figure 20: The distributions of jet width based on calorimeter tower and tracks for the predicted double b-tagged events in the signal region are compared to the observed double b-tagged events for the SS category. The red hashed histograms are the predicted double b-tagged events, and the black points are the observed double b-tagged events.

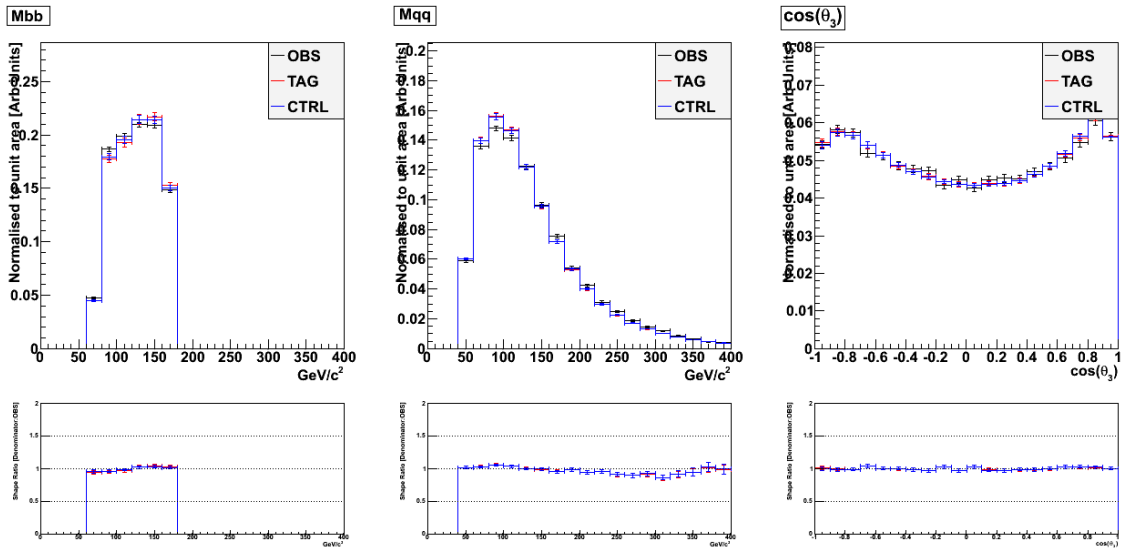

Figure 21: The kinematic distributions of the predicted double b-tagged events in the signal region are compared to the observed double b-tagged events for the SJ category. The left side plot shows the invariant mass of the two b tagged jets system, $M(bb)$. The middle plot shows the invariant mass of the two not b tagged jets system, $M(qq)$. The right side plot shows the $cos\theta_3$ The red hashed histograms are the predicted double b-tagged events, and the black points are the observed double b-tagged events.

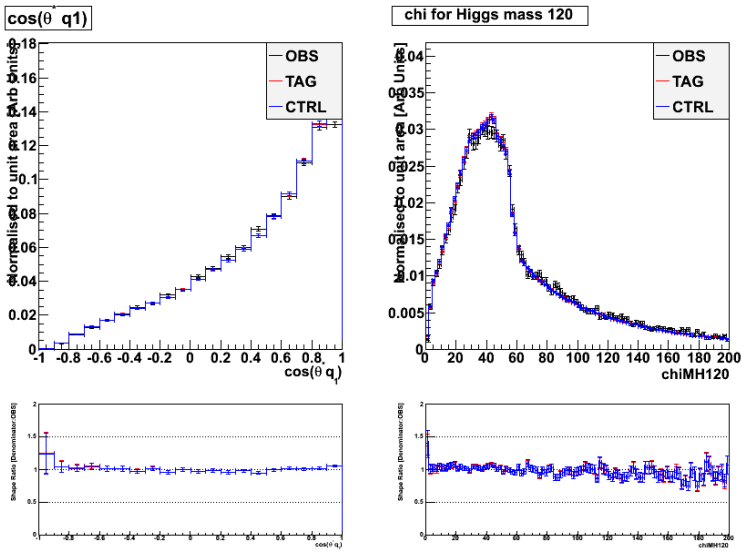

Figure 22: The kinematic distributions of the predicted double b-tagged events in the signal region are compared to the observed double b-tagged events for the SJ category. Shown in left side is the *cosine* of the helicity angle of the most energetic not b tagged jet. Shown in the right side is the *chi* value comparing the $M(bb)$ to the assumed Higgs mass at 120 GeV/c^2 and the $M(qq)$ to the Z or W boson mass, depending on which difference is smaller. The red hashed histograms are the predicted double b-tagged events, and the black points are the observed double b-tagged events.

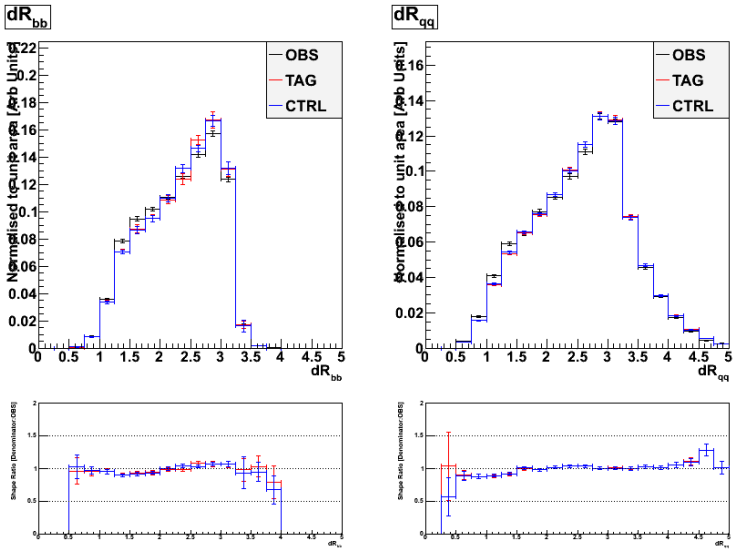

Figure 23: The kinematic distributions of the predicted double b-tagged events in the signal region are compared to the observed double b-tagged events for the SJ category. Left side plot is dR_{bb}. Right side plot is dR_{qq}. The red hashed histograms are the predicted double b-tagged events, and the black points are the observed double b-tagged events.

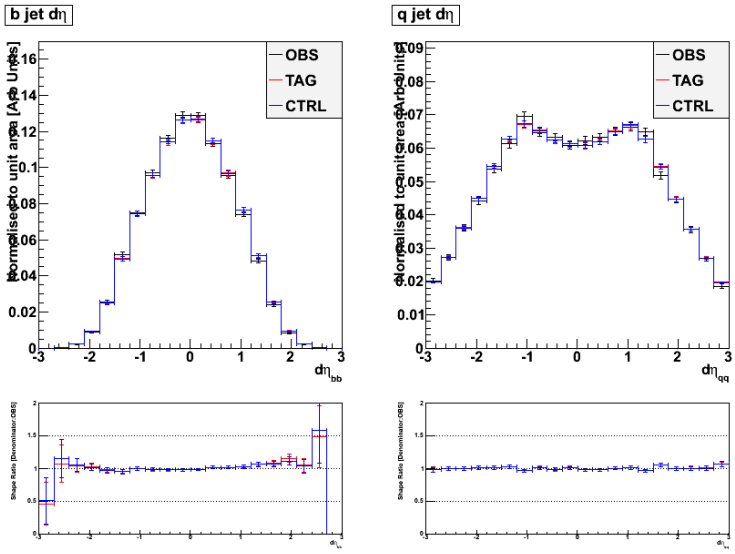

Figure 24: The kinematic distributions of the predicted double b-tagged events in the signal region are compared to the observed double b-tagged events for the SJ category. Left side plot is $\mathrm{d}\eta_{bb}$. Right side plot is $\mathrm{d}\eta_{qq}$. The red hashed histograms are the predicted double b-tagged events, and the black points are the observed double b-tagged events.

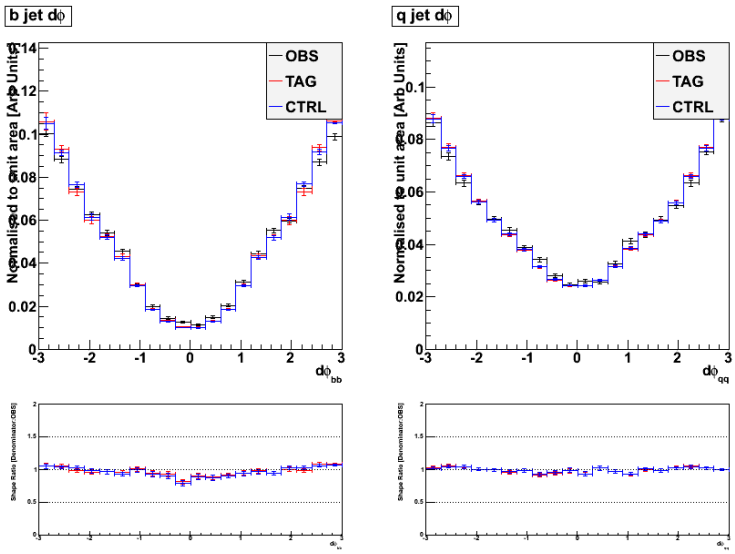

Figure 25: The kinematic distributions of the predicted double b-tagged events in the signal region are compared to the observed double b-tagged events for the SJ category. Left side plot is dϕ_{bb}. Right side plot is dϕ_{qq}. The red hashed histograms are the predicted double b-tagged events, and the black points are the observed double b-tagged events.

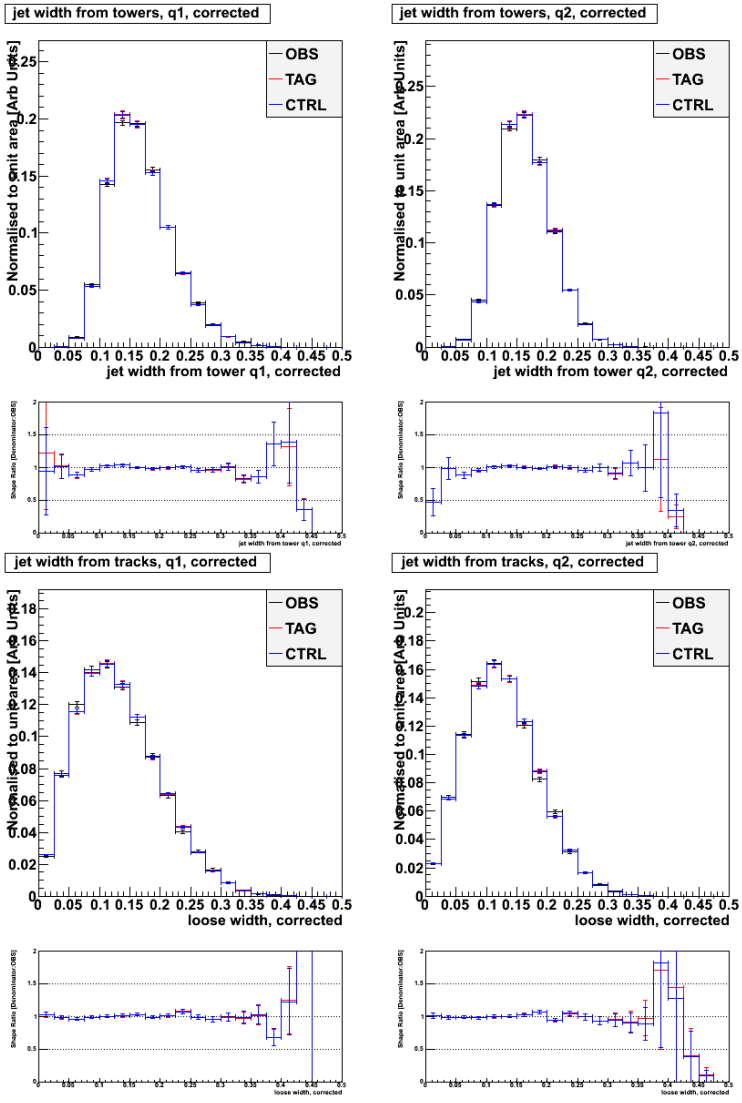

Figure 26: The distributions of jet width based on calorimeter tower and tracks for the predicted double b-tagged events in the signal region are compared to the observed double b-tagged events for the SJ category. The red hashed histograms are the predicted double b-tagged events, and the black points are the observed double b-tagged events.

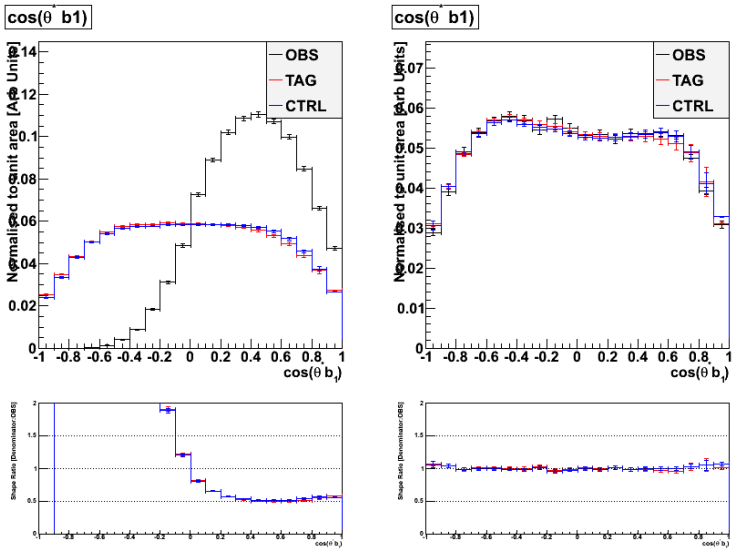

Figure 27: The distributions of $cos\theta$ (helicity) for the predicted double b-tagged events in the signal region are compared to the observed double b-tagged events. Shown in the left side is for the SS events; right side is for SJ events. The red hashed histograms are the predicted double b-tagged events, and the black points are the observed double b-tagged events.

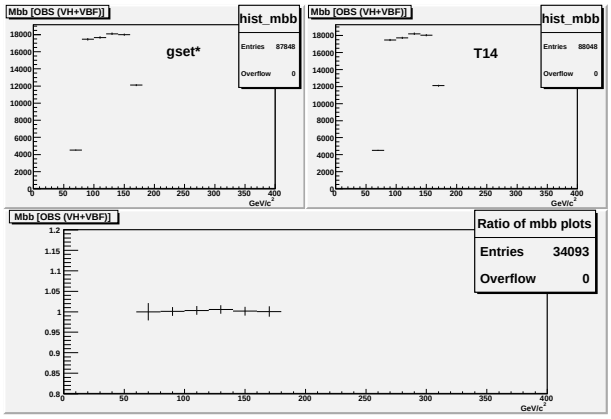

Figure 28: The plot in the upper left side shows the $M(bb)$ distribution from the regular samples. The plot in the upper right side shows the same distribution from the T14 samples. A small rise is seen in the region around $M(bb) = 125$ GeV/c^2.

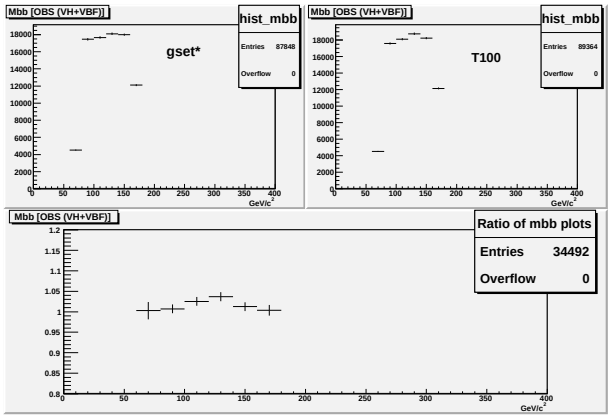

Figure 29: The plot in the upper left side shows the $M(bb)$ distribution from the regular samples. The plot in the upper right side shows the same distribution from the T100 samples. The rise in the region around $M(bb) = 125$ GeV/c^2 is seen more apparent than the T14.

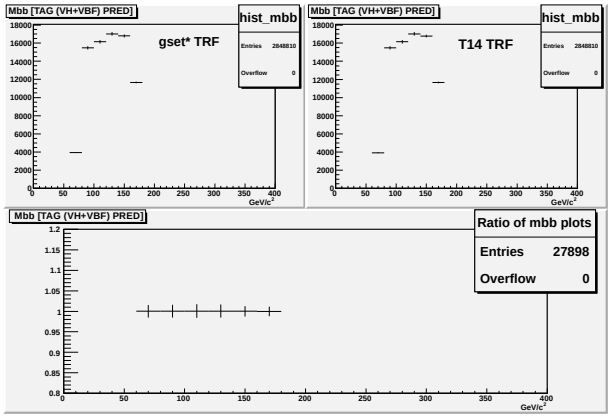

Figure 30: The plot in the upper left side shows the predicted $M(bb)$ distribution using the TRF from the regular samples. The plot in the upper right side shows the predicted $M(bb)$ distribution using the TRF derived from the T14 samples. No apparent rising is seen.

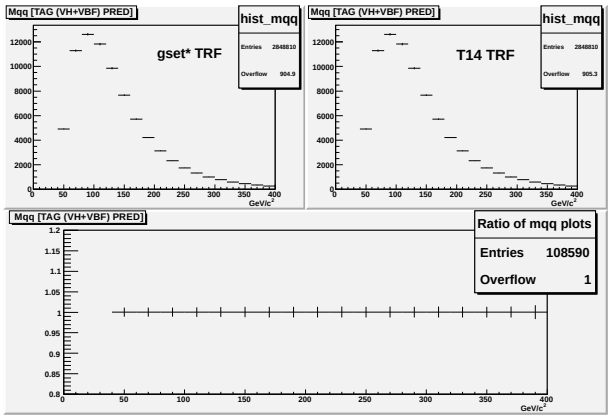

Figure 31: The plot in the upper left side shows the predicted $M(qq)$ distribution using the TRF from the regular samples. The plot in the upper right side shows the predicted $M(qq)$ distribution using the TRF derived from the T14 samples. No apparent rising is seen.

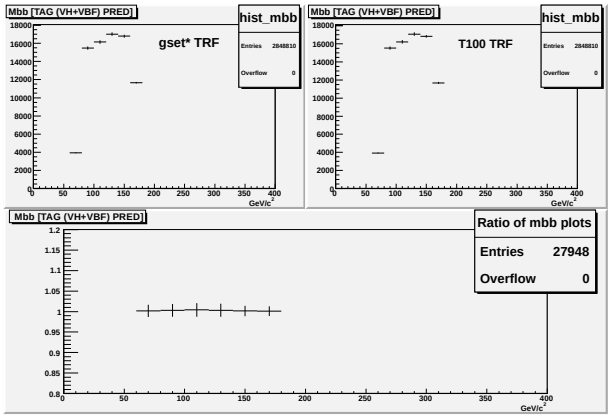

Figure 32: The plot in the upper left side shows the predicted $M(bb)$ distribution using the TRF from the regular samples. The plot in the upper right side shows the predicted $M(bb)$ distribution using the TRF derived from the T100 samples. No apparent rising is seen.

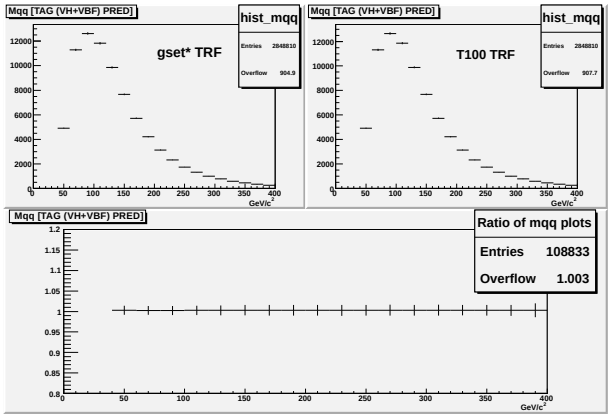

Figure 33: The plot in the upper left side shows the predicted $M(qq)$ distribution using the TRF from the regular samples. The plot in the upper right side shows the predicted $M(qq)$ distribution using the TRF derived from the T100 samples. No apparent rising is seen.

6 Untagged Jets Neural Networks

In the association production of Higgs particle there are light quark pairs from Z, W decay or through vector boson fusion, VBF. These light quark pairs have special features that can be used to help discrimnate the QCD background thus help the search of Higgs particle. So we train special Neural Networks to identify light quark pairs in the association production of Higgs particle event. Below we describe the features of the light quark pairs and how the Neural Networks are trained.

The main variable is $M(qq)$ which is the invariant mass of the two light quark jets, qq. Which is of course the main signature of Z and W bosons. In case of VBF, the same distribution is much wider and similar to qq from QCD.

The dR(qq) is defined as $\sqrt{d\phi + d\eta}$ of the qq which is strongly correlated to the opening angle of the two jets. For ZH and WH the qq jets are constraint to the mass of Z and W thus they don't go wide open as the qq from QCD where they could go back to back. For VBF the qq jets are very wide open in both ϕ and η phase space, especially in η, where the QCD light quark jets are not wide open but the ones from VBF are mostly back to back.

The other two main variables used are dϕ and dη, which are the differences of two ϕ angles and two η's of qq. For qq in the Z decay they form a cluster in the low dϕ and zero dη region. The empty hole is due to the two jets come too close to each other and are not reconstructed, this is shown in the plot (a) of Figure 34. For W it is quite similar as Z. For QCD the qq jets have large opening in the ϕ angle and close in η; this is shown in the plot (b) of Figure 34.

The qq in the case of VBF the qq are mostly back to back, having large opening in both ϕ and η; this is shown in the plot (a) of Figure 35. Shown in the plot (b) of Figure 35 is the dϕ vs. dη plot for the top pairs. This has a lot of overlap with ZH and WH thus to reject top requires other variable, such as Pt of the first four jets. However here we train NN's to reject QCD only.

Other variables such as Ptq, the transverse momentum of one q jet in the qq system, also shows difference for qq from ZH and WH. However the Ptq is highly correlated with the $M(qq)$ so when $M(qq)$ is used this variable provides little additional informaiton.

For the training purpose we specifically pick events that have exactly two b tagged jets and two untagged jets. The events of three or more b tagged jets are rejected purposely, which could happen especially in case of ZH when both Z and H decay into b quark pairs. In such case it is not clear which two jets are from Z and which two are from Higgs. This causes confusion in the Neural Network training.

The Neural Networks, YC_ZH and YC_WH, for the ZH and WH respectively, are trained based on $M(qq)$, dR(qq), dη(qq), dϕ(qq), ptq, pz(qq)/p(qq), pt(qq). While for VBF the Neural Network, YC_VBF, is trained based on $M(qq)$, dR(qq), dη(qq), abs(dη(qq))/dR(qq), abs(dϕ(qq))/dR(qq), ptq.

The performance of YC_ZH (plot (a)) and YC_WH (plot (b)) Neural Networks are shown in Figure 36. The performance of YC_VBF is shown in Figure 37. These are used in the final NN's for ZH, WH and VBF higgs search individually.

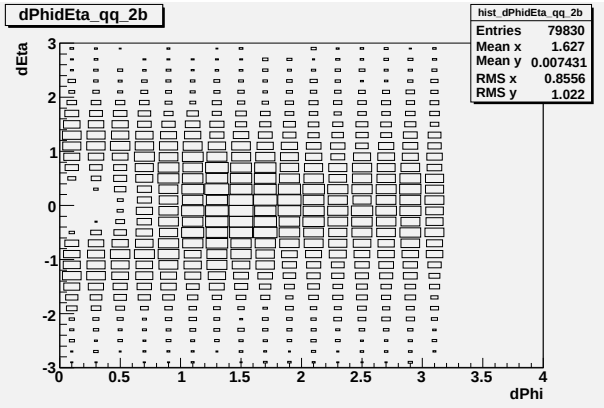

(a) ZH

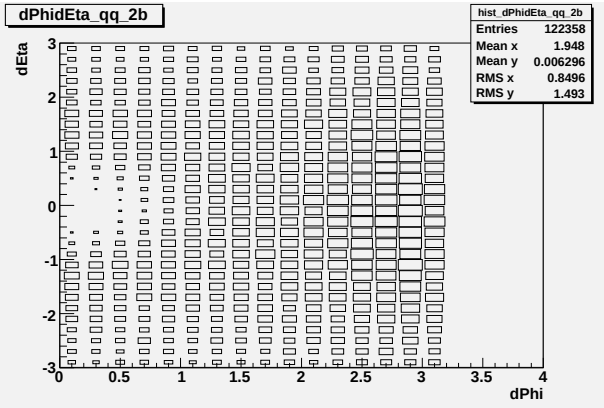

(b) QCD

Figure 34: dϕ vs. dη of the two light quark jets in the Higgs association production of ZH, which is shown in the plot (a). In the plot (b) it is dϕ vs. dη of the two light quark jets in the case of QCD.

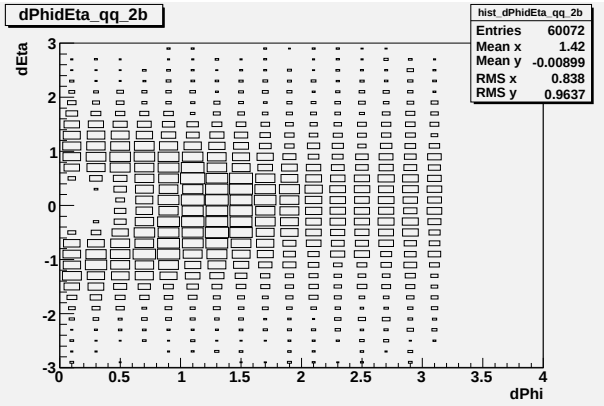

(a) VBF

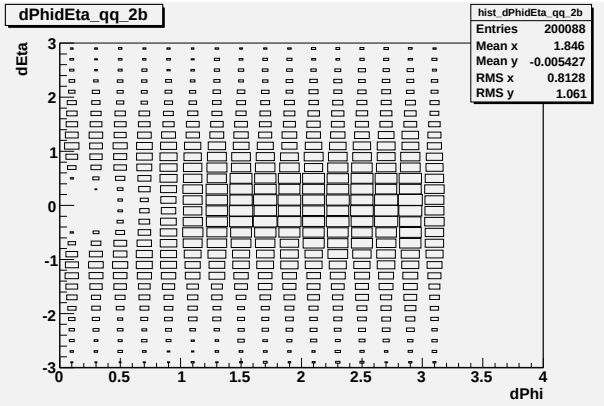

(b) TT

Figure 35: dϕ vs dη of the two light quark jets in the Higgs association production via VBF is shown in the plot (a). In the plot (b) it is the two light quark jets in the top pair events.

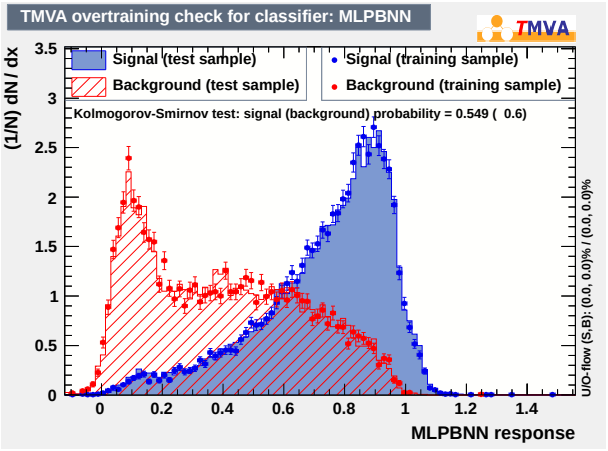

(a) ZHQCD

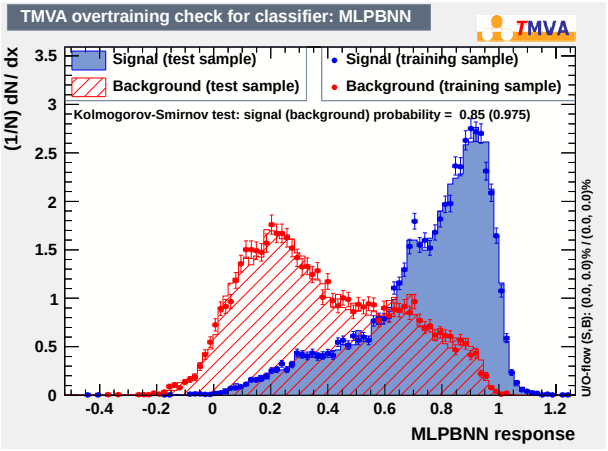

(b) WHQCD

Figure 36: The performance of YC_ZH (shown in the plot (a)) and YC_WH (shown in the plot (b).

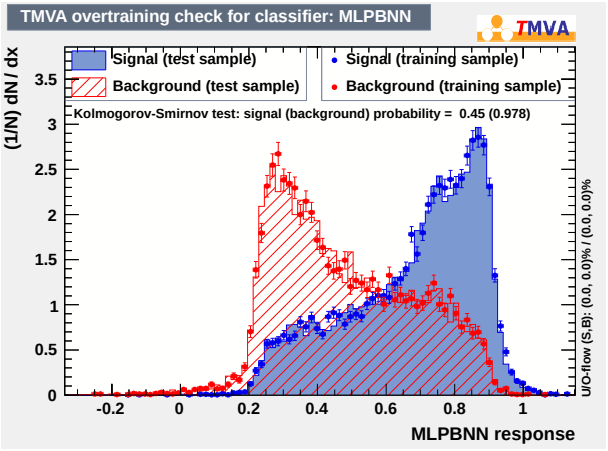

(a) ZHQCD

Figure 37: The performance of YC_VBF.

7 Neural Network Training

For the Higgs analysis, a multivariate discriminant has the ability to combine the information from several variables. This improves the ability to separate a Higgs signal from background events far greater than a standard cuts analysis. The TMVA package [11] allows one to evaluate several multivariate classifiers. For this analysis, we considered an Artificial Neural Network [7].

A dedicated Neural Net was trained for each process, WH, ZH and VBF. Because the proceses WH and ZH are similar we continue to identify them as VH, although the Neural Net was trained separately. The output of this first Neural Net was used as the input of a second one (SuperDiscriminant - SD). We used the output of the last Neural Net for the analysis.

After training with different variables and examining the signal efficiency/background rejection, expected limit & overtraining results, the Neural Net performed best was selected as the classifier for this analysis. The settings for the neural work were:

- Neuron Type : tanh
- Number of Training Cycles : 1000
- Number of Hidden Layers : 1 Hidden layer with N-inputs+1 nodes.
- 30,000/10,000 training & testing events are used for signal & background for MH100 (only VBF), MH120 and MH140.
- 17,000/1,700 training & testing events are used for signal & background for MH100 WH.
- 22,000/1,900 training & testing events are used for signal & background for MH100 ZH.
- 30,000/10,000 training & testing events are used for signal & background for MH100, MH120 and MH140 in SuperDiscriminant.

As the background is dominated by QCD, the 1-Tag background, weighted by the TRF, is used as the background sample for the NN. As we wish to keep the NN training, testing and final analysis events separate, the samples were divided as follows:

- 10% of the 1-Tag background sample from Signal region used only for training & testing Neural Net.
- The remaining 90% of the 1-Tag background sample from the Signal region was only used for the analysis.
- A dedicated Higgs signal sample for NN training & testing
- A dedicated Higgs signal sample for the analysis which is statistically independent to the NN training/testing samples.
- The two tagged events are only ever used in the analysis.

The Neural Net was trained at three target Higgs masses; 100 GeV, 120 Gev and 140 GeV. These three trained neural nets were used to search for a Higgs boson between 100 GeV to 150 GeV. For each mass point, the closest trained neural net was used as follows:

- 100 GeV Higgs used Neural Net trained on 100 GeV Higgs sample
- 105, 110, 115, 120, 125, 130 GeV Higgs used Neural Net trained on 120 GeV Higgs sample
- 135, 140, 145, 150 GeV Higgs used Neural Net trained on 140 GeV Higgs sample

[7] We followed TMVAs recommendation of the Multi-layer Perceptron algorithm for the artificial neural network

For all Neural Nets the same window cut was applied:

$$\begin{aligned} \text{Signal Window} \quad : \quad & 75 < M(b\bar{b}) < 175\text{GeV} \\ & M(q\bar{q}) > 50\text{GeV} \end{aligned} \tag{6}$$

The selection of variables for the first neural net training must fulfil two criteria:

- the variable must give good background-signal separation.
- The variable must be well modelled by the Tag-Rate-Function (TRF).

A initial list of 68 variables was drawn and were judged by the two criteria. After this first pass, the number of suitable variables reduced to 29. The next step was to examine which variables help the Neural Net to separate the signal from background. An initial neural net trained with just M_{bb}, M_{jj} (the Higgs & W/Z mass resonance), $\cos(\theta_3)$ and Chi (both defined later). Then an additional variable was added from the reduced list until all 29 variables were added. At each stage, the signal efficiency for different background rejection rates and the expected (statistics-only) limit was recorded.

7.1 VH Neural Net Training

For the VH neural net training, the samples used were:

- Signal : dedicated WH and ZH training samples
- Background: the 10% 1-Tag background

The list of training variables for the VH Neural Net is:

- Mass of the two b-tagged jets ($M(bb)$)
- Mass of the two non b-tagged jets ($M(qq)$)
- cosine of the leading-jet scattering angle in the 4-jet rest-frame ($\cos(\theta_3)$)
- Chi
- Jet Width Tower of leading non b-jet
- Jet Width Track of leading non b-jet
- Jet Width Tower of second leading non b-jet
- Jet Width Track of second leading non b-jet
- Aplanarity, Sphericity and Centrality
- ΔR of the two b-tagged jets
- ΔR of the two non b-tagged jets
- Difference between the two ϕ angles of the two b-tagged jets
- Difference between the two ϕ angles of the two non b-tagged jets
- Neural Network distribution for the identification of WH non b-jet
- Neural Network distribution for the identification of ZH non b-jet

The definition for $\cos(\theta_3)$ can be found in [12]

The Chi variable is defined as:

$$Chi = \mathrm{Min}(Chi_W, Chi_Z) \quad (7)$$

$$Chi_{W/Z} = \sqrt{(M_{W/Z} - M_{qq})^2 + (M_H - M_{bb})^2} \quad (8)$$

Figure 38 and 39 show the signal & background plots for the selected variables and the modelling by the Tag-Rate-Function (TRF) are shown in figures 40-47 for SS category and figures 48- 55 for SJ category.

The neural net is trained with the selected 17 variables with the settings given in section 7.

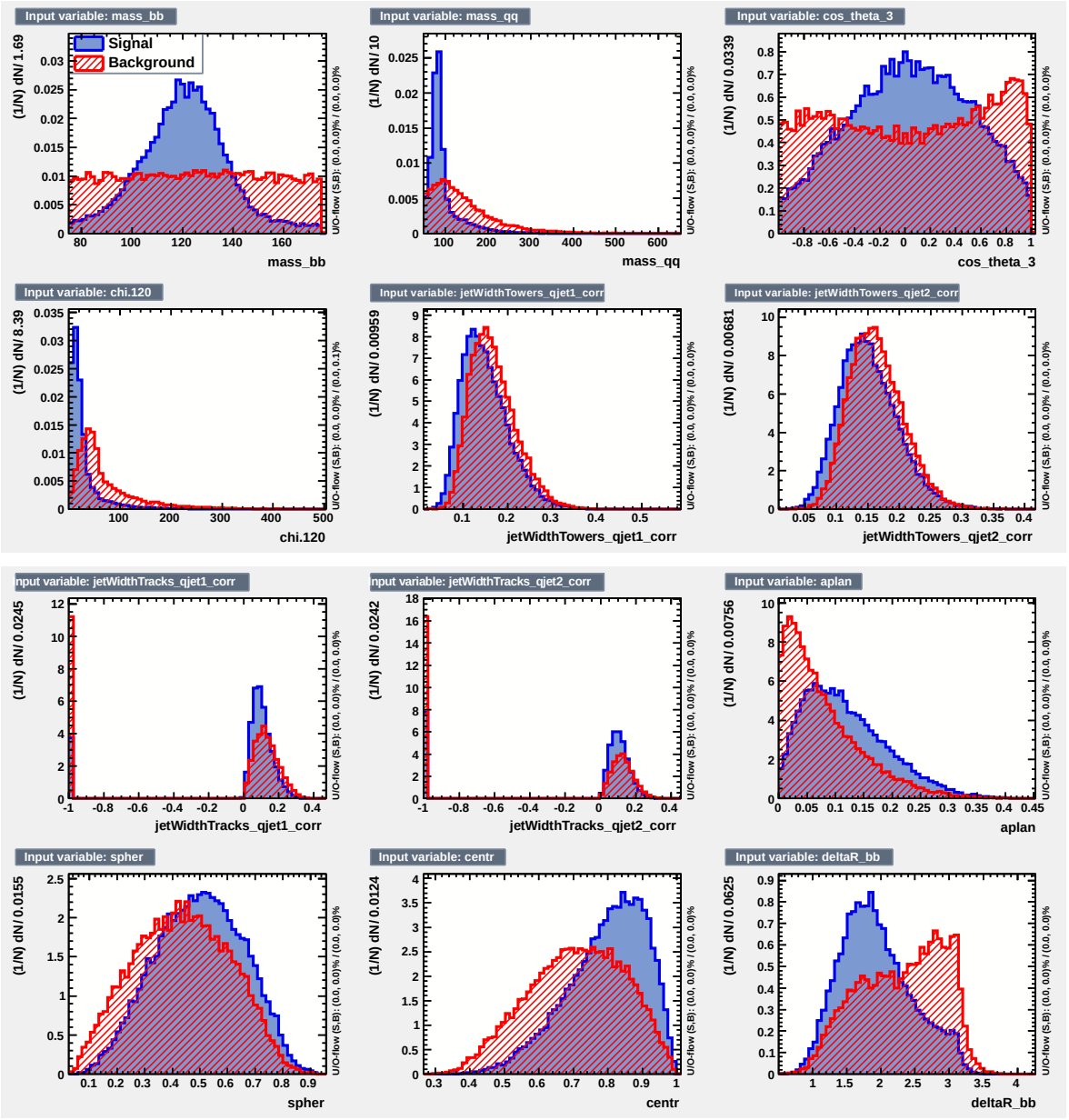

Figure 38: The training variables used for the VH analysis. WH(MH120) is used as the signal.

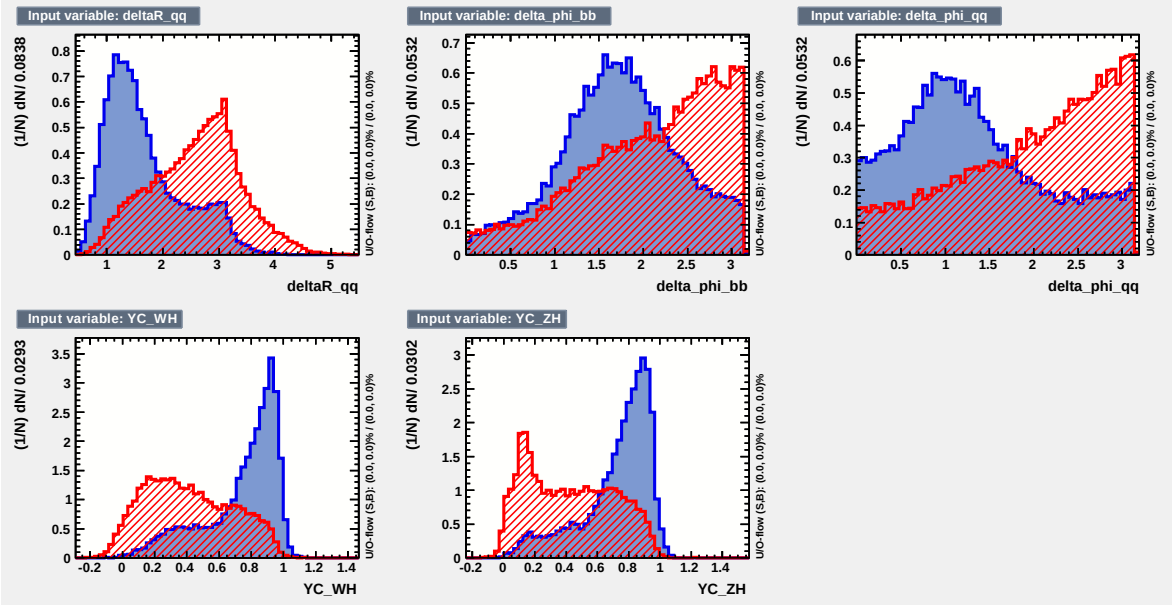

Figure 39: The training variables used for the VH analysis. WH(MH120) is used as the signal.

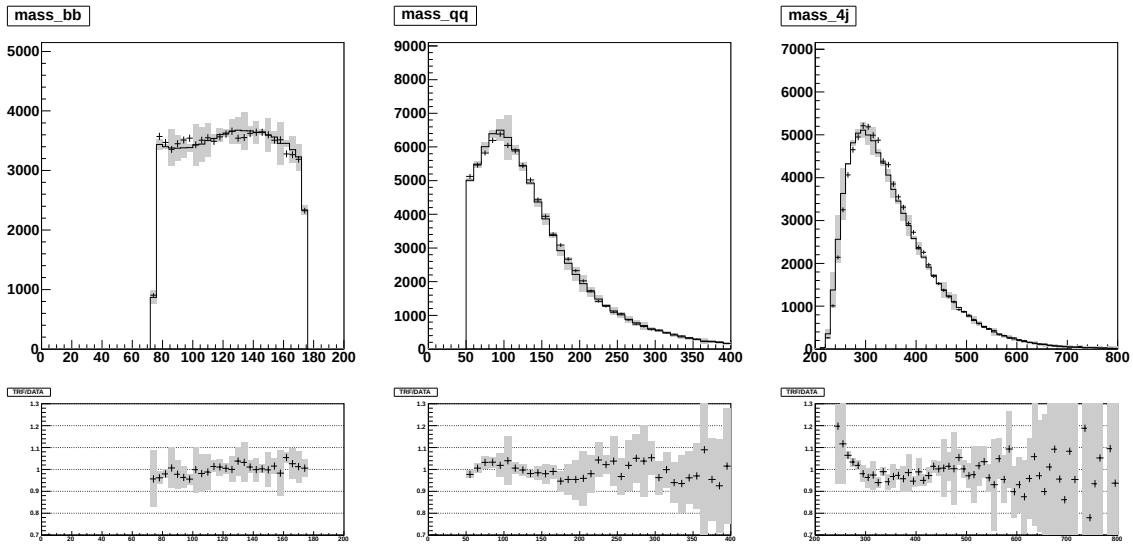

Figure 40: The SS TRF prediction of the training variables. The black histograms are the TRF prediction, the black crosses are the data for the Higgs signal region and the grey bar are the total uncertainty. As the TRF only predicts the shape, the histograms are normalised to unit area. Below the histograms are the ratio plots of Prediciton/Data. Variables which are modelled by the TRF have a flat ratio.

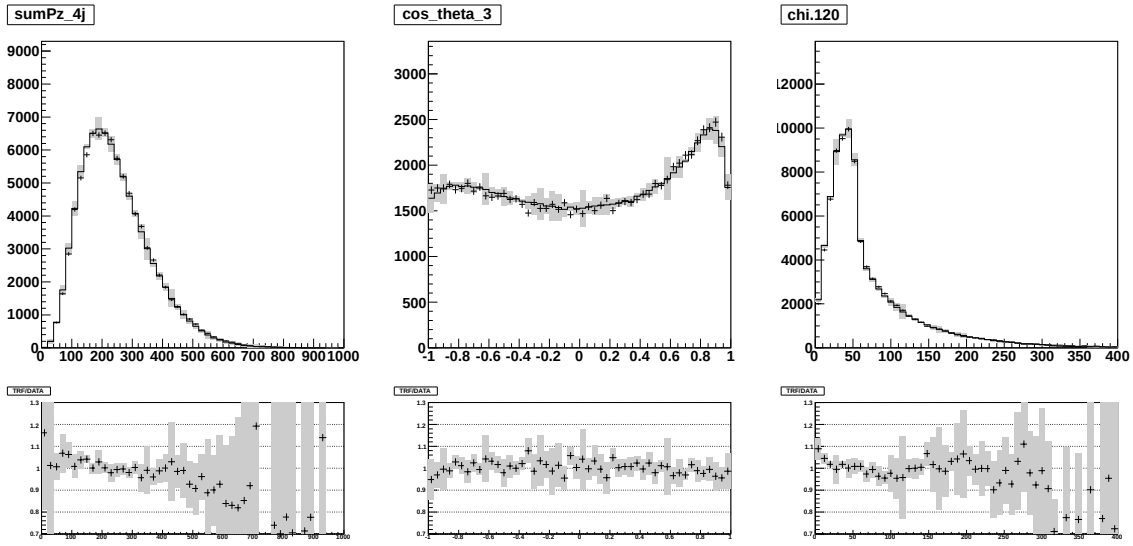

Figure 41: The SS TRF prediction of the training variables. The black histograms are the TRF prediction, the black crosses are the data for the Higgs signal region and the grey bar are the total uncertainty. As the TRF only predicts the shape, the histograms are normalised to unit area. Below the histograms are the ratio plots of Prediciton/Data. Variables which are modelled by the TRF have a flat ratio.

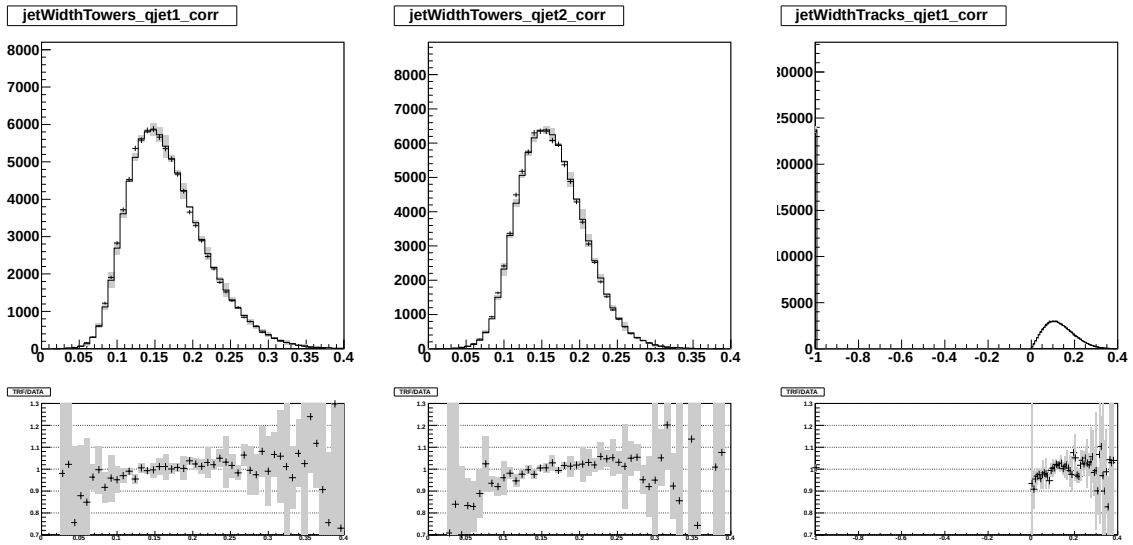

Figure 42: The SS TRF prediction of the training variables. The black histograms are the TRF prediction, the black crosses are the data for the Higgs signal region and the grey bar are the total uncertainty. As the TRF only predicts the shape, the histograms are normalised to unit area. Below the histograms are the ratio plots of Prediciton/Data. Variables which are modelled by the TRF have a flat ratio.

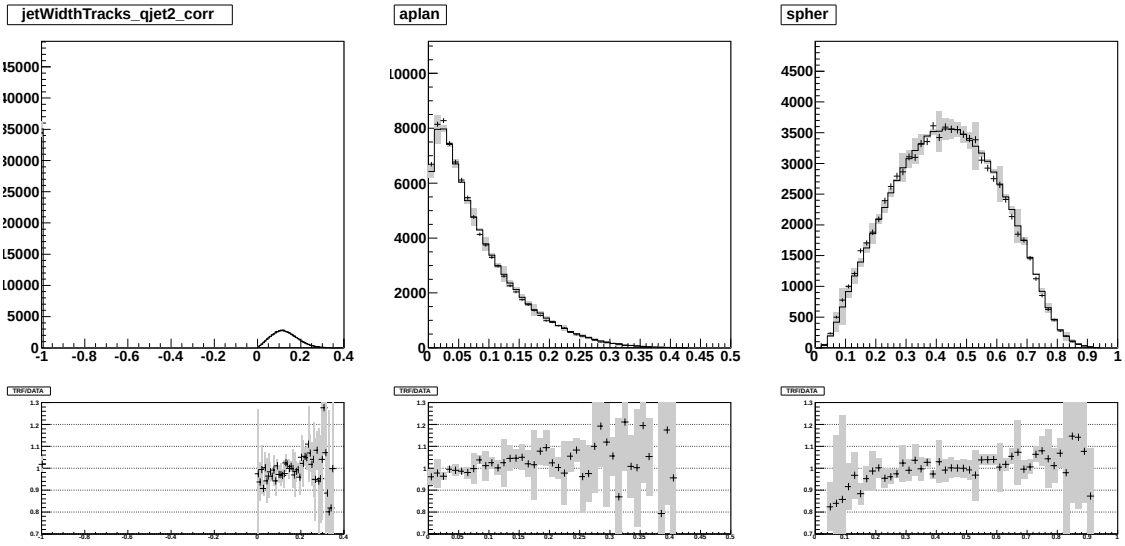

Figure 43: The SS TRF prediction of the training variables. The black histograms are the TRF prediction, the black crosses are the data for the Higgs signal region and the grey bar are the total uncertainty. As the TRF only predicts the shape, the histograms are normalised to unit area. Below the histograms are the ratio plots of Prediciton/Data. Variables which are modelled by the TRF have a flat ratio.

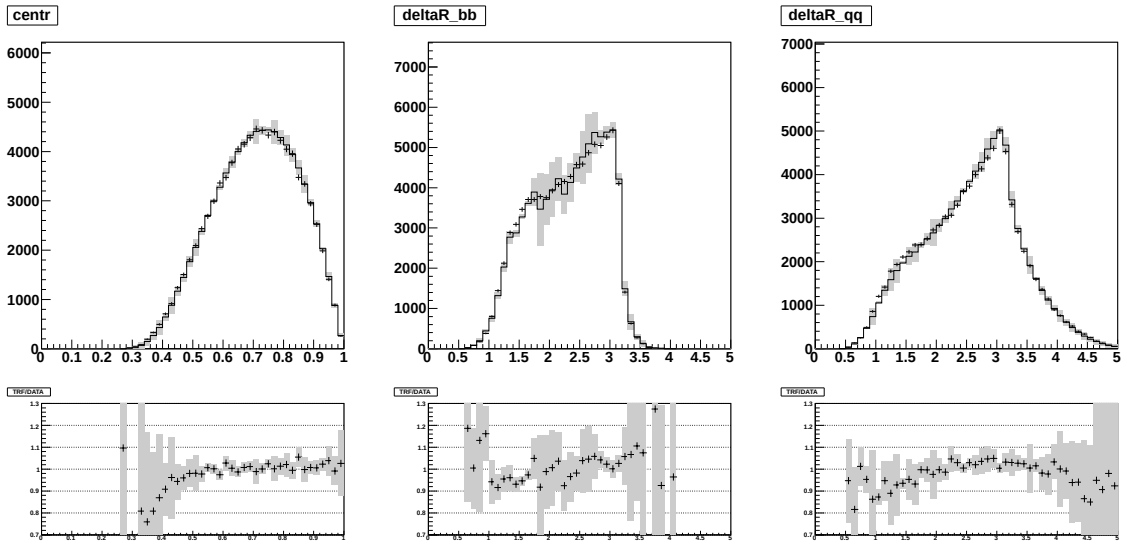

Figure 44: The SS TRF prediction of the training variables. The black histograms are the TRF prediction, the black crosses are the data for the Higgs signal region and the grey bar are the total uncertainty. As the TRF only predicts the shape, the histograms are normalised to unit area. Below the histograms are the ratio plots of Prediciton/Data. Variables which are modelled by the TRF have a flat ratio.

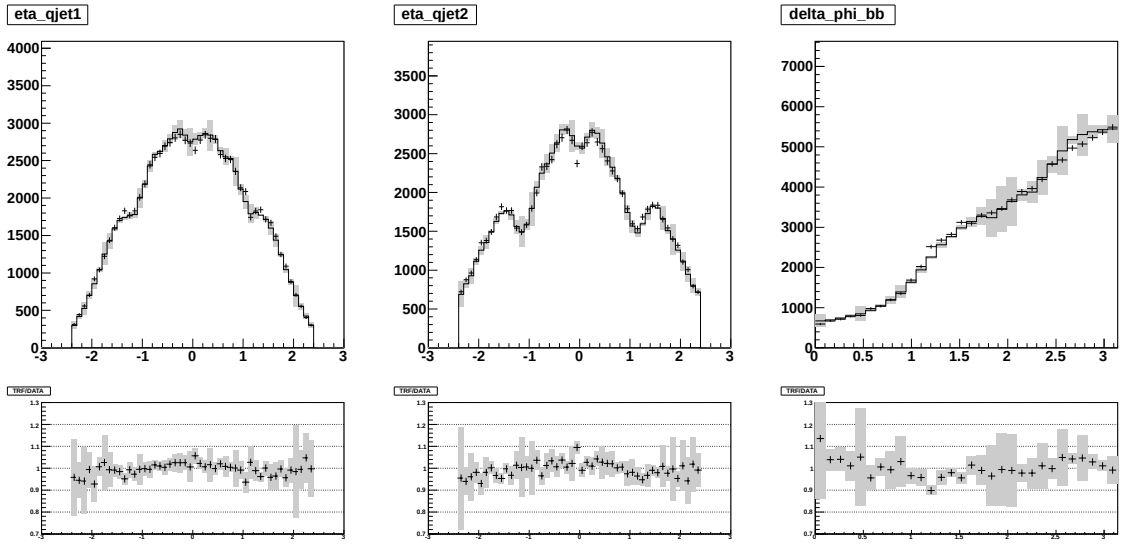

Figure 45: The SS TRF prediction of the training variables. The black histograms are the TRF prediction, the black crosses are the data for the Higgs signal region and the grey bar are the total uncertainty. As the TRF only predicts the shape, the histograms are normalised to unit area. Below the histograms are the ratio plots of Prediciton/Data. Variables which are modelled by the TRF have a flat ratio.

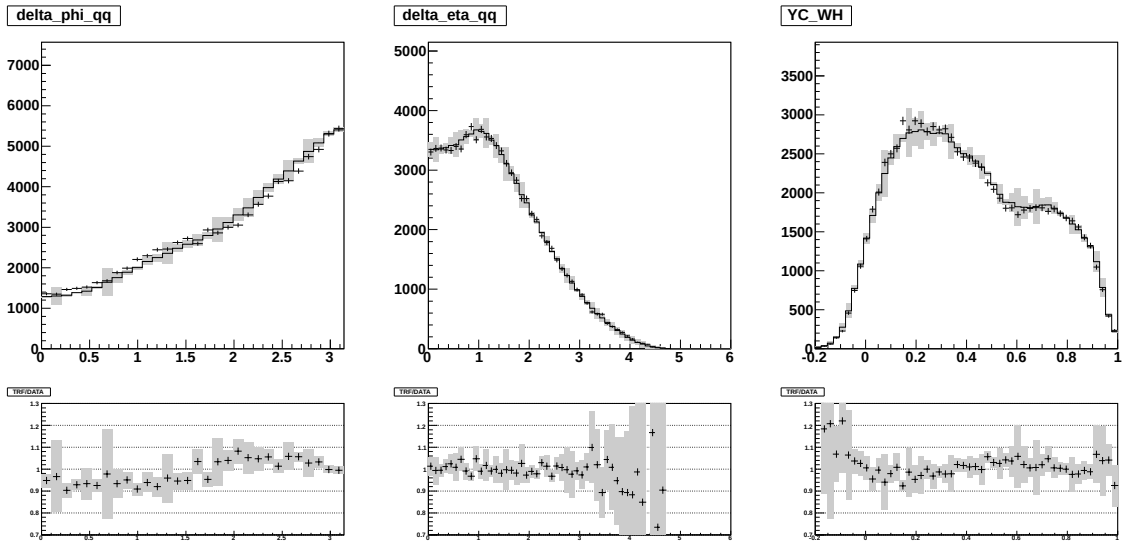

Figure 46: The SS TRF prediction of the training variables. The black histograms are the TRF prediction, the black crosses are the data for the Higgs signal region and the grey bar are the total uncertainty. As the TRF only predicts the shape, the histograms are normalised to unit area. Below the histograms are the ratio plots of Prediciton/Data. Variables which are modelled by the TRF have a flat ratio.

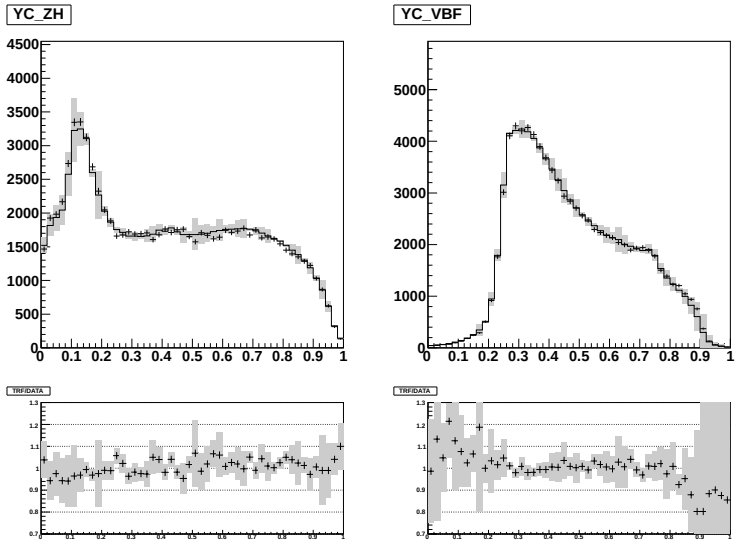

Figure 47: The SS TRF prediction of the training variables. The black histograms are the TRF prediction, the black crosses are the data for the Higgs signal region and the grey bar are the total uncertainty. As the TRF only predicts the shape, the histograms are normalised to unit area. Below the histograms are the ratio plots of Prediciton/Data. Variables which are modelled by the TRF have a flat ratio.

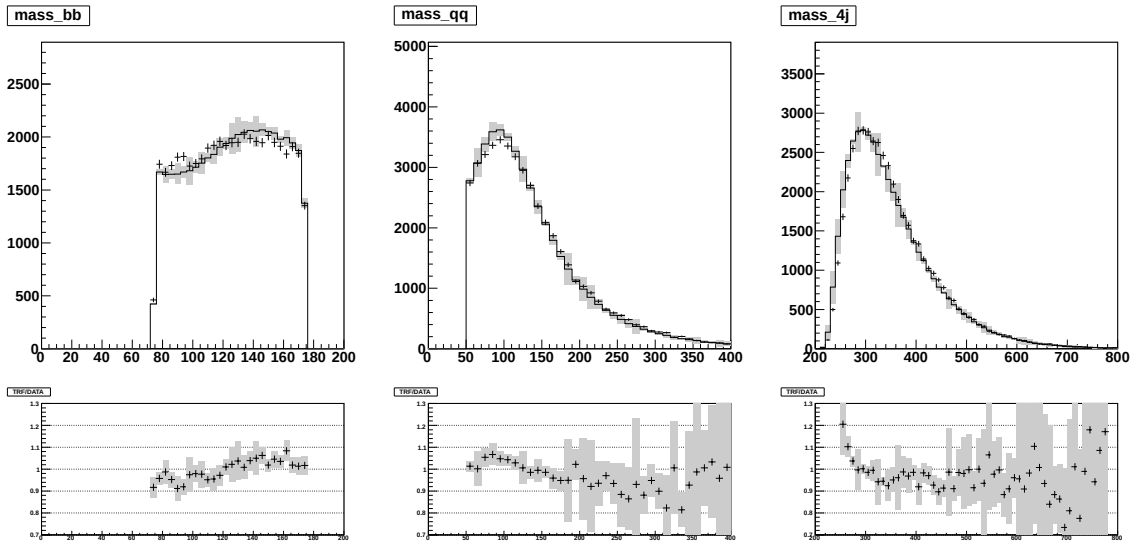

Figure 48: The SJ TRF prediction of the training variables. The black histograms are the TRF prediction, the black crosses are the data for the Higgs signal region and the grey bar are the total uncertainty. As the TRF only predicts the shape, the histograms are normalised to unit area. Below the histograms are the ratio plots of Prediciton/Data. Variables which are modelled by the TRF have a flat ratio.

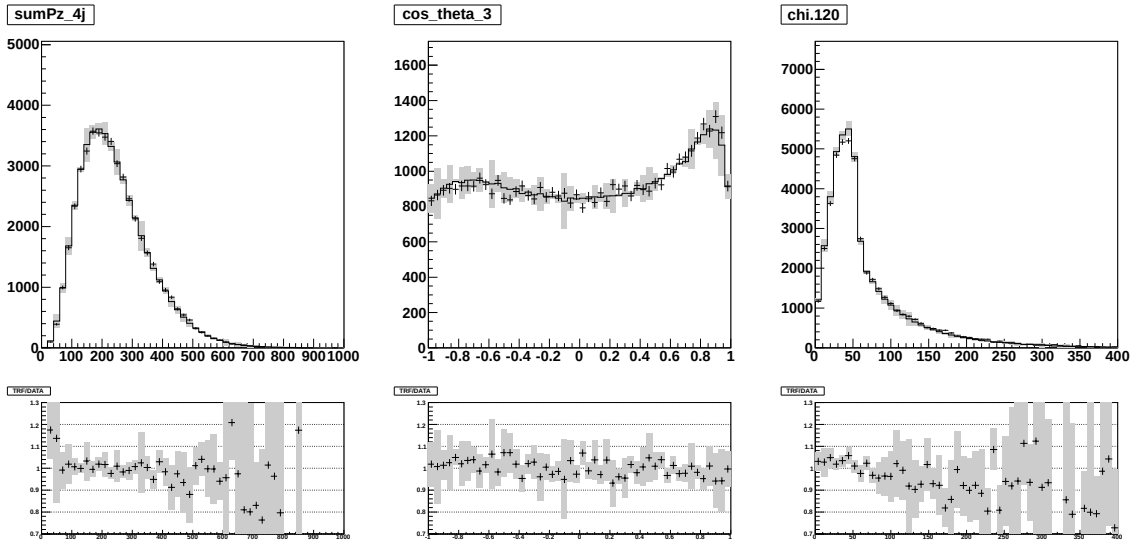

Figure 49: The SJ TRF prediction of the training variables. The black histograms are the TRF prediction, the black crosses are the data for the Higgs signal region and the grey bar are the total uncertainty. As the TRF only predicts the shape, the histograms are normalised to unit area. Below the histograms are the ratio plots of Prediciton/Data. Variables which are modelled by the TRF have a flat ratio.

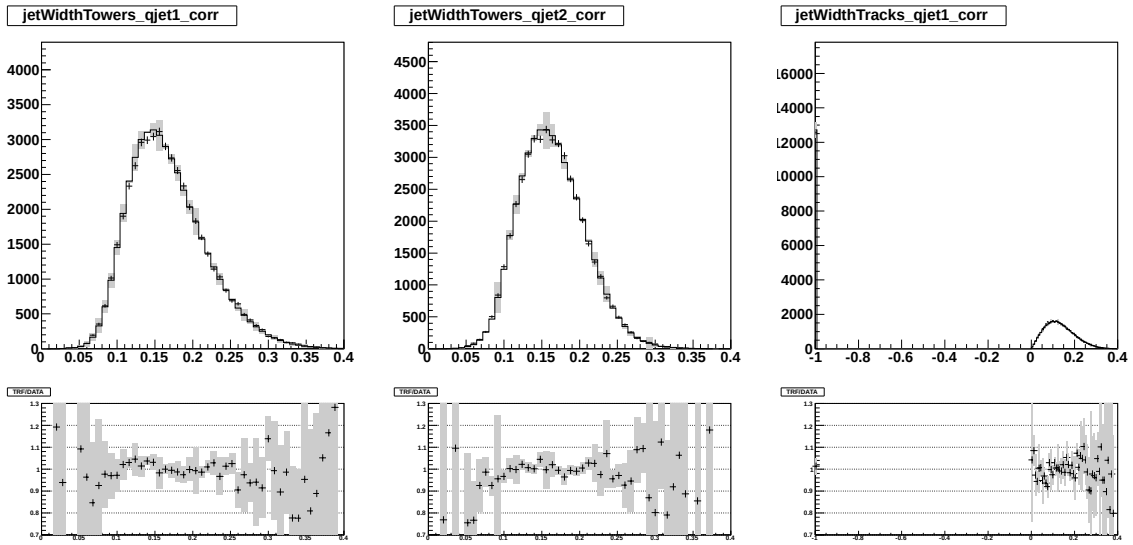

Figure 50: The SJ TRF prediction of the training variables. The black histograms are the TRF prediction, the black crosses are the data for the Higgs signal region and the grey bar are the total uncertainty. As the TRF only predicts the shape, the histograms are normalised to unit area. Below the histograms are the ratio plots of Prediciton/Data. Variables which are modelled by the TRF have a flat ratio.

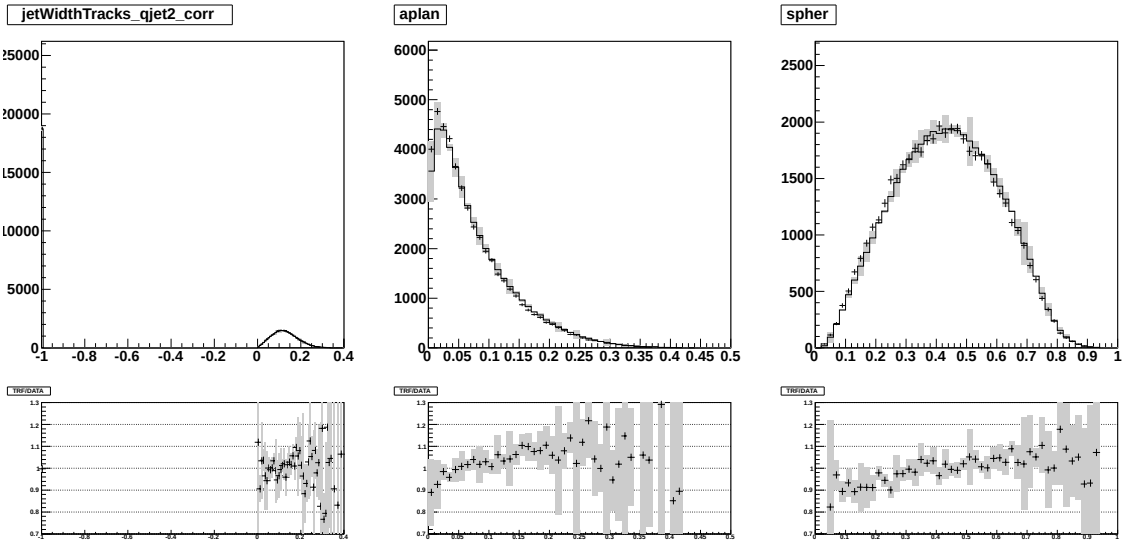

Figure 51: The SJ TRF prediction of the training variables. The black histograms are the TRF prediction, the black crosses are the data for the Higgs signal region and the grey bar are the total uncertainty. As the TRF only predicts the shape, the histograms are normalised to unit area. Below the histograms are the ratio plots of Prediciton/Data. Variables which are modelled by the TRF have a flat ratio.

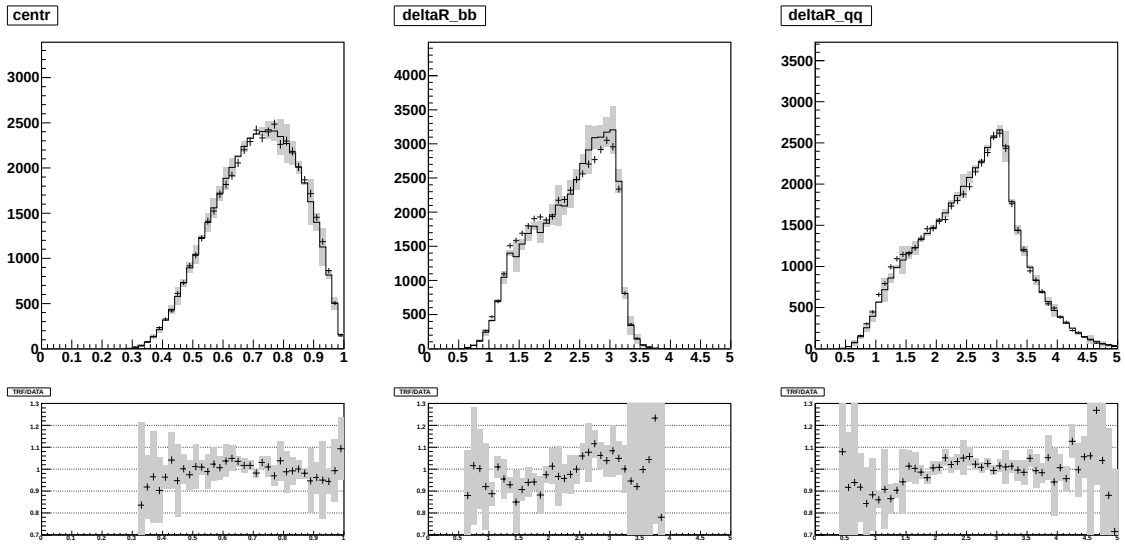

Figure 52: The SJ TRF prediction of the training variables. The black histograms are the TRF prediction, the black crosses are the data for the Higgs signal region and the grey bar are the total uncertainty. As the TRF only predicts the shape, the histograms are normalised to unit area. Below the histograms are the ratio plots of Prediciton/Data. Variables which are modelled by the TRF have a flat ratio.

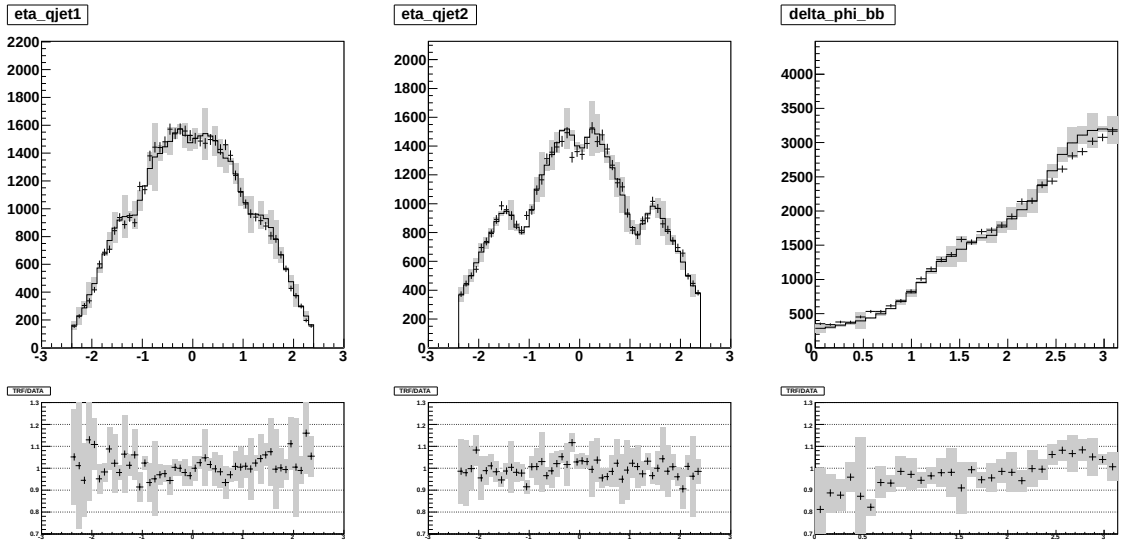

Figure 53: The SJ TRF prediction of the training variables. The black histograms are the TRF prediction, the black crosses are the data for the Higgs signal region and the grey bar are the total uncertainty. As the TRF only predicts the shape, the histograms are normalised to unit area. Below the histograms are the ratio plots of Prediciton/Data. Variables which are modelled by the TRF have a flat ratio.

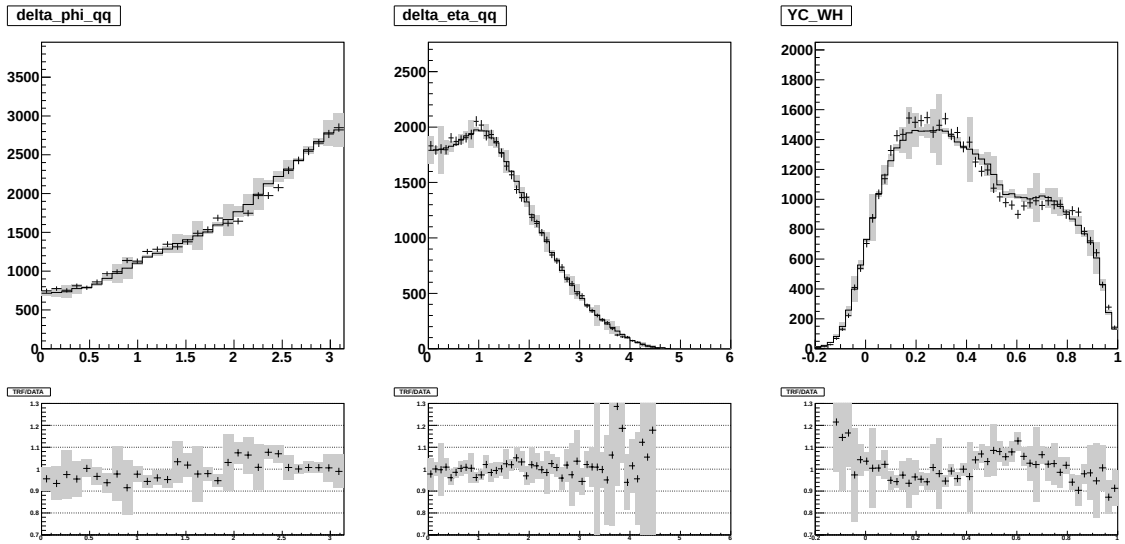

Figure 54: The SJ TRF prediction of the training variables. The black histograms are the TRF prediction, the black crosses are the data for the Higgs signal region and the grey bar are the total uncertainty. As the TRF only predicts the shape, the histograms are normalised to unit area. Below the histograms are the ratio plots of Prediciton/Data. Variables which are modelled by the TRF have a flat ratio.

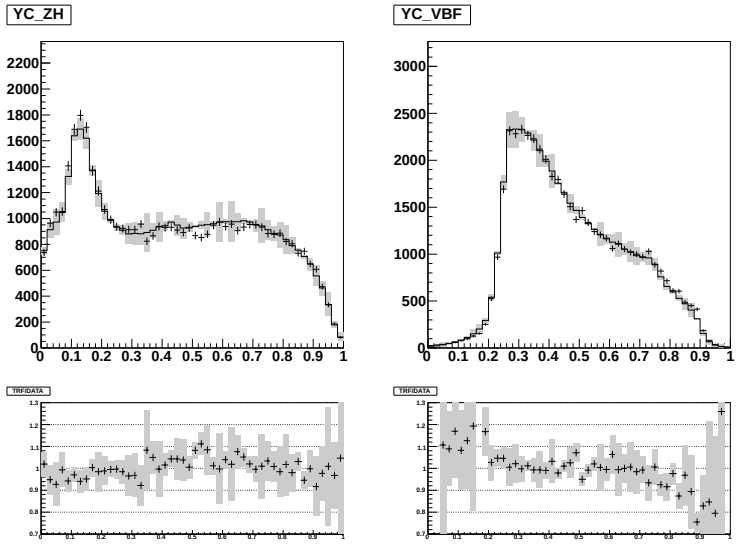

Figure 55: The SJ TRF prediction of the training variables. The black histograms are the TRF prediction, the black crosses are the data for the Higgs signal region and the grey bar are the total uncertainty. As the TRF only predicts the shape, the histograms are normalised to unit area. Below the histograms are the ratio plots of Prediciton/Data. Variables which are modelled by the TRF have a flat ratio.

7.2 VBF Neural Net Training

The VBF neural net is trained with the following samples:

- Signal : dedicated VBF training sample
- Background: the 10% 1-Tag background

Due to the different underlying physics process of the Vector Boson Fusion (VBF) compared to VH channel, we expect a different set of variables will be optimal for the VBF channel. The same variable selection procedure for VH was adopted for VBF. This resulted in 18 training variables for VBF:

- Mass of the two b-tagged jets ($M(bb)$)
- Mass of the two non b-tagged jets ($M(qq)$)
- Chi
- Jet Width Tower of leading non b-jet
- Jet Width Track of leading non b-jet
- Jet Width Tower of second leading non b-jet
- Jet Width Track of second leading non b-jet
- η of leading non b-jet
- η of second leading non b-jet
- Difference between the two η angles of the two b-tagged jets
- Invariant mass of four jets system
- Sum of momentum Z component of the four jets system
- Sphericity and Centrality
- ΔR of the two b-tagged jets
- ΔR of the two non b-tagged jets
- Difference between the two ϕ angles of the two b-tagged jets
- Neural Network distribution for the identification of VBF non b-jet

Fig. 56 57 show the signal and background plots for the selected variables and Figs.40-47 shows the TRF modelling of the NN training variables for SS category and figures 48-55 for the SJ category and Fig. 61(c) shows the overtraining check .

7.3 SuperDiscriminant Neural Net Training

For the SuperDiscriminant (SD) neural net training, the samples used were:

- Signal : WH, ZH and VBF NN training samples
- Background: the NN 10% 1-Tag background

The list of training variables is:

- Neural Net distribution for WH

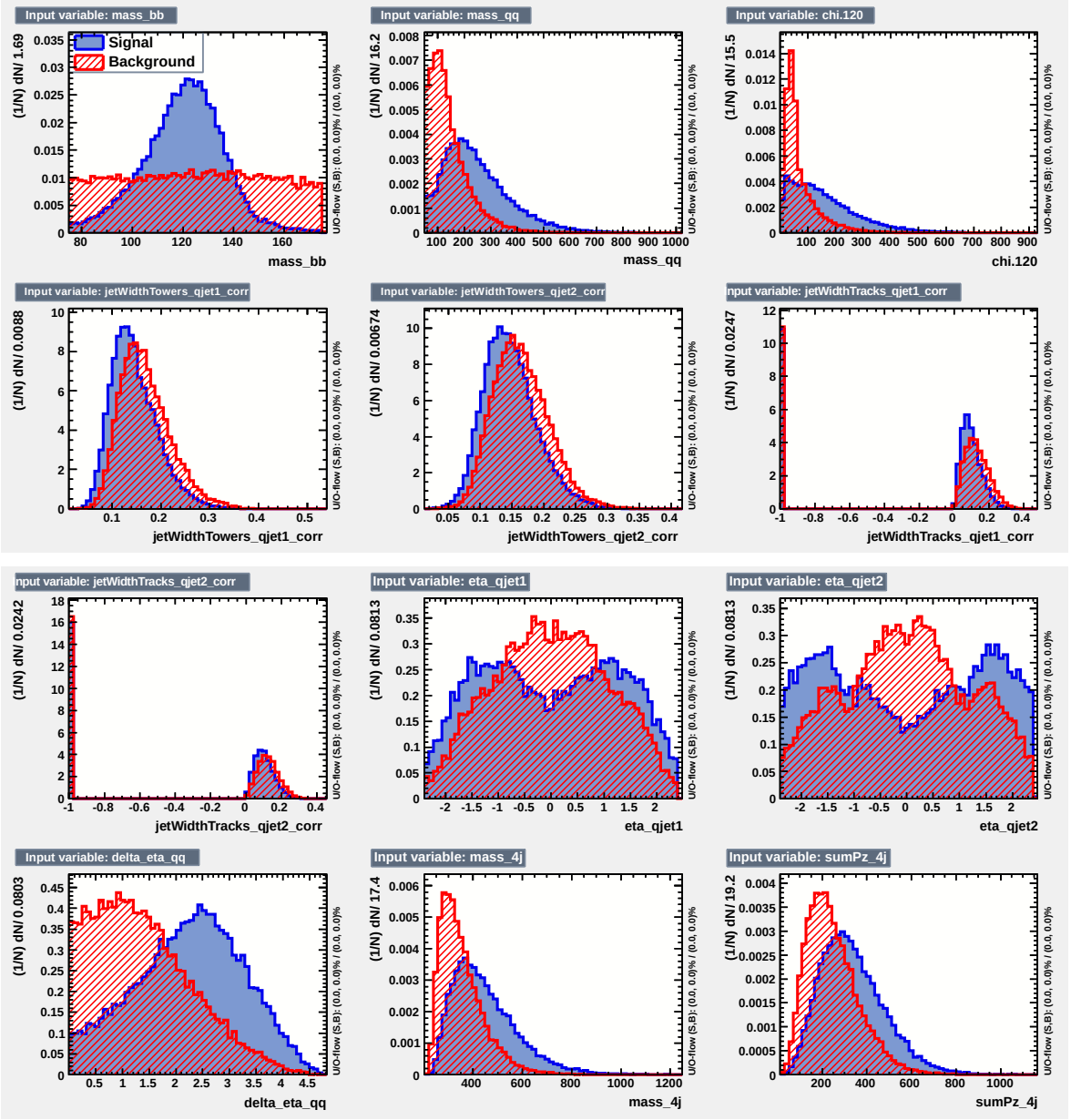

Figure 56: The training variables used for the VBF analysis. VBF(MH120) is used as the signal.

- Neural Net distribution for ZH
- Neural Net distribution for VBF

The figure 58 shows the signal & background plots for the selected variables and the figures 59 and 60 show the TRF modelling of NN training variables for MH120, analogous plots are obtained for MH100 and MH140. Figure 61 shows the overtraining for the four neural nets.

For any multivariate analysis, one must ensure their classifier is not overtrained. Otherwise it would lead to an overoptimistic performance of the classifier. A measure of the over-training is to compare the Neural Net distribution using events used for training & events from an independent test

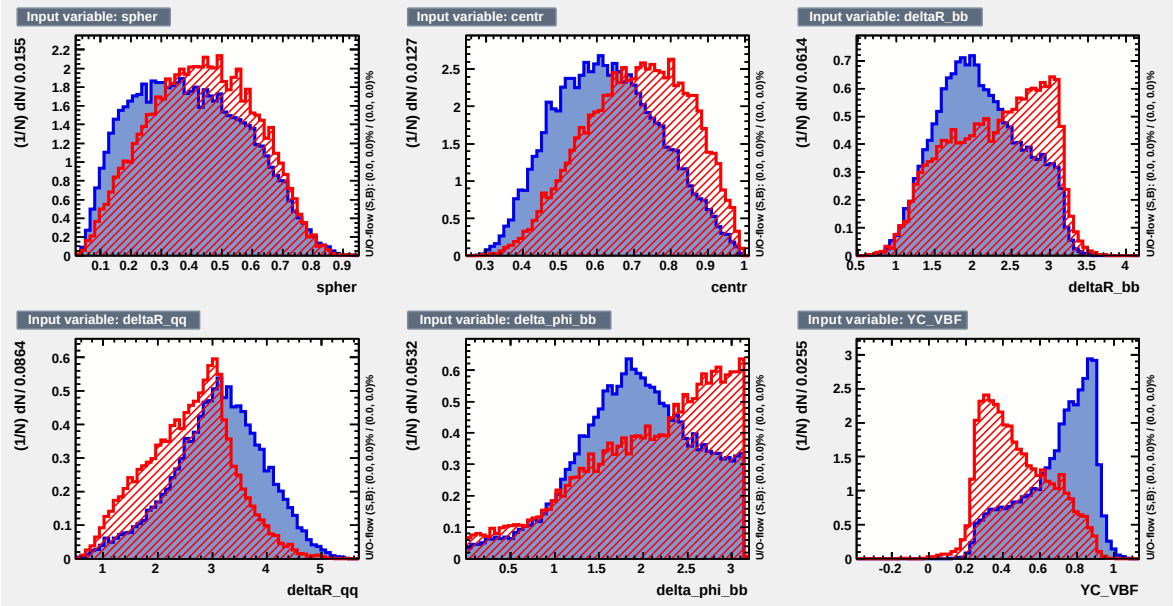

Figure 57: The training variables used for the VBF analysis. VBF(MH120) is used as the signal.

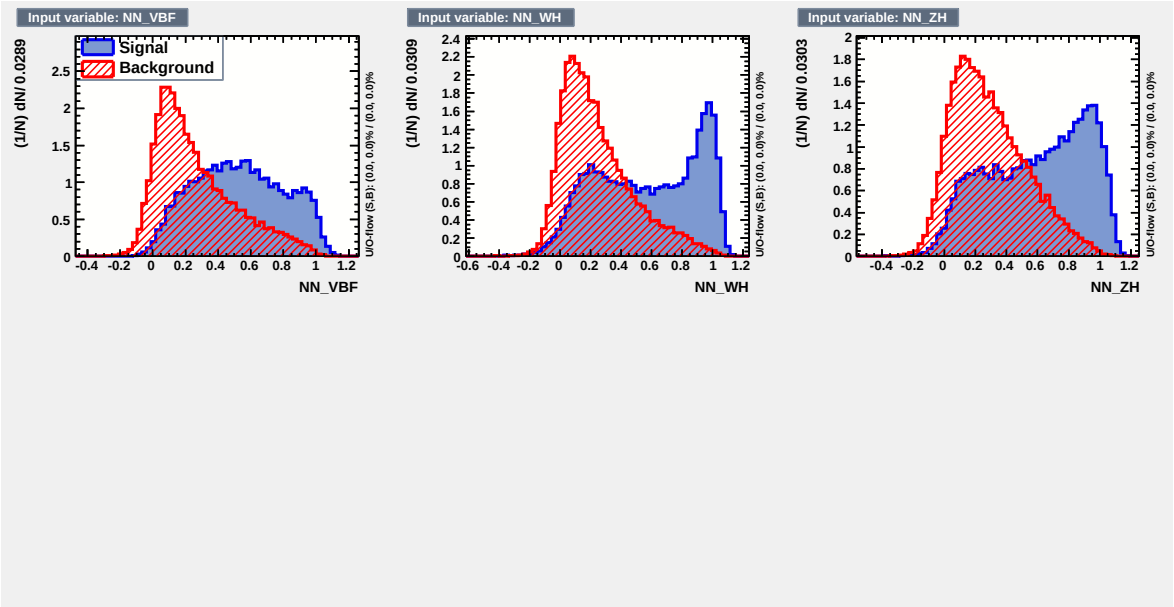

Figure 58: The training variables used for the SD analysis. MH120 training is used.

sample. The TMVA package provides such a test and reports the Kolmargorov-Smirnoff probabilties for the signal & background. The values for various training are in table 7.

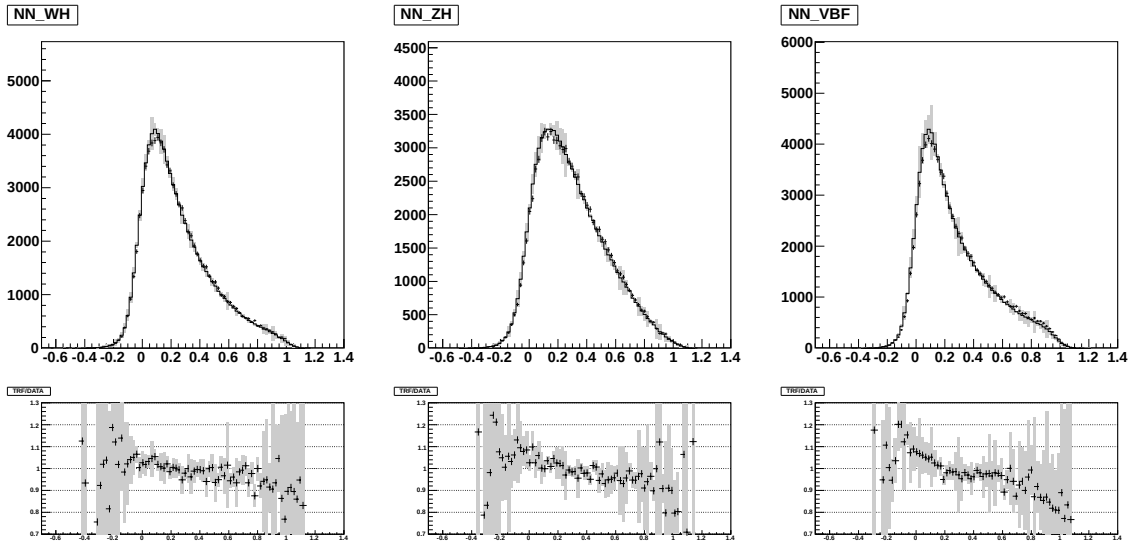

Figure 59: The SS TRF prediction of the training variables for SuperDiscriminat. The black histograms are the TRF prediction, the black crosses are the data for the Higgs signal region and the grey bar are the total uncertainty. As the TRF only predicts the shape, the histograms are normalised to unit area. Below the histograms are the ratio plots of Prediciton/Data. Variables which are modelled by the TRF have a flat ratio.

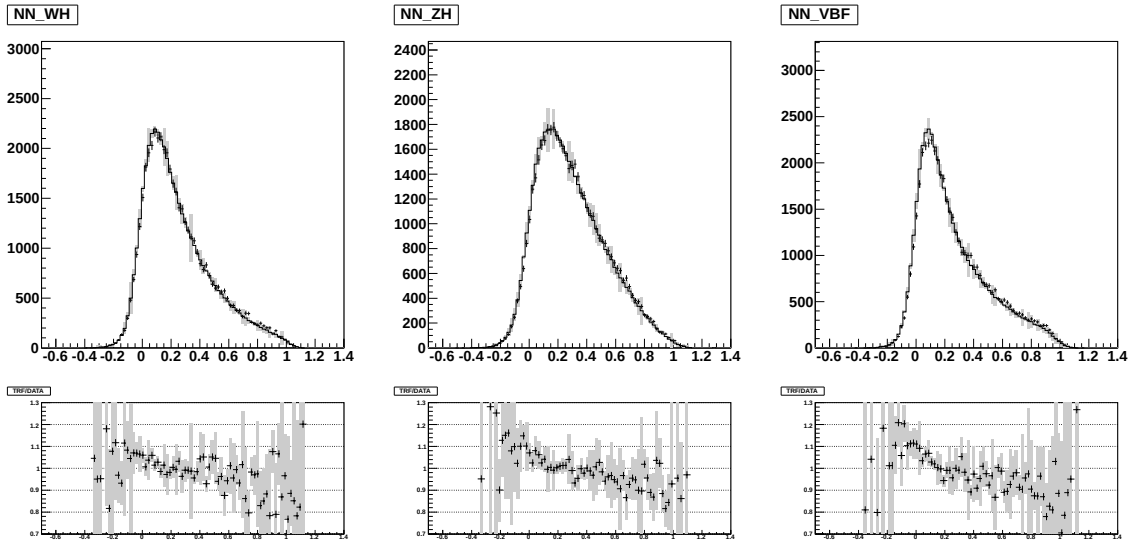

Figure 60: The SJ TRF prediction of the training variables for SuperDiscriminat. The black histograms are the TRF prediction, the black crosses are the data for the Higgs signal region and the grey bar are the total uncertainty. As the TRF only predicts the shape, the histograms are normalised to unit area. Below the histograms are the ratio plots of Prediciton/Data. Variables which are modelled by the TRF have a flat ratio.

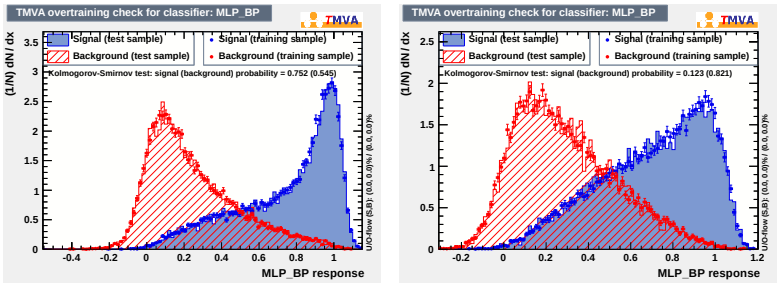

(a) Overtraining check for WH (b) Overtraining check for ZH

(c) Overtraining check for VBF (d) Overtraining check for SD

Figure 61: Overtraining checks for WH, ZH, VBF & SD trained for MH120. All trained neural nets give good Kolmorogov-Smirnoff probabilities which indicates no overtraining.

NN Train	Signal (%)	Background (%)
WH	75.2	54.5
ZH	12.3	82.1
VBF	83.5	6.3
SuperDiscriminant	45.9	96.7

Table 7: Kolmogorov-Smirnoff probabilities for signal and background for each Neural Network training for a MH120 signal

7.4 NN Templates

7.4.1 MH100 Neural Network

The NN trained with m_H=100 GeV/c^2 is used to search for Higgs bosons of mass m_H=100 GeV/c^2. Figure 62 shows the NN output for the background and m_H=100 GeV/c^2 Higgs signal.

7.4.2 MH120 Neural Network

The NN trained with m_H=120 GeV/c^2 is used to search for Higgs bosons of mass m_H=105 GeV/c^2 to 130 GeV/c^2. Figure 63 shows the NN output for the background and m_H=120 GeV/c^2 Higgs signal. The m_H=105,110,115,125,130 GeV/c^2 Higgs uses the same background templates and just replaces the Higgs signal (Fig. 64- 68).

7.4.3 MH140 Neural Network

The NN trained with m_H=140 GeV/$c^2$is used to search for Higgs bosons of mass m_H=135 GeV/c^2 to 150 GeV/c^2. Figure 69 shows the NN output for the background and m_H=140 GeV/c^2 Higgs signal.

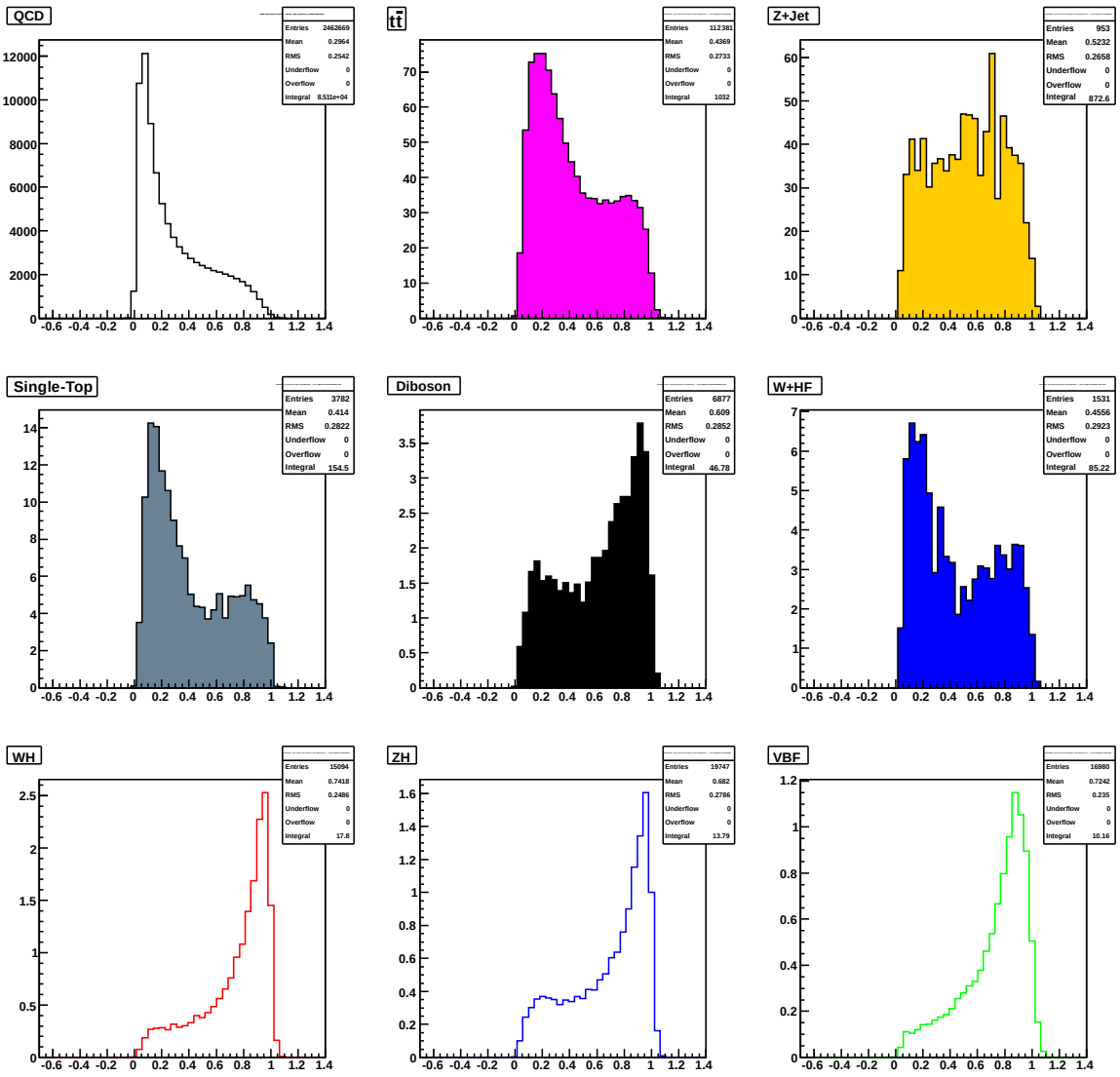

Figure 62: Background and Higgs signal (m_H=100 GeV/c^2) distributions for NN trained at m_H=100 GeV/c^2. For this low mass, the diboson background has a very signal like distribution.

The m_H=135,145,150 GeV/c^2 Higgs uses the same background templates and just replaces the Higgs signal (Fig. 70- 72).

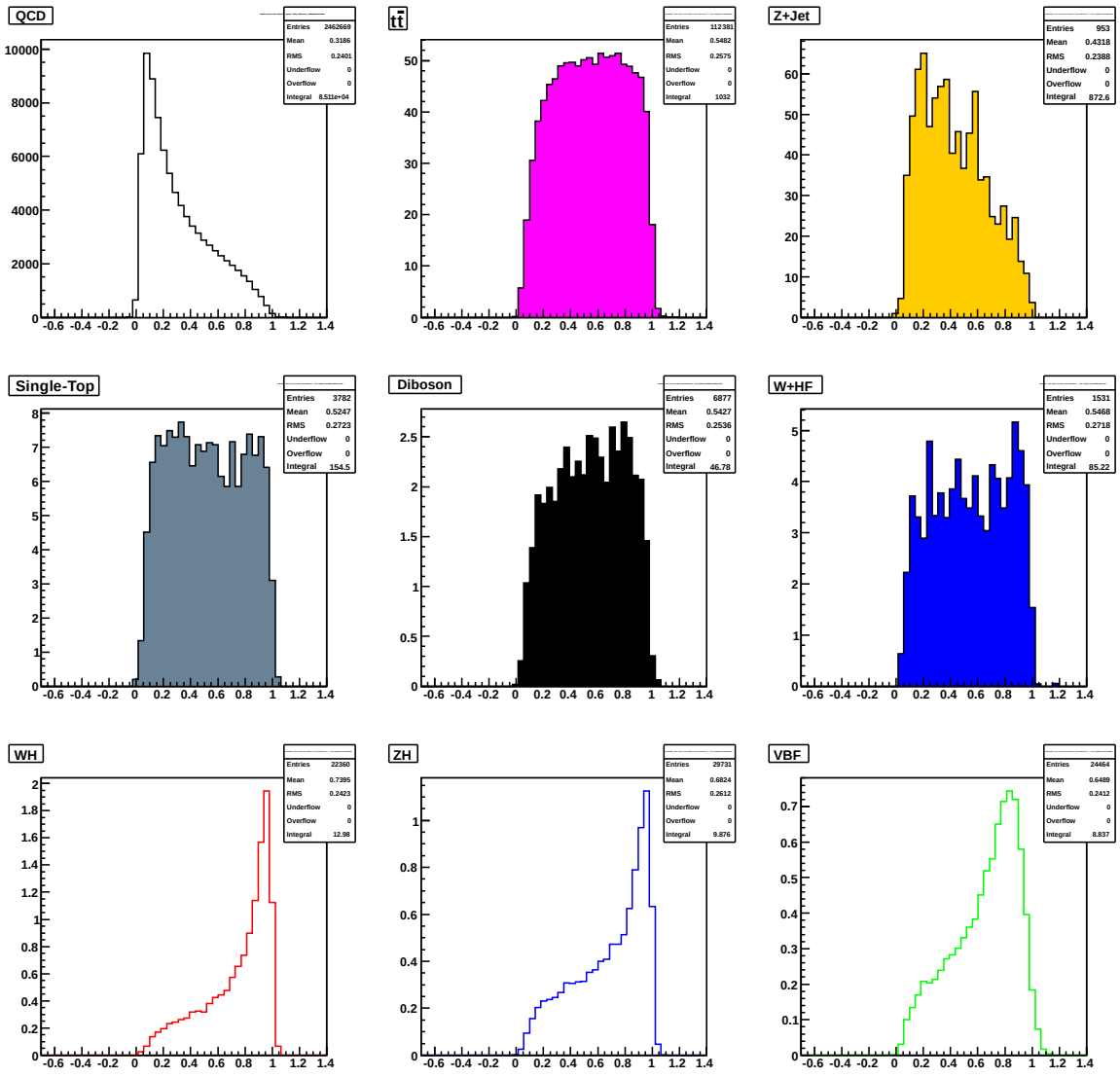

Figure 63: Background and Higgs signal (m_H=120 GeV/c^2) distributions for NN trained at m_H=120 GeV/c^2.

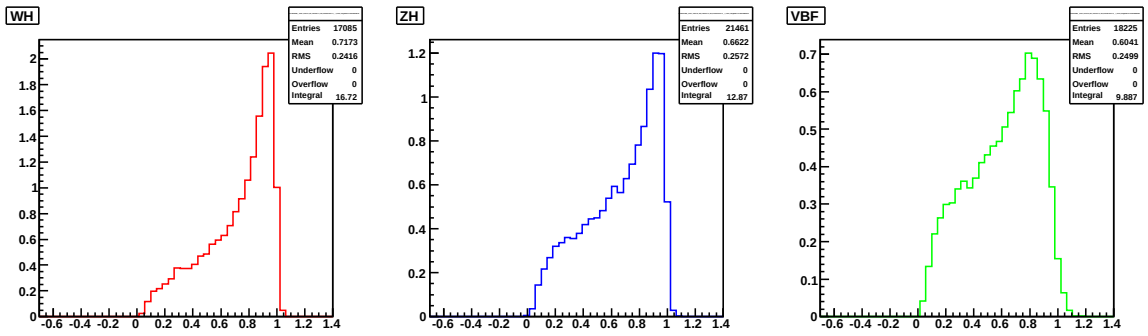

Figure 64: NN distributions for m_H=105 GeV/c^2 using the NN trained at m_H=120 GeV/c^2

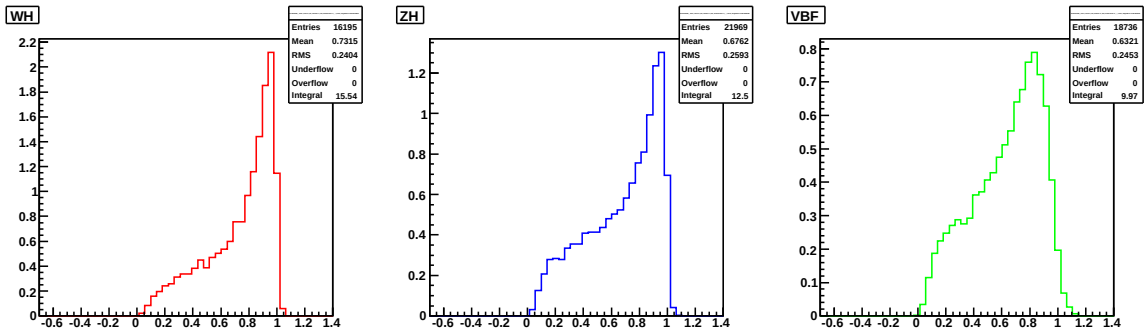

Figure 65: NN distributions for m_H=110 GeV/c^2 using the NN trained at m_H=120 GeV/c^2

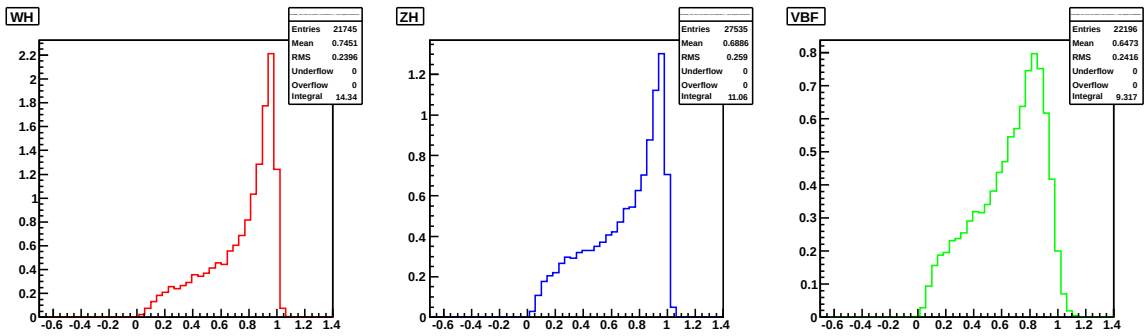

Figure 66: NN distributions for m_H=115 GeV/c^2 using the NN trained at m_H=120 GeV/c^2

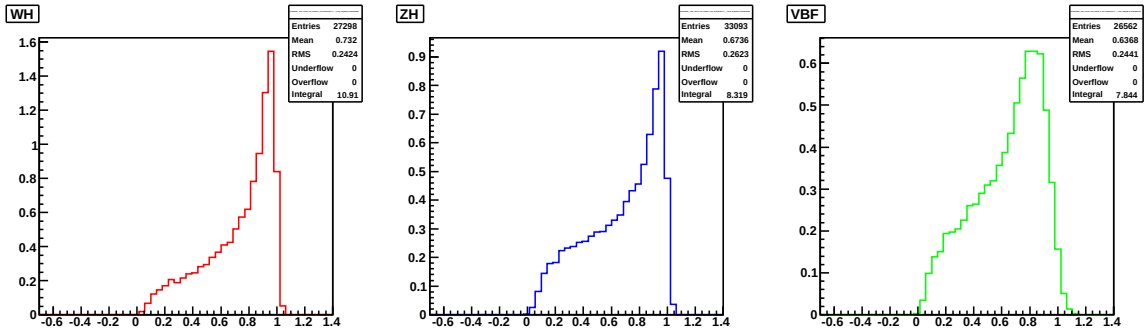

Figure 67: NN distributions for m_H=125 GeV/c^2 using the NN trained at m_H=120 GeV/c^2

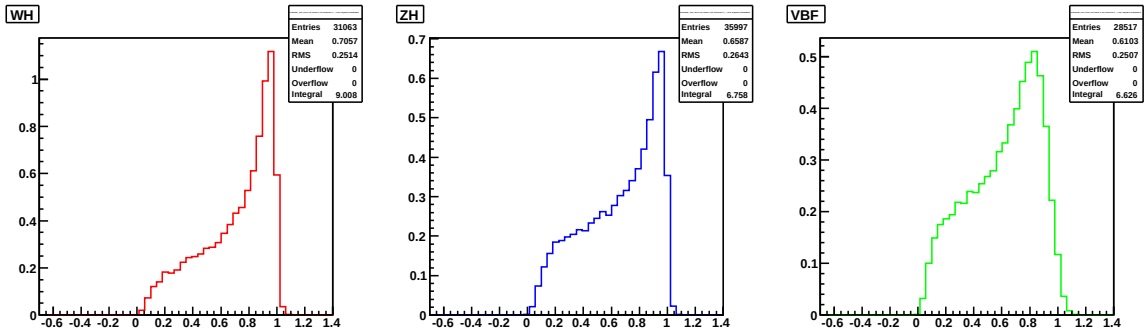

Figure 68: NN distributions for m_H=130 GeV/c^2 using the NN trained at m_H=120 GeV/c^2

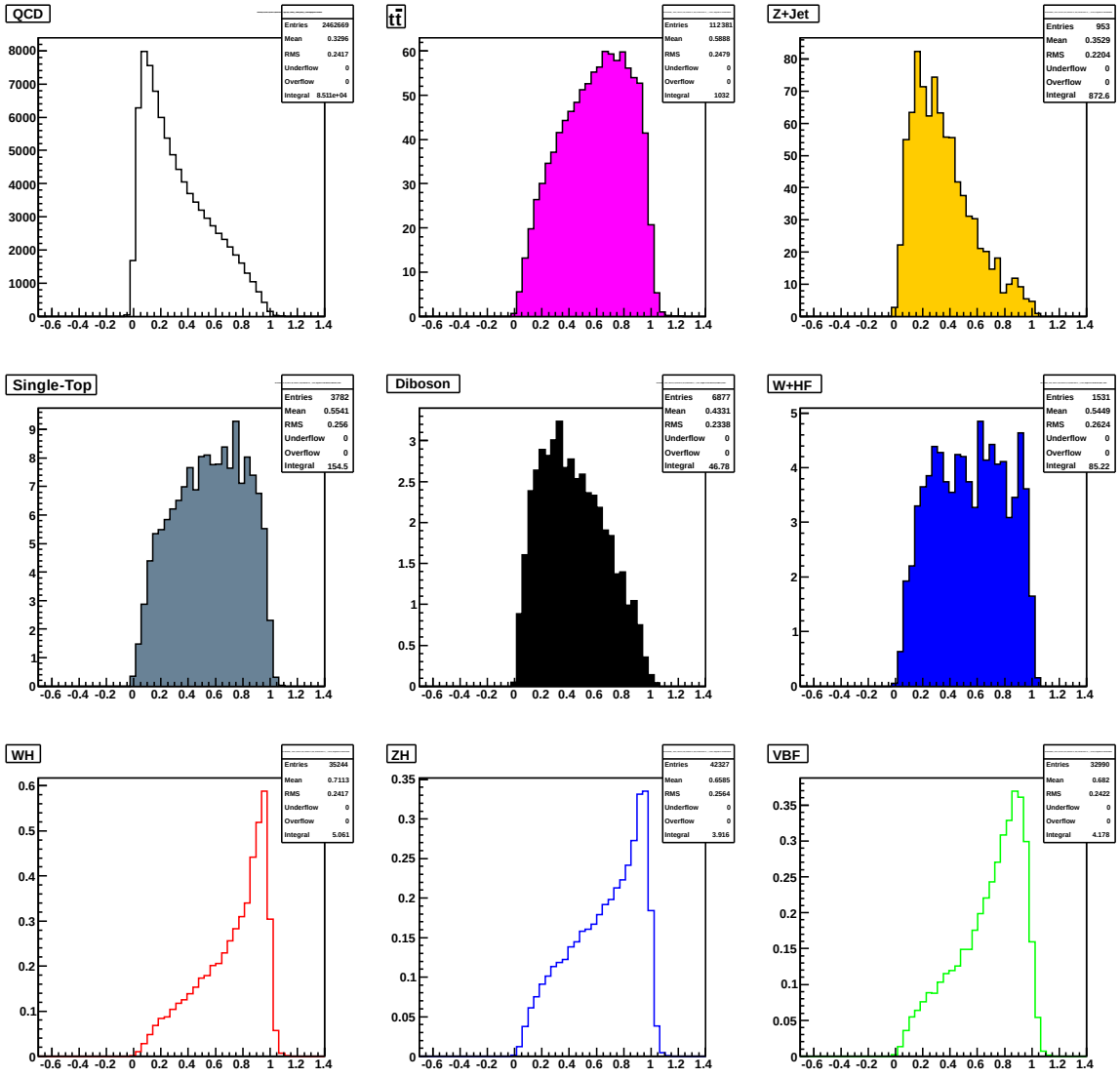

Figure 69: Background and Higgs signal (m_H=140 GeV/c^2) distributions for NN trained at m_H=140 GeV/c^2.

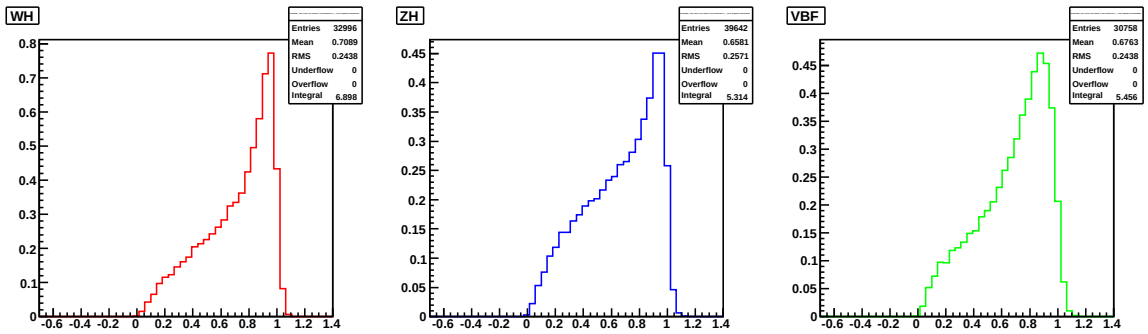

Figure 70: NN distributions for m_H=135 GeV/c^2 using the NN trained at m_H=140 GeV/c^2

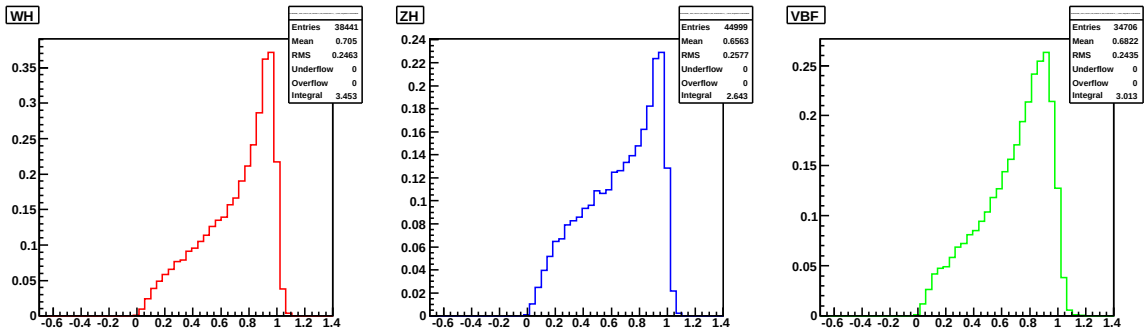

Figure 71: NN distributions for m_H=145 GeV/c^2 using the NN trained at m_H=140 GeV/c^2

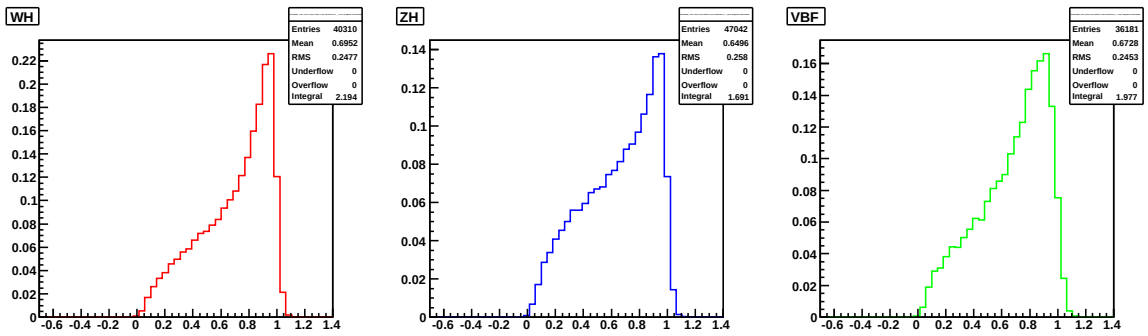

Figure 72: NN distributions for m_H=150 GeV/c^2 using the NN trained at m_H=140 GeV/c^2

8 Neural Network Output Tuning

The Super Discriminant Neural Network output presents a disagreement between Data and TRF prediction in the Higgs Signal Region (Fig. 73(b)). We also see a similar mismodelling for the VBF Neural Network output (Fig. 73(a)).

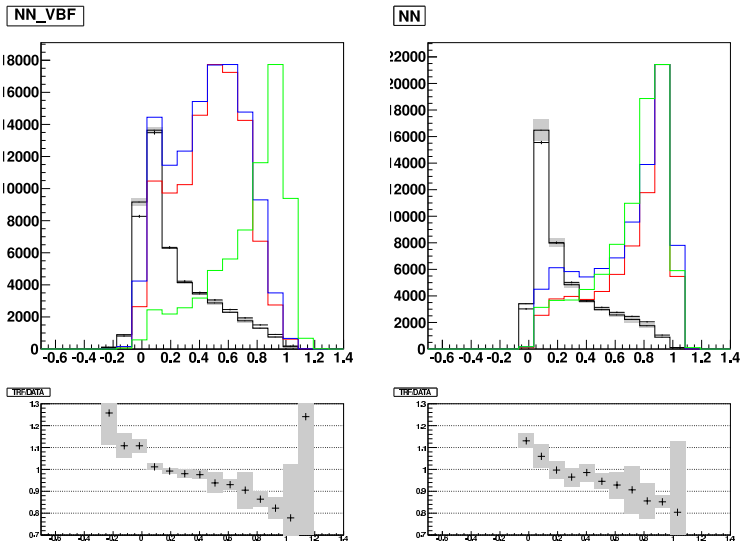

(a) Neural Network Output for VBF (b) Neural Network Output for SuperDiscriminant

Figure 73: Neural Network Output for the four Neural Network Training. The black histograms are the TRF prediction, the black crosses are the Data, the grey bar are the total uncercainties, the green histograms are the VBF signal sample, the red histograms are the WH signal samples and the blue histograms are the ZH signal samples. The TRF histograms is normalized to the DATA. Below the histograms are the ratio plots of Prediction/Data.

We correct the VBF Neural Network Output (NN_VBF) so to improve also the SD Neural Network Output (NN_SD). The idea is to apply a correction function measured in a No-Signal region to the Signal Region.

The two No-Signal Region we cosidered are (Fig.74):

- Tag Region
- NJet6 Region

The Tag Region is define as:

- 4 or 5 jets
- $65GeV < M_{bb} < 70GeV, M_{qq} > 40GeV$
- $70GeV < M_{bb} < 200GeV, 40GeV < M_{qq} < 45GeV$
- $200GeV < M_{bb} < 250GeV, M_{qq} > 40GeV$

and the NJet6 Region is define as:

- 6 jets

- $70GeV < M_{bb} < 75GeV$
- $M_{qq} > 50GeV$

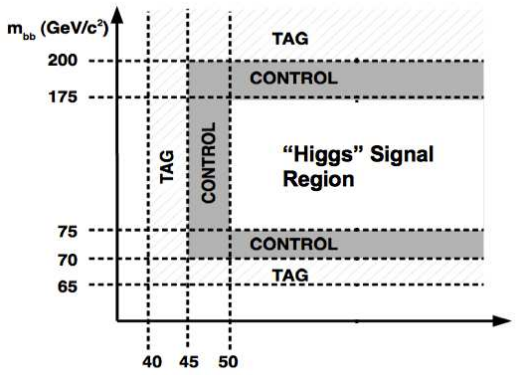

Figure 74: Analysis region in Mbb Mqq plane.

In the 2 No-Signal Region is present the same mis-modelling we see in the Signal Region (Fig. 75), so we assume that they have the same source. The correction function is the fit of the ratio between Data and TRF Prediction in a No-Signal Region and we use that fit values to reweight the TRF events, assuming that the same correction works also in Signal Region, we apply it in the Signal Region, if the NN_VBF present an improvment we also should see an improvment in NN_SD.

The function we used to fit the ratio between Data and TRF Prediction is a first order polynomial (y=y(NN_VBF)):

$$y = a_0 + a_1 x \tag{9}$$

We calculated the TRF correction function for all 3 mass point used for training: 100, 120 and 140GeV and for the 2 bjet categories: SS and SJ in the 2 No-Signal Region. To choose which correction to use, we applied each correction function fit to the TRF predict events in the Control Region (CTRL) and we measured the χ^2/NDF and the Kolmogorov-Smirnov value (KS-value) (Tab. 8) of corrected TRF prediction to Data. The function with best values is selected and we used the other one to estimate the systematic uncertainty.

(a) KS-value and χ^2/NDF in TAG Region

Samples	KS-value	χ^2/NDF
100 STST	0.69226	0.857104
100 STJP	0.258203	1.24795
120 STST	0.302658	0.822528
120 STJP	0.102873	1.24716
140 STST	0.18663	1.38333
140 STJP	0.262354	1.87248

(b) KS-value and χ^2/NDF in NJet6 Region

Samples	KS-value	χ^2/NDF
100 STST	0.0472725	1.24937
100 STJP	0.0152989	1.78886
120 STST	0.994325	0.646125
120 STJP	0.00010446	2.10496
140 STST	0.0565532	1.38517
140 STJP	0.0477932	2.01858

Table 8: Kolmogorv-Smirnov and χ^2/NDF values for TAG and NJet6 Region.

The CTRL Region is define as (Fig.74):

- 4 or 5 jets

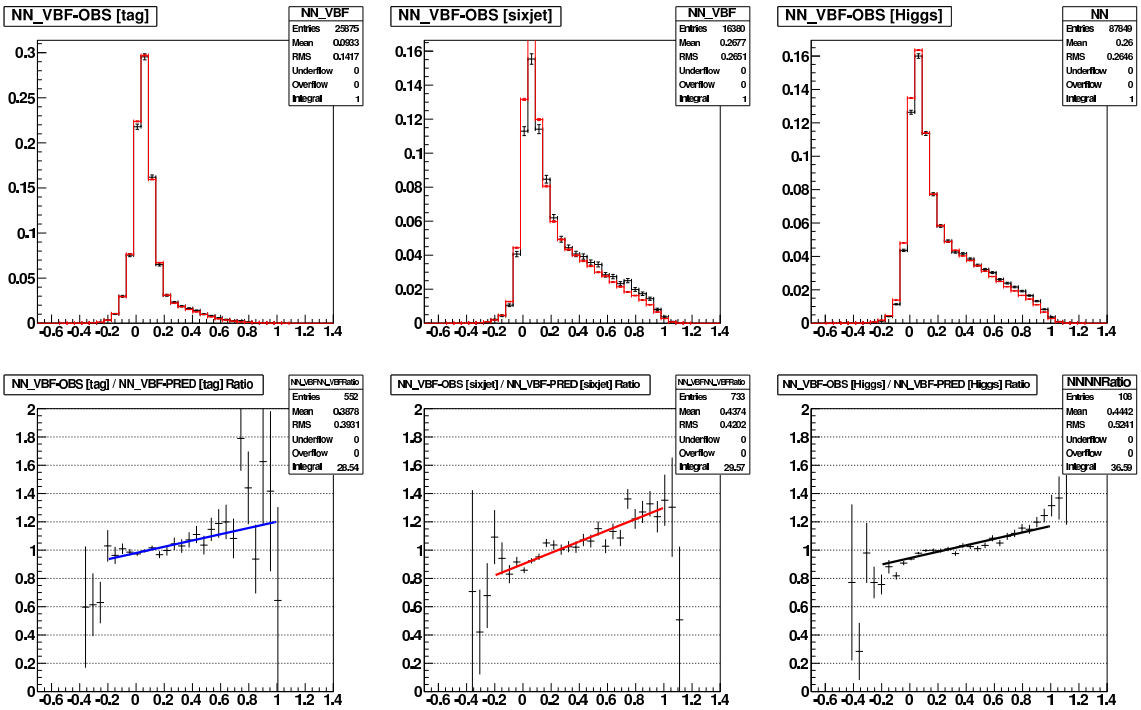

(a) NN_VBF in Tag Region. (b) NN_VBF in NJet6 Region. (c) NN_VBF in Higgs Region.

Figure 75: VBF Neural Network Output for MH100-SS in a) Tag, b) NJet6 and c) Higgs Region show the same mis-modelling.

- $70GeV < M_{bb} < 75GeV, M_{qq} > 45GeV$
- $75GeV < M_{bb} < 175GeV, 45GeV < M_{qq} < 50GeV$
- $175GeV < M_{bb} < 200GeV, M_{qq} > 45GeV$

The figures 76, 80 and 84 show, for the mass point 100, 120 and 140 in SS category, the distribution of VBF Neural Network Output in Tag, NJet6 and CTRL Region before the application of correction Function; the figures 77, 81 and 85 show the distribution of VBF and SuperDiscriminat Neural Network Output after the application of Correction Function. For MH100-SS and MH140-SS we use the Tag Correction Function to correct the Neural Network Output and the NJet6 one for the systematics uncertainties. For MH120-SS the NJet6 Correction function does give a better KS-value and χ^2/NDF value. However the difference between between using the NJet6 and TAG correction function is minor. So it was decided to apply the TAG correction function for MH120-SS too and be consistent with the other samples.

The figures 78, 82 and 86 show, for the mass point 100, 120 and 140 in SJ category, the distribution of VBF Neural Network Output in Tag, NJet6 and CTRL Region before the application of correction Function; the figures 79, 83 and 87 show the distribution of VBF and SuperDiscriminat Neural Network Output after the application of Correction Function. For these samples we use the Tag Correction Function to correct the Neural Network Output and the NJet6 one to evaluate the systematics uncertainties.

The table 9 show a summary for each sample what correction is applyed and which one is used to evaluate the systematic uncertainty.

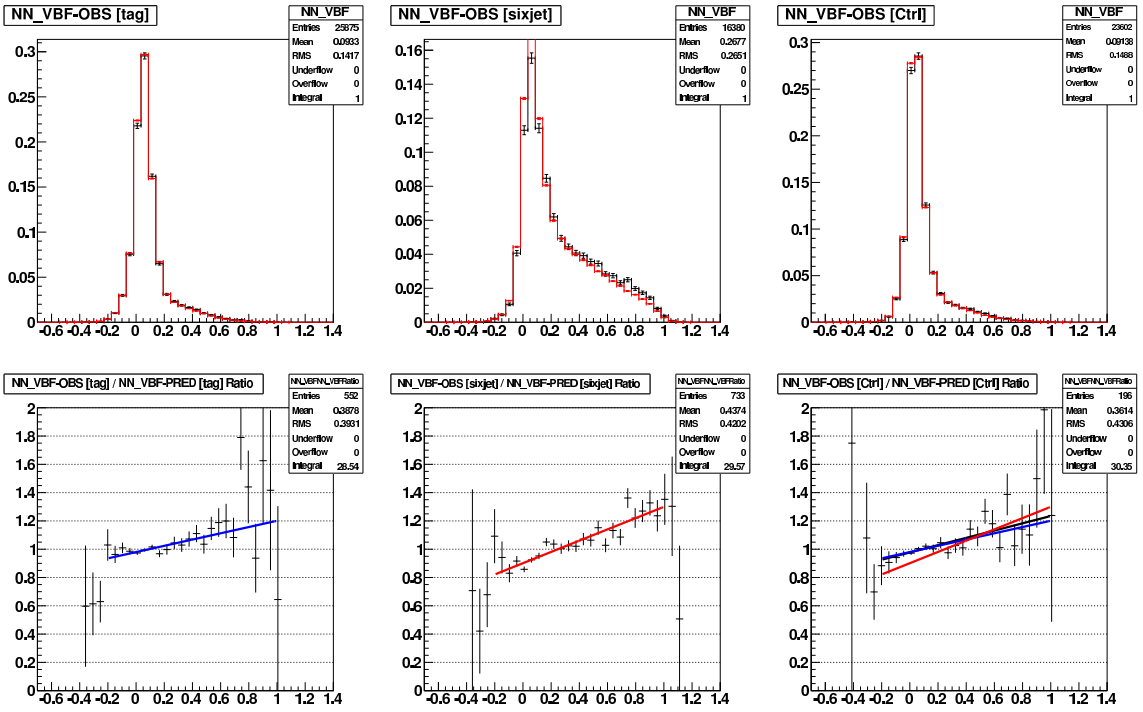

(a) NN_VBF Correction function evaluated in Tag Region.

(b) NN_VBF Correction function evaluated in NJet6 Region.

(c) NN_VBF in CTRL Region with overlap of Correction Function obtained in Tag and NJet6 Region.

Figure 76: Neural Network Correction Function for MH100-SS evaluated in a) Tag, b) NJet6 and c) overlap of these correction in CTRL Region where the red line is the fit obtained in NJet6 Region, blue line is the fit in Tag Region and the black line is the fit in CTRL Region.

Sample	Correction	Systematics
100SS	Tag	NJet6
100SJ	Tag	NJet6
120SS	Tag	NJet6
120SJ	Tag	NJet6
140SS	Tag	NJet6
140SJ	Tag	NJet6

Table 9: Summary of NN Correction Function.

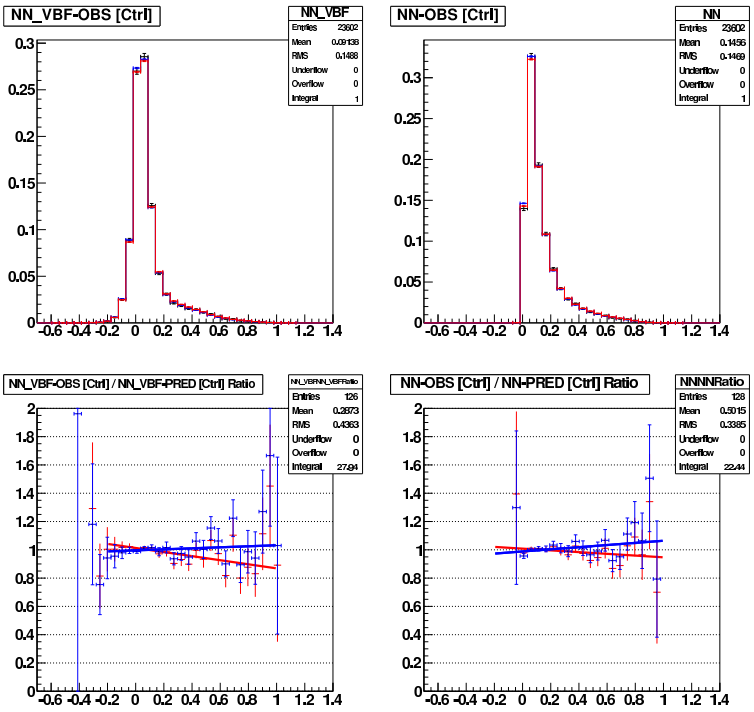

(a) VBF Neural Network in CTRL Region.

(b) SuperDiscriminant Neural Network in CTRL Region.

Figure 77: Distribution of Neural Network Output for MH100-SS in CTRL Region after the application of Correction Function. a) VBF and b) SuperDiscriminant Neural Network Output. The red histograms are the NN Output after the application of the Correction Function evaluated in NJet6 Region. The blue histograms are the NN Output after the application of the Correction Function evaluated in Tag Region. The black histograms are the NN Output for Data.

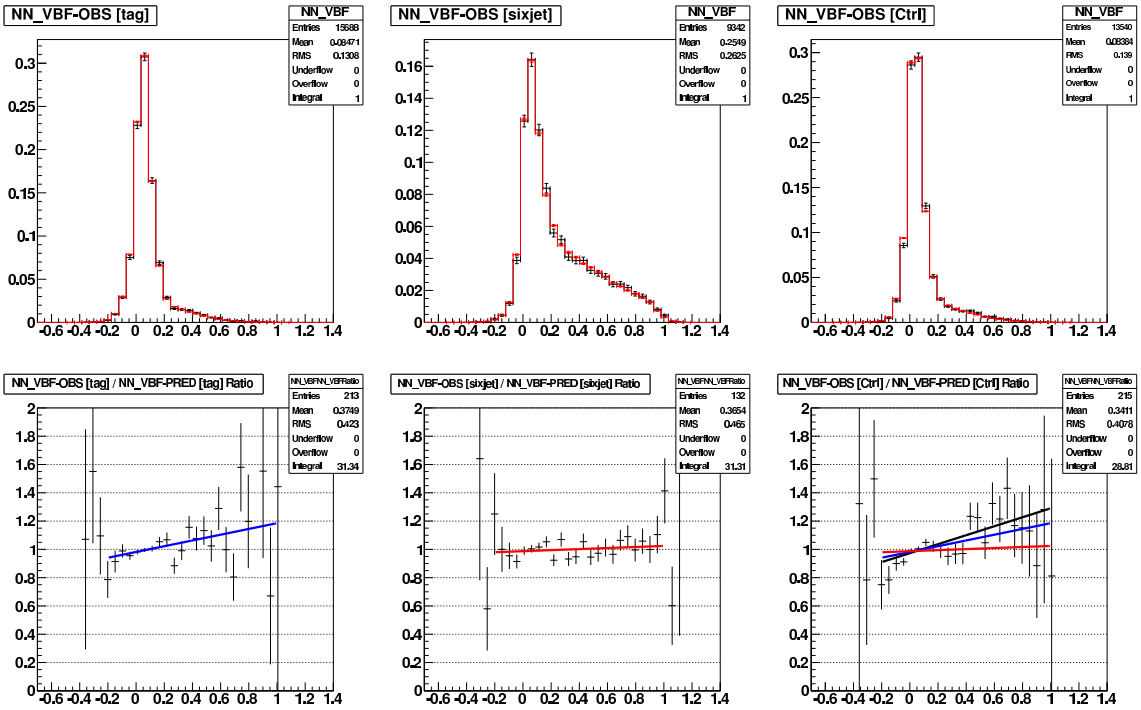

(a) NN_VBF Correction function evaluated in Tag Region.

(b) NN_VBF Correction function evaluated in NJet6 Region.

(c) NN_VBF in CTRL Region with overlap of Correction Function obtained in Tag and NJet6 Region.

Figure 78: Neural Network Correction Function for MH100-SJ evaluated in a) Tag, b) NJet6 and c) overlap of these correction in CTRL Region where the red line is the fit obtained in NJet6 Region, blue line is the fit in Tag Region and the black line is the fit in CTRL Region.

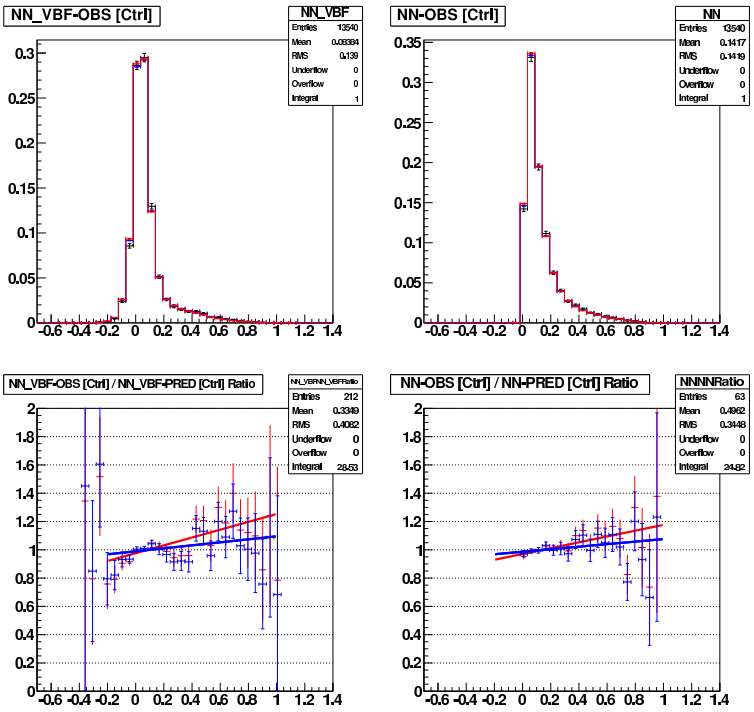

(a) VBF Neural Network in CTRL Region.

(b) SuperDiscriminant Neural Network in CTRL Region.

Figure 79: Distribution of Neural Network Output for MH100-SJ in CTRL Region after the application of Correction Function. a) VBF and b) SuperDiscriminant Neural Network Output. The red histograms are the NN Output after the application of the Correction Function evaluated in NJet6 Region. The blue histograms are the NN Output after the application of the Correction Function evaluated in Tag Region. The black histograms are the NN Output for Data.

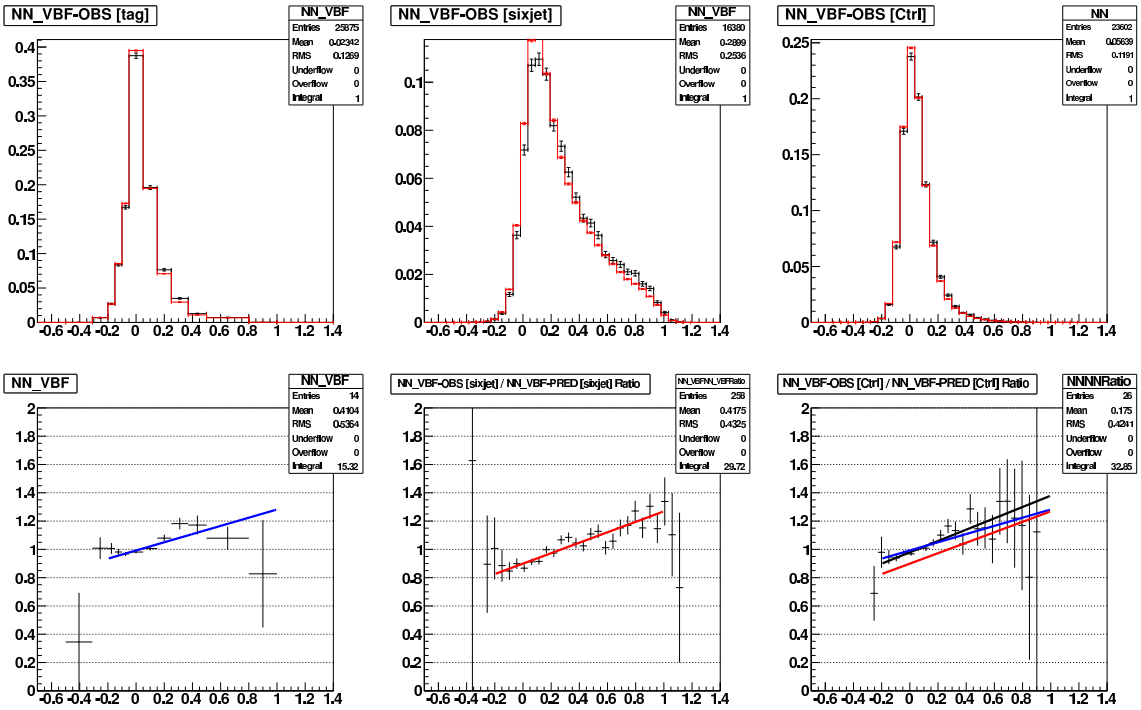

(a) NN_VBF Correction function evaluated in Tag Region.

(b) NN_VBF Correction function evaluated in NJet6 Region.

(c) NN_VBF in CTRL Region with overlap of Correction Function obtained in Tag and NJet6 Region.

Figure 80: Neural Network Correction Function for MH120-SS evaluated in a) Tag, b) NJet6 and c) overlap of these correction in CTRL Region where the red line is the fit obtained in NJet6 Region, blue line is the fit in Tag Region and the black line is the fit in CTRL Region.

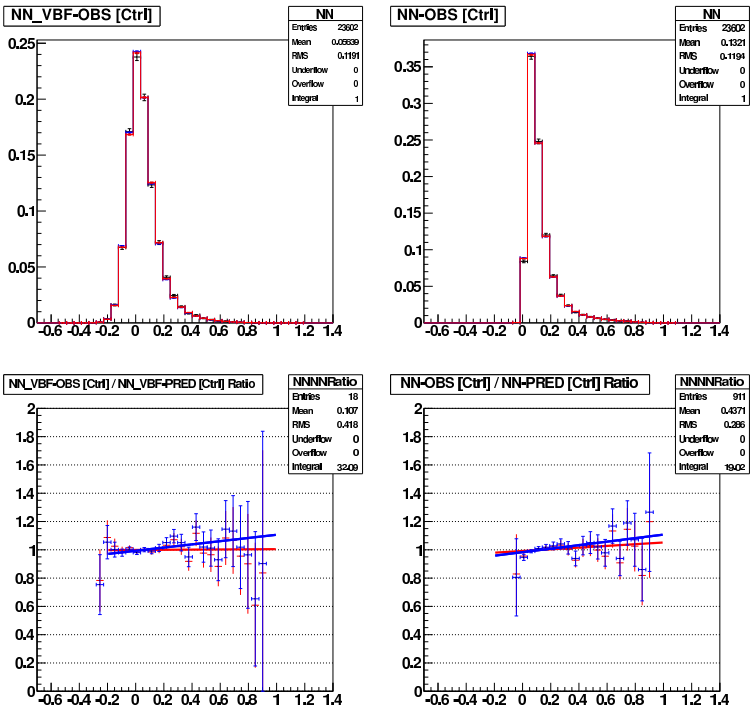

(a) VBF Neural Network in CTRL Region.

(b) SuperDiscriminant Neural Network in CTRL Region.

Figure 81: Distribution of Neural Network Output for MH120-SS in CTRL Region after the application of Correction Function. a) VBF and b) SuperDiscriminant Neural Network Output. The red histograms are the NN Output after the application of the Correction Function evaluated in NJet6 Region. The blue histograms are the NN Output after the application of the Correction Function evaluated in Tag Region. The black histograms are the NN Output for Data.

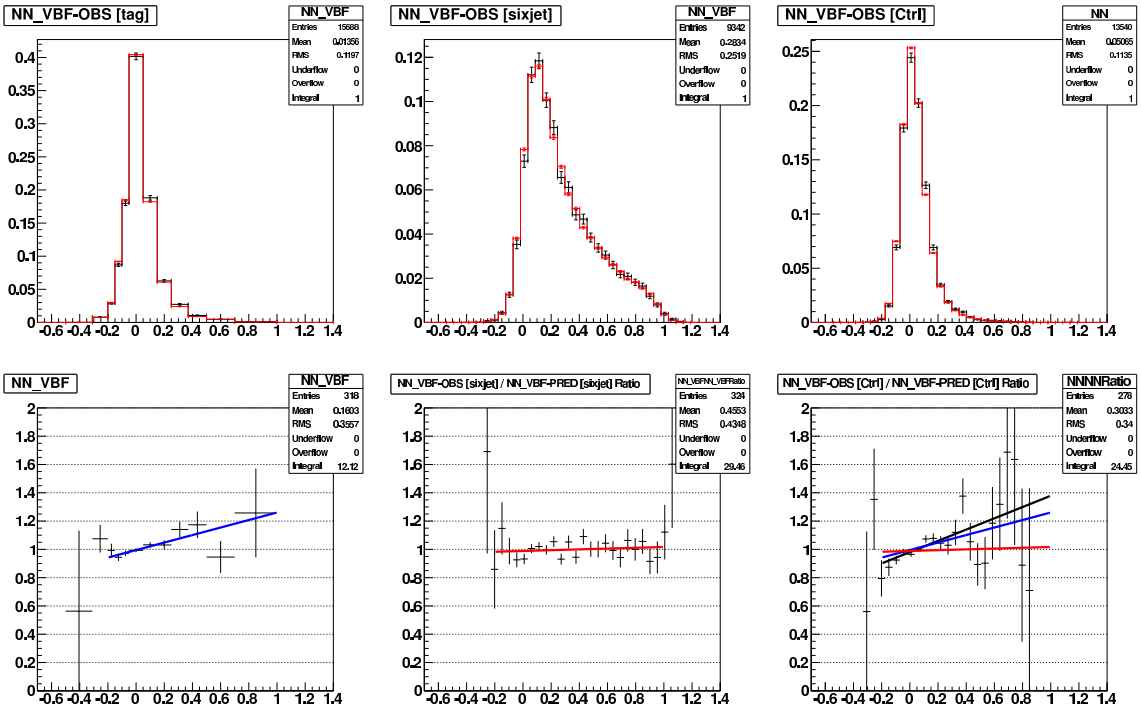

(a) NN_VBF Correction function evaluated in Tag Region.

(b) NN_VBF Correction function evaluated in NJet6 Region.

(c) NN_VBF in CTRL Region with overlap of Correction Function obtained in Tag and NJet6 Region.

Figure 82: Neural Network Correction Function for MH120-SJ evaluated in a) Tag, b) NJet6 and c) overlap of these correction in CTRL Region where the red line is the fit obtained in NJet6 Region, blue line is the fit in Tag Region and the black line is the fit in CTRL Region.

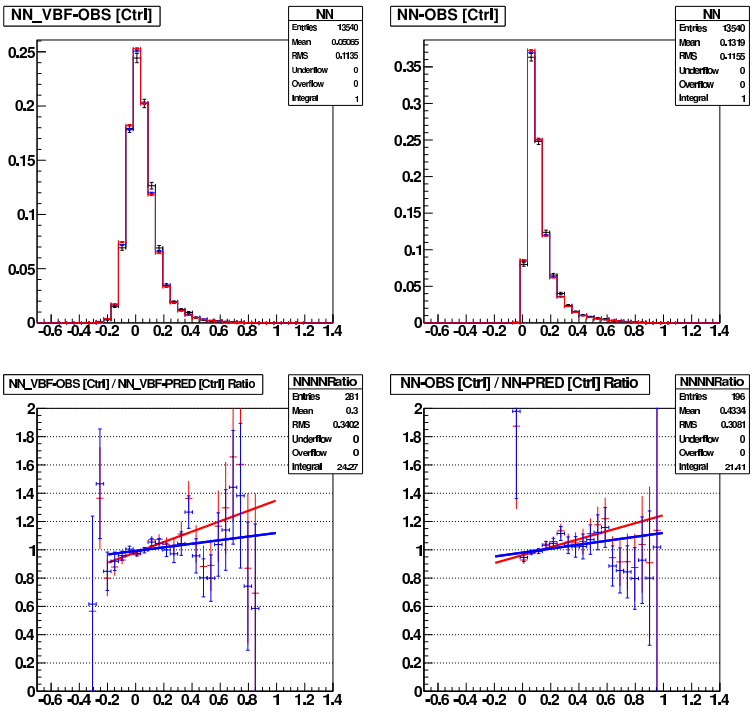

(a) VBF Neural Network in CTRL Region.

(b) SuperDiscriminant Neural Network in CTRL Region.

Figure 83: Distribution of Neural Network Output for MH120-SJ in CTRL Region after the application of Correction Function. a) VBF and b) SuperDiscriminant Neural Network Output. The red histograms are the NN Output after the application of the Correction Function evaluated in NJet6 Region. The blue histograms are the NN Output after the application of the Correction Function evaluated in Tag Region. The black histgrams are the NN Output for Data.

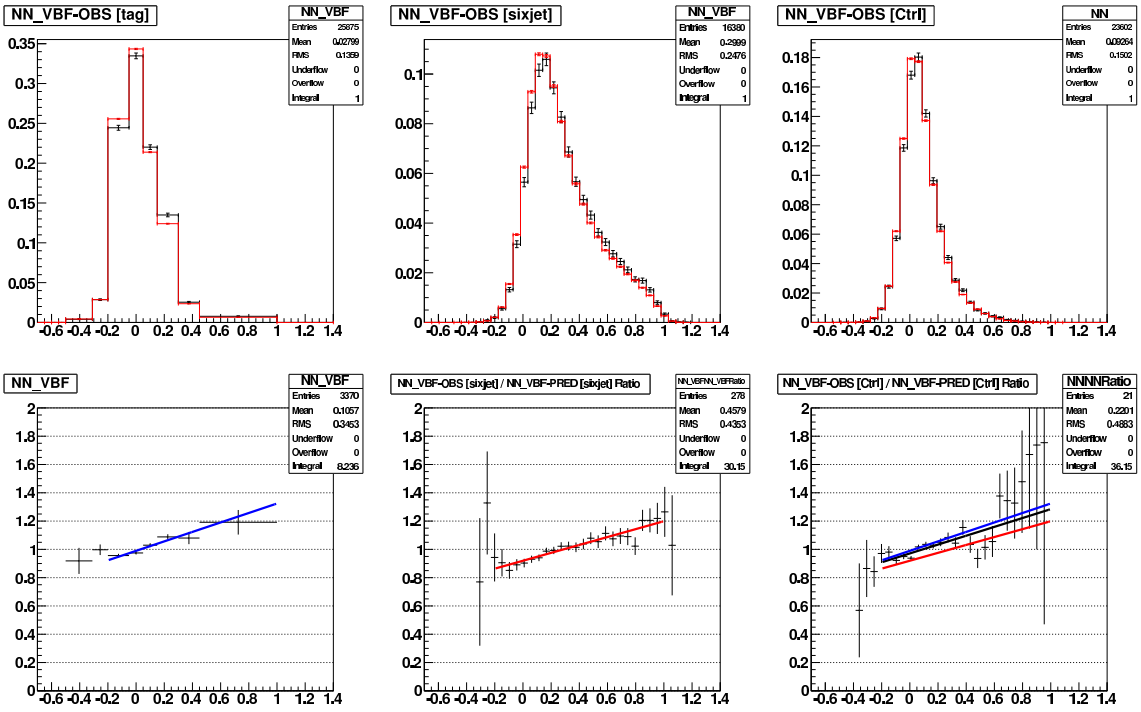

(a) NN_VBF Correction function evaluated in Tag Region.

(b) NN_VBF Correction function evaluated in NJet6 Region.

(c) NN_VBF in CTRL Region with overlap of Correction Function obtained in Tag and NJet6 Region.

Figure 84: Neural Network Correction Function for MH140-SS evaluated in a) Tag, b) NJet6 and c) overlap of these correction in CTRL Region where the red line is the fit obtained in NJet6 Region, blue line is the fit in Tag Region and the black line is the fit in CTRL Region.

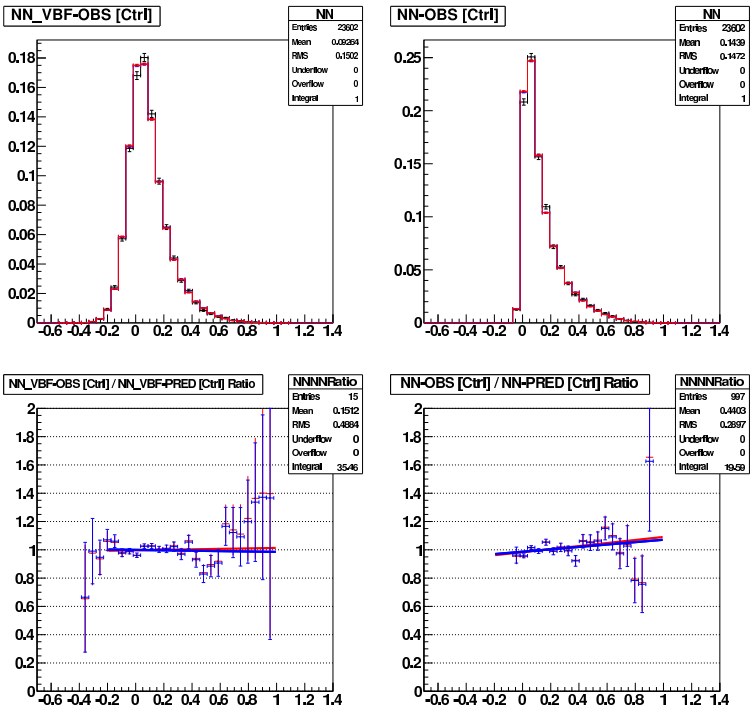

(a) VBF Neural Network in CTRL Region.

(b) SuperDiscriminant Neural Network in CTRL Region.

Figure 85: Distribution of Neural Network Output for MH140-SS in CTRL Region after the application of Correction Function. a) VBF and b) SuperDiscriminant Neural Network Output. The red histograms are the NN Output after the application of the Correction Function evaluated in NJet6 Region. The blue histograms are the NN Output after the application of the Correction Function evaluated in Tag Region. The black histograms are the NN Output for Data.

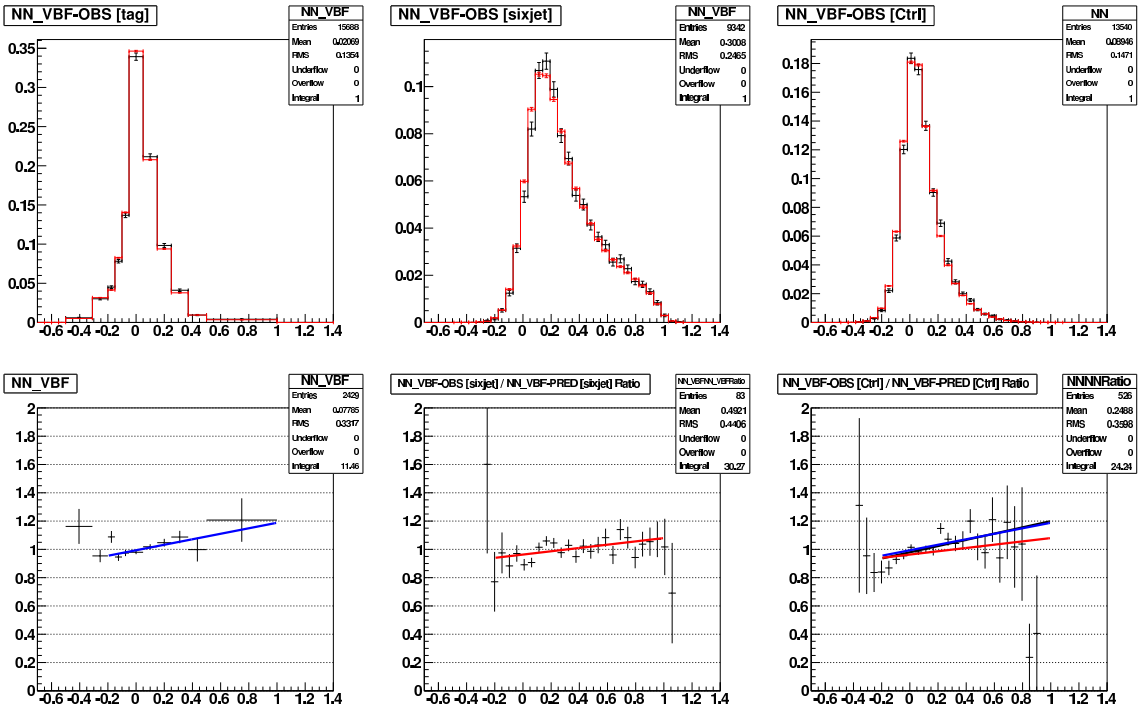

(a) NN_VBF Correction function evaluated in Tag Region.

(b) NN_VBF Correction function evaluated in NJet6 Region.

(c) NN_VBF in CTRL Region with overlap of Correction Function obtained in Tag and NJet6 Region.

Figure 86: Neural Network Correction Function for MH140-SJ evaluated in a) Tag, b) NJet6 and c) overlap of these correction in CTRL Region where the red line is the fit obtained in NJet6 Region, blue line is the fit in Tag Region and the black line is the fit in CTRL Region.

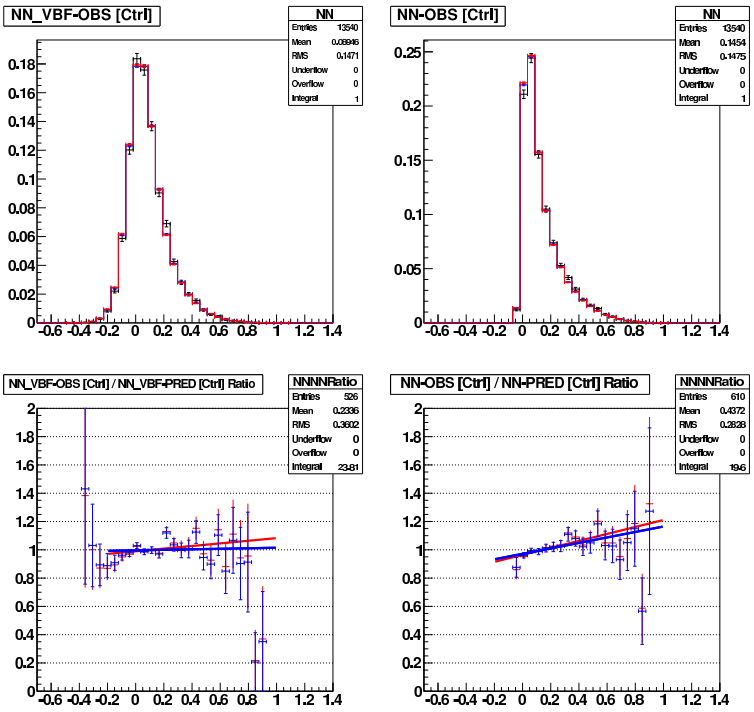

(a) VBF Neural Network in CTRL Region.

(b) SuperDiscriminant Neural Network in CTRL Region.

Figure 87: Distribution of Neural Network Output for MH140-SJ in CTRL Region after the application of Correction Function. a) VBF and b) SuperDiscriminant Neural Network Output. The red histograms are the NN Output after the application of the Correction Function evaluated in NJet6 Region. The blue histograms are the NN Output after the application of the Correction Function evaluated in Tag Region. The black histograms are the NN Output for Data.

9 Systematics Uncertainty

9.1 TRF Systematics

For the TRF predicited backgrounds, three sources of systematic error were considered:

- TRF Interpolation Uncertainty
- m_{qq} tuning uncertainty
- VBF-NN tuning uncertainty

All three systematics were taken as shape systematics. Normalisation errors were not considered as the background prediction will be floated to best fit the data.

9.1.1 TRF Interpolation Uncertainty

The nominal background predicition used the TRF derived from the TAG regions (TAG-TRF) which is interpolated into the signal region. The systematic error for this interpolation is taken from the background prediction using the CTRL-TRF. The difference of these two background shapes is used as the interpolation shape systematic. Figure 88 shows the Neural Net shapes using the nominal TRF(TAG) and TRF(CTRL).

9.1.2 m_{qq} Tuning Uncertainties

In section 5.1 it was shown that the predicted mass m_{qq} are tuned using correction functions measured in the TAG region. To estimate the uncertainties due to these tuning corrections, we measured another set of correction functions in the CTRL region. The difference in the NN output due to the different sets of correction functions are then taken as the effect of the uncertainties from these tuning corrections (Fig. 89).

9.1.3 VBF-NN Tuning Uncertainties

Section 8 discussed the requirement for additional tuning of the VBF-NN output. A function measured in the TAG region is used to correct the output of the VBF-NN. An alternative correction function is measured in the SIXJET region and is used to give an alternative background prediction. The difference of the two background shapes defines the VBF-NN correction function systematic uncertainty (Fig. 90).

9.1.4 Summary of all TRF systematic uncertainties

Figure 91 summarizes shows the effect of each TRF systematic and the total TRF systematic. Each plot shows the error in number of events for each NN bin and each plot has the data-total background superimposed. For most plots, the scatter of the data-total background is within the bounds defined by the total TRF systematic uncertainty.

9.2 Signal Systematics

9.2.1 Jet Energy Scale

The Jet Energy Scale affects the Jet E_t related quantities. The training variables which are affected most are the m_{bb} and m_{qq} . The effect upon the Neural Net distribution is shown in figure 92. Although the Jet Energy Scale systematics affects the m_{bb} and m_{qq} distribution, the Neural Net shape for the Higgs signal is less affected. However $t\bar{t}$ NN output is sensitive to the changes in the JES. The JES uncertainty does affect the acceptance on account of the SumEt>220.0 GeV event selection cut and we apply a $\pm 9\%$ rate systematic error in addition to the shape errors.

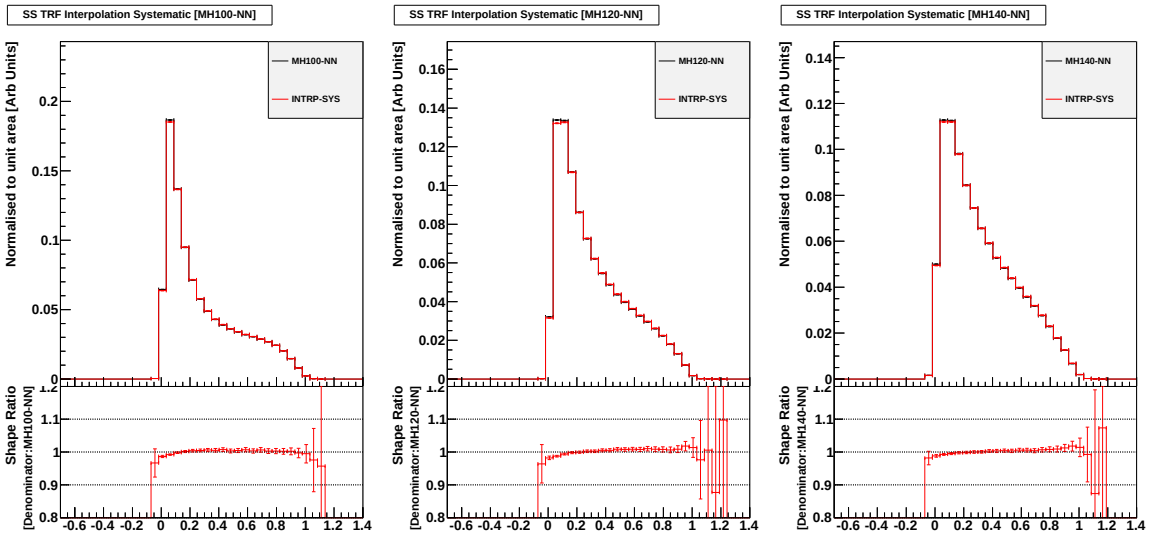

(a) SS MH100-NN (b) SS MH120-NN (c) SS MH140-NN

(d) SJ MH100-NN (e) SJ MH120-NN (f) SJ MH140-NN

Figure 88: TRF Interpolation Uncertainty: The nominal TRF QCD prediction uses TRF measured from the TAG region (black). Another TRF is measured in the CTRL region (red) and the difference of the two shapes defines the TRF interpolation systematic.

The Higgs group are now recommending separate JES for quarks and gluons. For this Higgs search, 98% of the background is multijet QCD which is modeled from data. Thus no JES is required However the signal could potentially have gluon jets in the jet selected for the analysis. Figure 93 show the the Higgs-NN output using the nominal JES (black) and gluon-JES applied to gluons (red). We find no change in the shape or acceptance. So we will not apply any specific gluon-JES for this analysis.

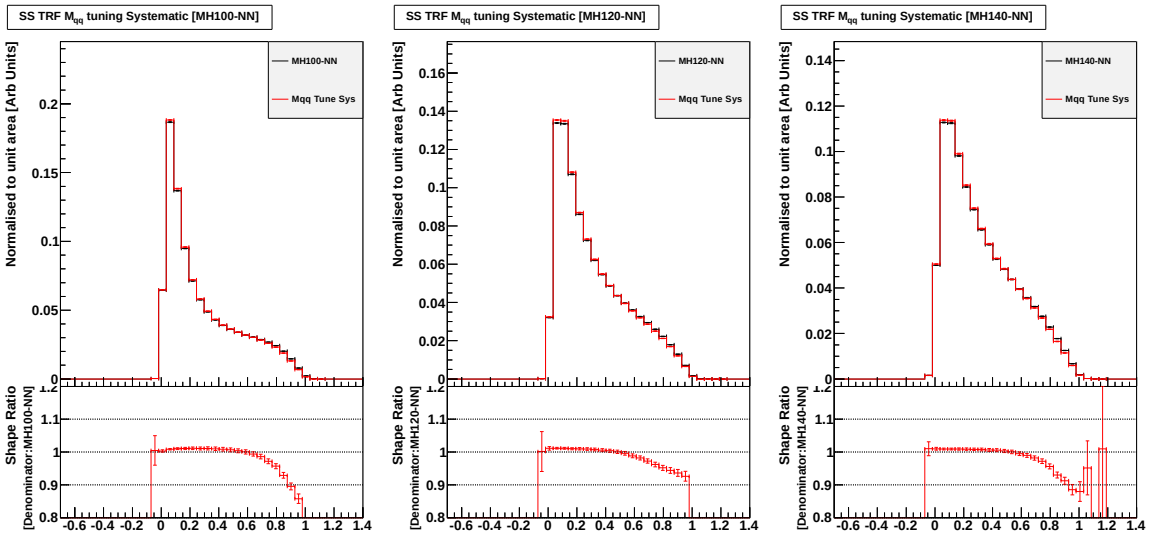

(a) SS MH100-NN (b) SS MH120-NN (c) SS MH140-NN

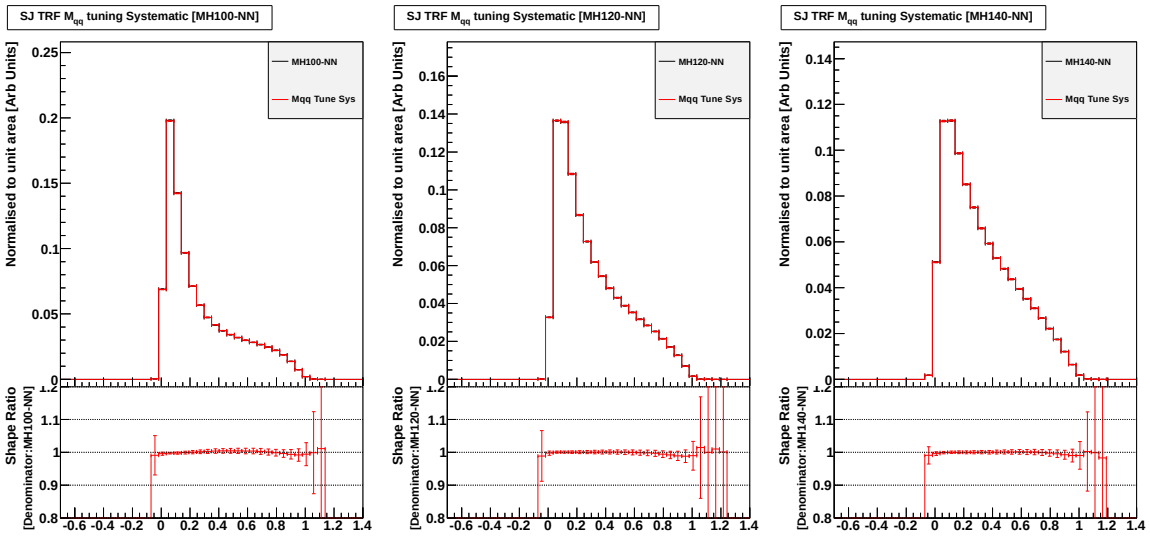

(d) SJ MH100-NN (e) SJ MH120-NN (f) SJ MH140-NN

Figure 89: m_{qq} tuning uncertainty: The nominal TRF (QCD) prediction uses a tuning function for m_{qq} measured in the TAG region (black). A measure of the systematic uncertainty is to use an alternative m_{qq} correction function measured in the CTRL region (red). The difference of the two background shapes defines the systematic uncertainty for the m_{qq} tuning uncertainty.

9.2.2 ISR/FSR Systematics

The ISR/FSR systematics for the Higgs signal was measured using the prescription defined in May 27 2005 Joint Physics Meeting [13]. The effect of the systematic upon the neural network shape for the Higgs signal is shown in Figure 94. This is included as a shape systematic in the limit calculation. The VBF sample only shows shape changes from reduction of ISR/FSR as no MC sample was available for increased ISR/FSR. For the limit calculation we assume the shape change for VBF is symmetric. In addition to the shape systematic, the change in ISR/FSR affects the acceptance. There is a $\pm 3\%$

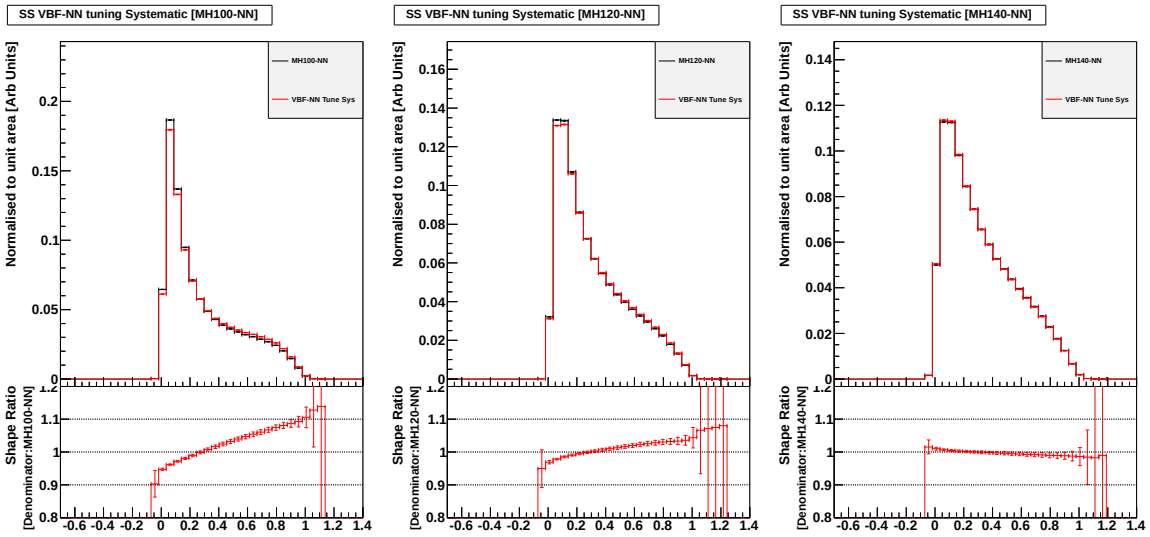

(a) SS MH100-NN (b) SS MH120-NN (c) SS MH140-NN

(d) SJ MH100-NN (e) SJ MH120-NN (f) SJ MH140-NN

Figure 90: VBF-NN correction function uncertainty: The nominal TRF (QCD) prediction uses a VBF-NN correction function, measured in the TAG region, to correct the VBF-NN output (black). Another VBF-NN correction function is measured in the SIXJET region to give an alternative background prediction (red). The difference of the two TRF shapes defines the VBF-NN correction function uncertainty.

rate systematic. for VH and VBF Higgs signal.

9.2.3 Jet width uncertainty

The jet width uncertainty affects the shape of the NN output and evaluated in a similar fashion as the JES uncertainty. The calorimeter(tracker) jet width are adjusted by $\pm 0.004(0.006)$ ($\pm 1\sigma$). We assume the calorimeter and tracker jet width uncertainty are uncorrelated and are evaluated

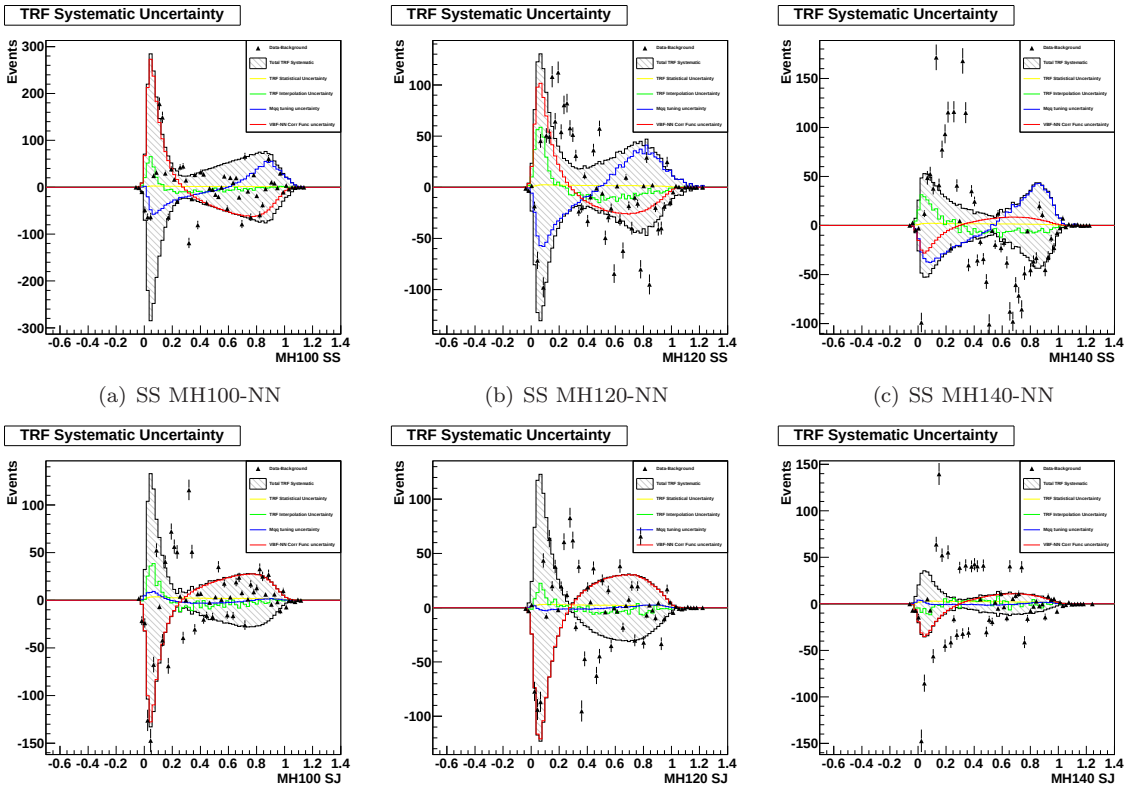

(a) SS MH100-NN (b) SS MH120-NN (c) SS MH140-NN

(d) SJ MH100-NN (e) SJ MH120-NN (f) SJ MH140-NN

Figure 91: Summary of all TRF systematic uncertainties: Each plot shows the bin-by-bin uncertainty of each TRF systematic component, the total TRF systematic and the data-total background. For most NN, the scatter of the data-total background is contained within the bounds defined by the total TRF systematic uncertainty.

separately. Figure 95 and 96 shows the change in NN shape from a $\pm 1\sigma$ change of jet width. The NN is sensitive to changes to the jet width with the calorimeter measured jet width being more sensitive.

9.3 Summary of all Systematic

Table 10 summarises all the rate uncertainties & shape systematics which are applied to calculate the limit.

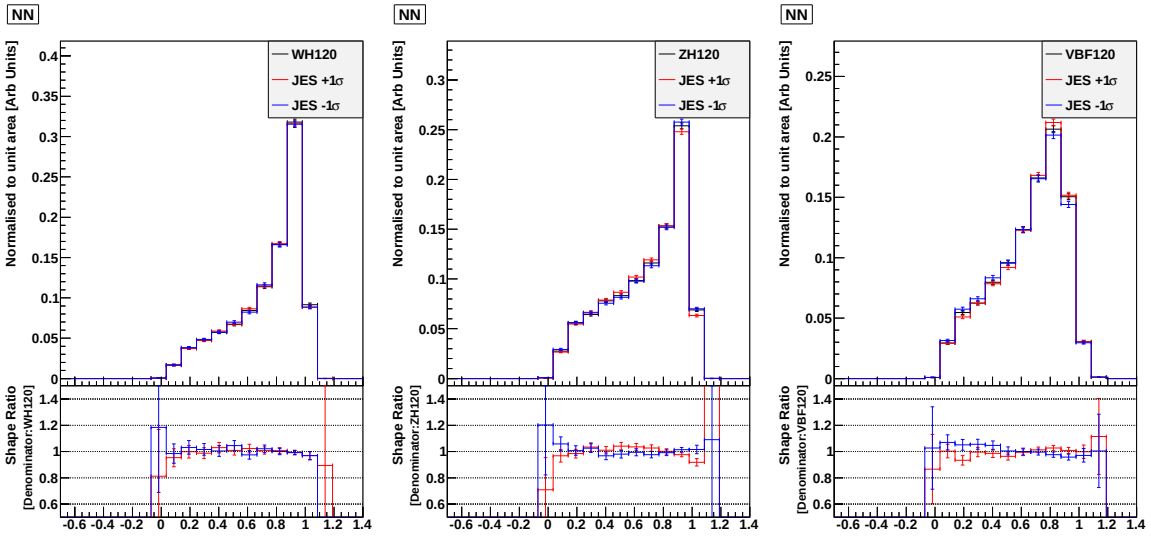

(a) WH(m_H=120 GeV/c^2) JES systematic (b) ZH(m_H=120 GeV/c^2) JES systematic (c) VBF(m_H=120 GeV/c^2) JES systematic

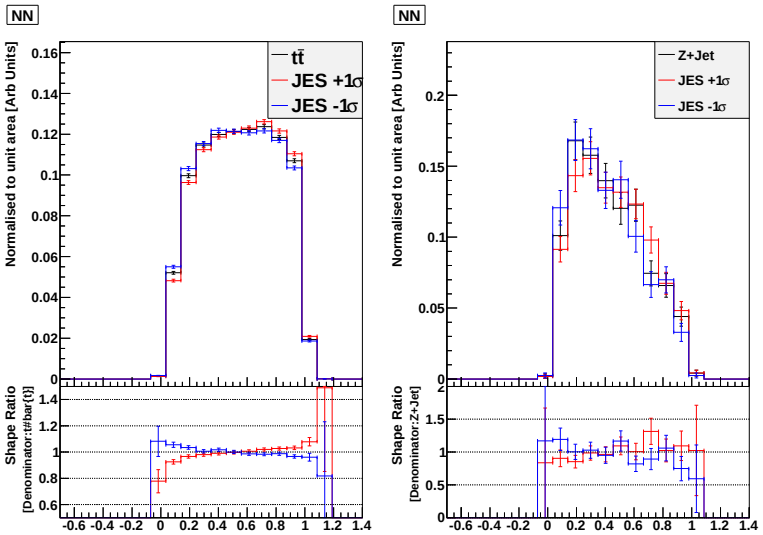

(d) $t\bar{t}$JES systematic (e) Z+Jet JES systematic

Figure 92: Jet Energy Scale Systematic: The variation of the NN output for $\pm 1\sigma$ variation of the Jet Energy Scale. The black histograms use the nominal JES and the red(blue) histograms use JES shifted by +(-)1σ. The histograms are normalized to unit area to show the variation in shape. The ratio plots are show the ratio of shifted JES / Nominal JES.

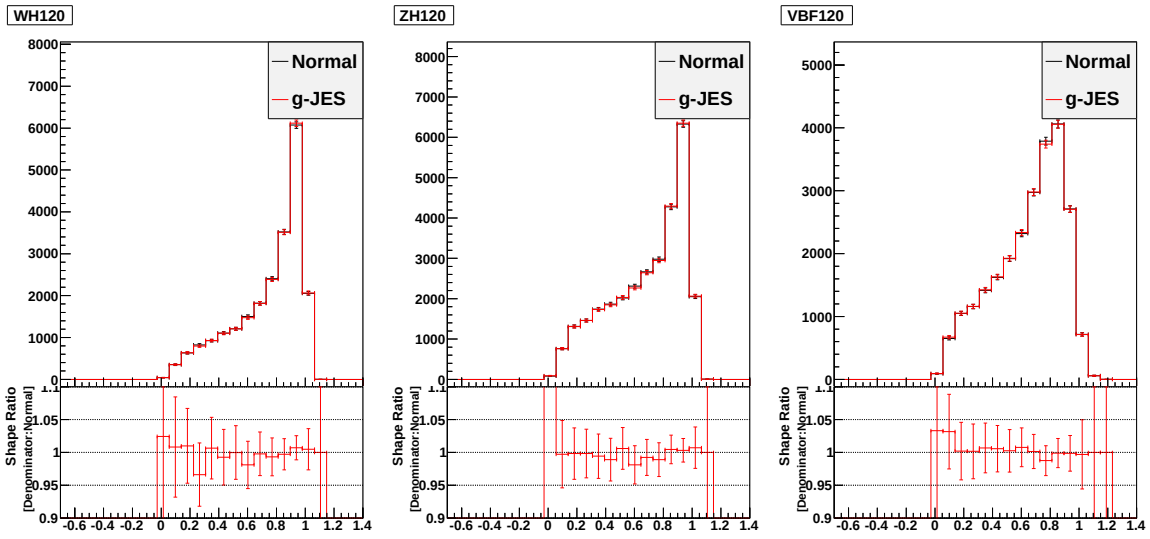

(a) WH(m_H=120 GeV/c^2) (b) ZH(m_H=120 GeV/c^2) (c) VBF(m_H=120 GeV/c^2)

Figure 93: Effect of Gluon-JES: The Higgs-NN output for WH, ZH and VBF are shown using the default CDF JES (black) and a gluon specific JES (Red). We see no change after applying the gluon-JES.

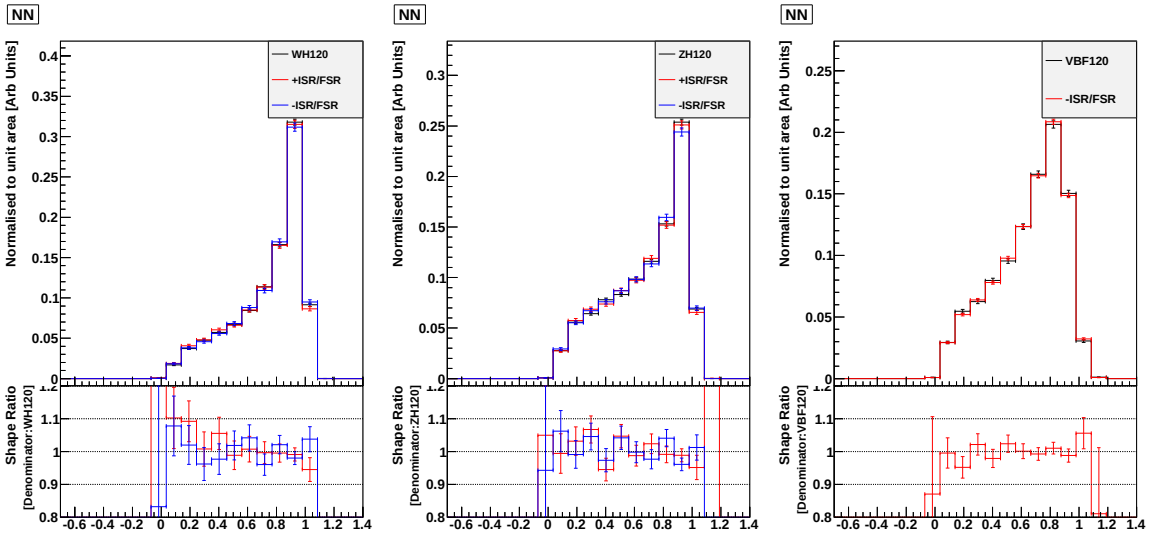

(a) WH(m_H=120 GeV/c^2) SS More/Less ISR/FSR (b) ZH(m_H=120 GeV/c^2) SS More/Less ISR/FSR (c) VBF(m_H=120 GeV/c^2) SS Less ISR/FSR

Figure 94: Variation of ISR/FSR: The variation of the SS SD-NN from $\pm 1\sigma$ changes in the ISR/FSR. The black histogram is the nominal ISR/FSR scale and the red(blue) are changes in +(-)1σ changes of ISR/FSR. The VBF plot only has change in reduction of ISR/FSR as no MC sample for increased ISR/FSR is available.

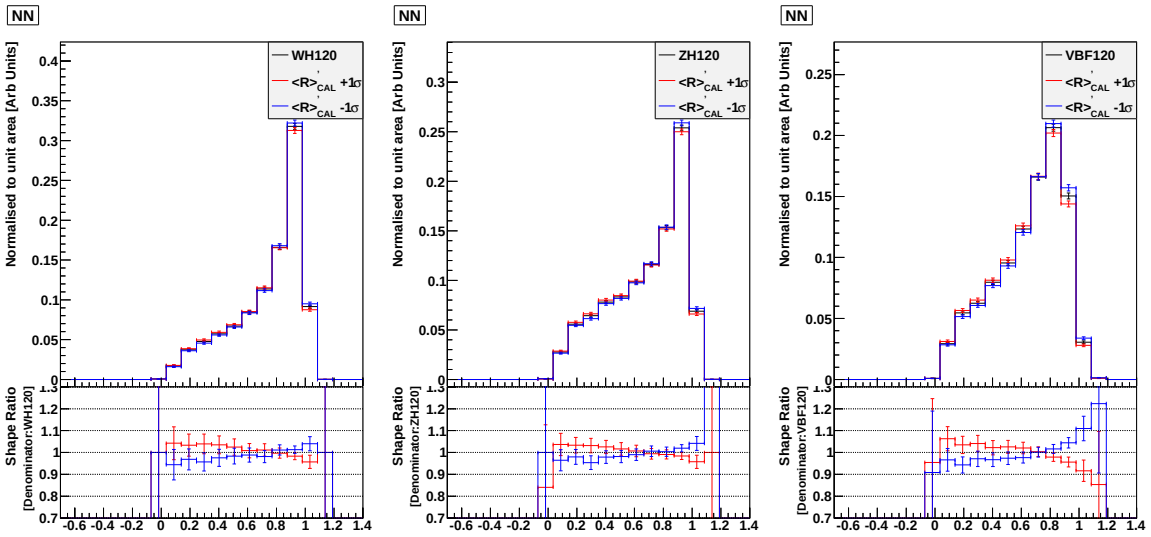

(a) WH(m_H=120 GeV/c^2) SS Calorimeter Jet Width Uncertainty

(b) ZH(m_H=120 GeV/c^2) SS Calorimeter Jet Width Uncertainty

(c) VBF(m_H=120 GeV/c^2) SS Calorimeter Jet Width Uncertainty

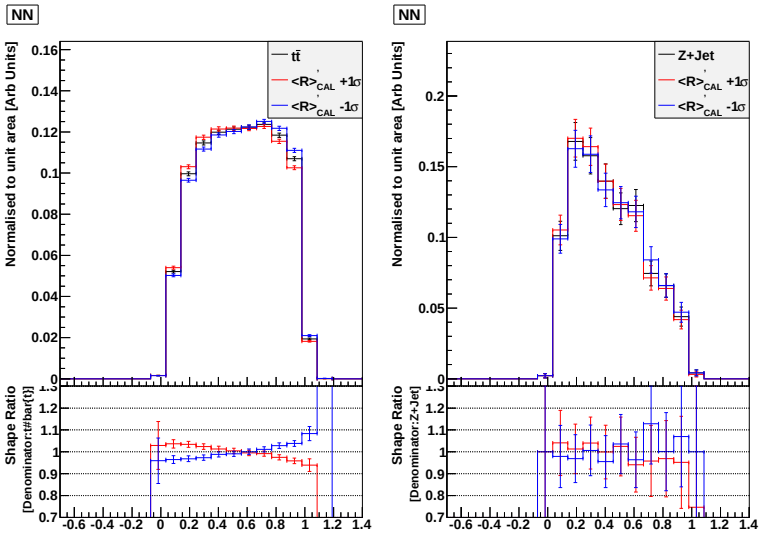

(d) $t\bar{t}$ SS Calorimeter Jet Width Uncertainty

(e) Z+Jet Calorimeter Jet Width Uncertainty

Figure 95: Jet width uncertainty: Changes in the SS SD-NN shape from changes in the calorimeter jet width by $\pm 1\sigma$. The black histograms are the nominal jet width and the red(blue) are changes by +(-)1σ. The histograms are normalized to unit area to show variation in shape. The ratio plots show shifted Jet Width / nominal jet width.

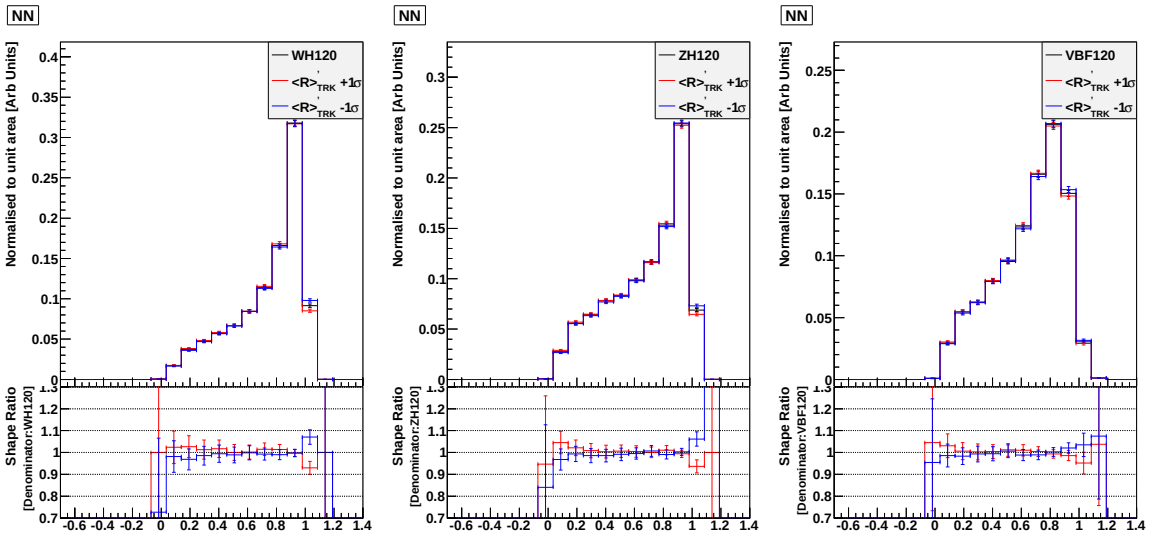

(a) WH(m_H=120 GeV/c^2) SS Tracker Jet Width Uncertainty

(b) ZH(m_H=120 GeV/c^2) SS Tracker Jet Width Uncertainty

(c) VBF(m_H=120 GeV/c^2) SS Tracker Jet Width Uncertainty

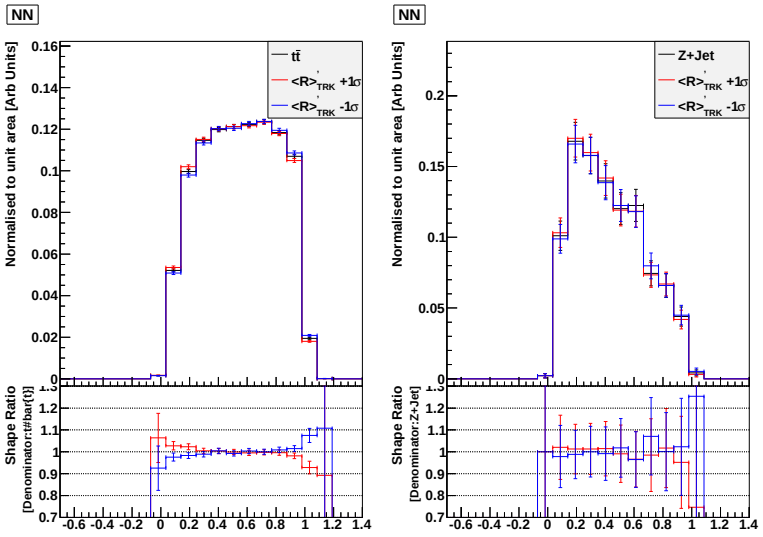

(d) $t\bar{t}$ SS Tracker Jet Width Uncertainty

(e) Z+Jet Tracker Jet Width Uncertainty

Figure 96: Jet width uncertainty: Changes in the SS SD-NN shape from changes in the tracker jet width by $\pm 1\sigma$. The black histograms are the nominal jet width and the red(blue) are changes by $+(-)1\sigma$. The histograms are normalized to unit area to show variation in shape. The ratio plots show shifted Jet Width / nominal jet width.

Table 10: Summary of all Systematic Uncertainties used to calculate the limit

TRF (QCD) Uncertainties	
TRF Interpolation	Shape
TRF m_{qq} Tuning	Shape
TRF VBF-NN tuning	Shape
Higgs and Non-QCD Uncertainties	
Luminosity	± 6% Rate
Trigger	± 3.55% Rate
SecVtx+SecVtx	± 7.1% Rate
SecVtx+JetProb	± 6.4% Rate
Jet Energy Correction	± 9% Rate
	Shape
Jet Width	Shape
Higgs and Non-QCD cross-section uncertainties	
$t\bar{t}$& single-top	± 7% Rate
Diboson (WW/WZ/ZZ)	± 6% Rate
W+HF & Z+Jets	± 50% Rate
WH/ZH	± 5% Rate
VBF	± 10% Rate
Higgs Uncertainties	
PDF	± 2% Rate
ISR/FSR	± 3%
	Shape

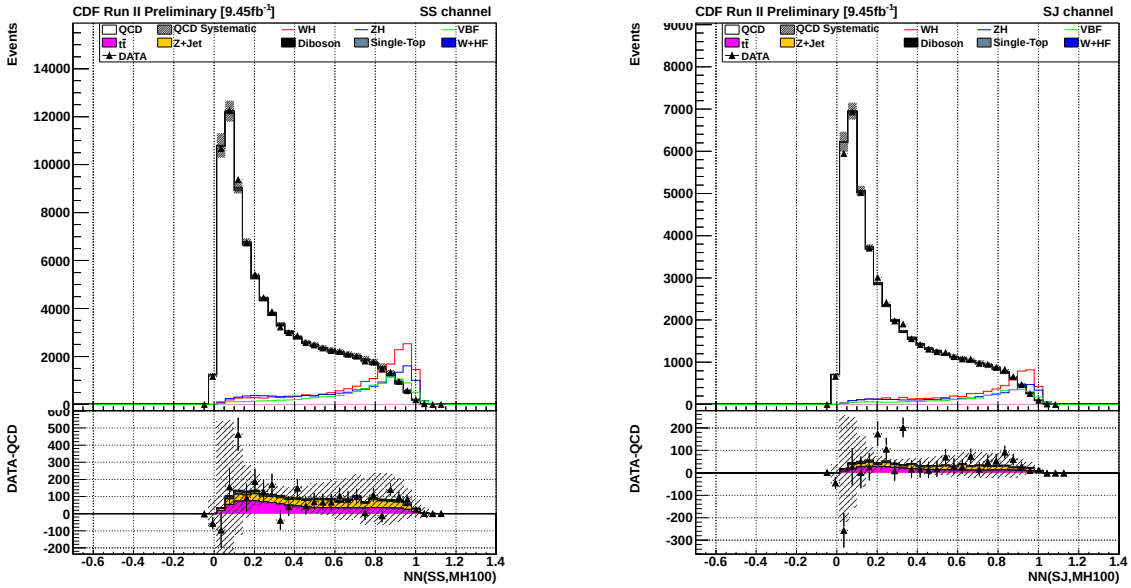

(a) MH100-SS (b) MH100-SJ

Figure 97: Higgs-NN distribution for m_H=100 GeV/c^2. The left plot are from the SS b-tag category and the right plot is from the SJ b-tag category. All backgrounds are stacked and the superimposed Higgs signal is scaled by x1000. As the QCD background is large, plots of the DATA-QCD are plotted with stacked plot of non-QCD background and QCD systematic.

10 Unblinded Signal Region

Figures 97- 107 show the Higgs-NN output distributions. The backgrounds are stacked and the Higgs signal is scaled by x1000. As the QCD multijet background is large, plots of DATA-QCD residual plots are shown with the the non-QCD backgrounds stacked. The plots show the background prediction is in good agreement with the data. Figures 108, 109 and 110 show ratio plots of the DATA/Total Background. These histograms are made with 50 bins rather than 100 bins to reduce the statistical scatter. The ratio plots confirm the background is in good agreement with the DATA.

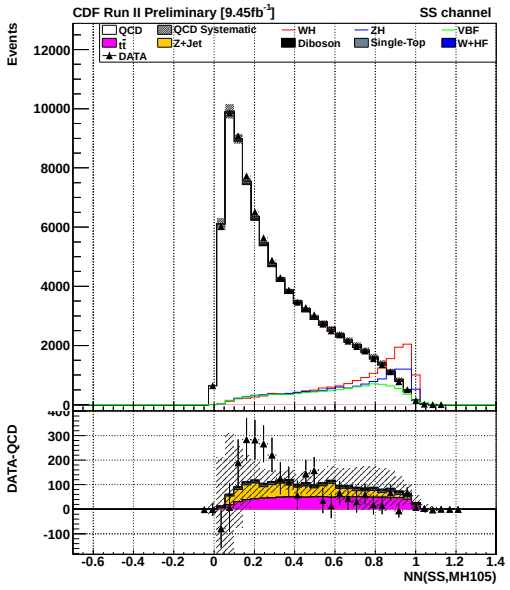

(a) MH105-SS

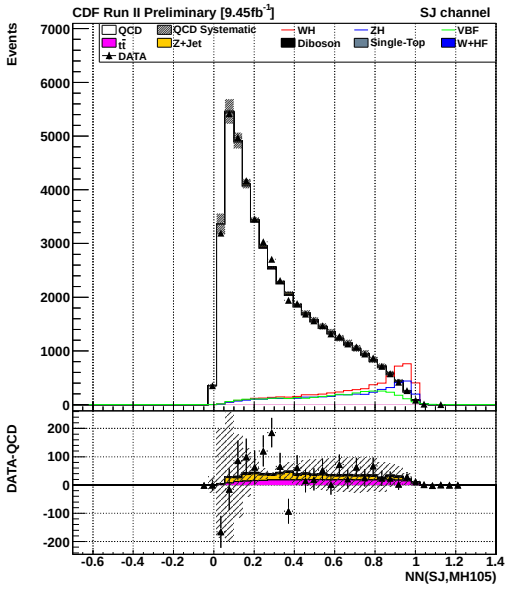

(b) MH105-SJ

Figure 98: Higgs-NN distribution for m_H=105 GeV/c^2. The left plot are from the SS b-tag category and the right plot is from the SJ b-tag category. All backgrounds are stacked and the superimposed Higgs signal is scaled by x1000. As the QCD background is large, plots of the DATA-QCD are plotted with stacked plot of non-QCD background and QCD systematic.

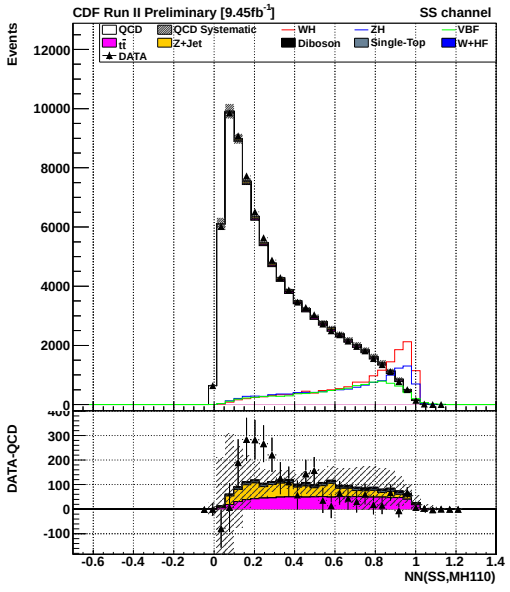

(a) MH110-SS

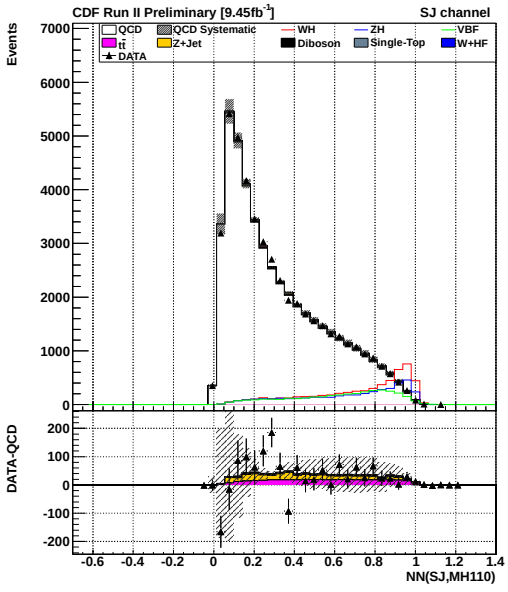

(b) MH110-SJ

Figure 99: Higgs-NN distribution for m_H=110 GeV/c^2. The left plot are from the SS b-tag category and the right plot is from the SJ b-tag category. All backgrounds are stacked and the superimposed Higgs signal is scaled by x1000. As the QCD background is large, plots of the DATA-QCD are plotted with stacked plot of non-QCD background and QCD systematic.

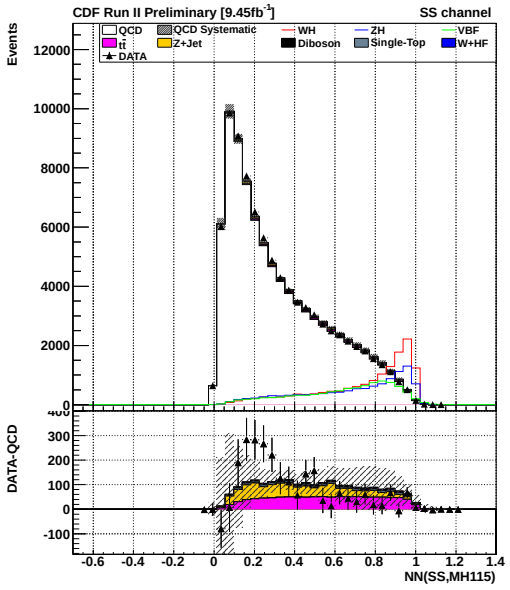

(a) MH115-SS

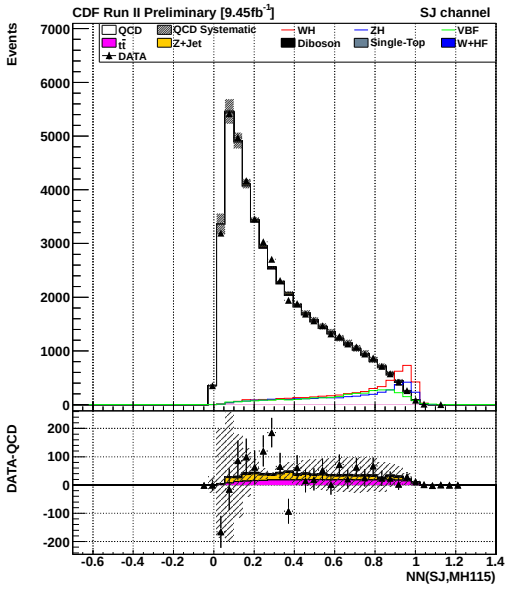

(b) MH115-SJ

Figure 100: Higgs-NN distribution for m_H=115 GeV/c^2. The left plot are from the SS b-tag category and the right plot is from the SJ b-tag category. All backgrounds are stacked and the superimposed Higgs signal is scaled by x1000. As the QCD background is large, plots of the DATA-QCD are plotted with stacked plot of non-QCD background and QCD systematic.

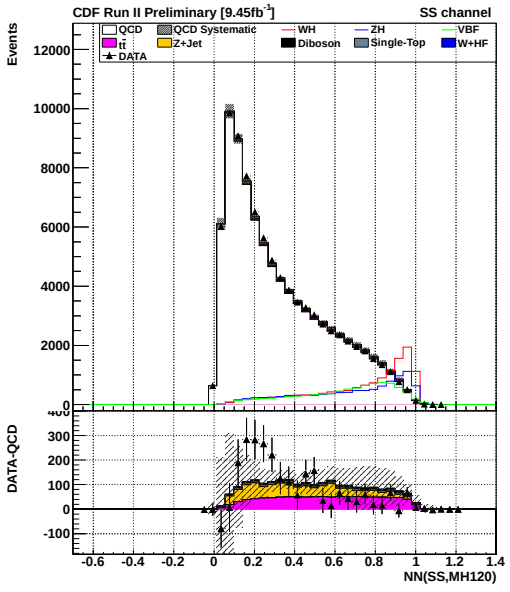

(a) MH120-SS

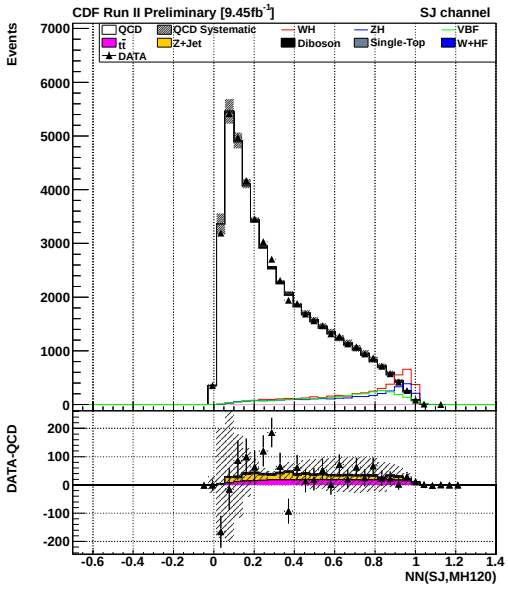

(b) MH120-SJ

Figure 101: Higgs-NN distribution for m_H=120 GeV/c^2. The left plot are from the SS b-tag category and the right plot is from the SJ b-tag category. All backgrounds are stacked and the superimposed Higgs signal is scaled by x1000. As the QCD background is large, plots of the DATA-QCD are plotted with stacked plot of non-QCD background and QCD systematic.

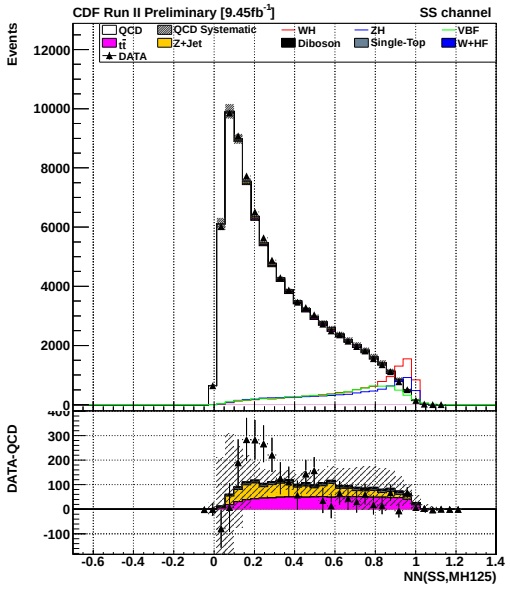

(a) MH125-SS

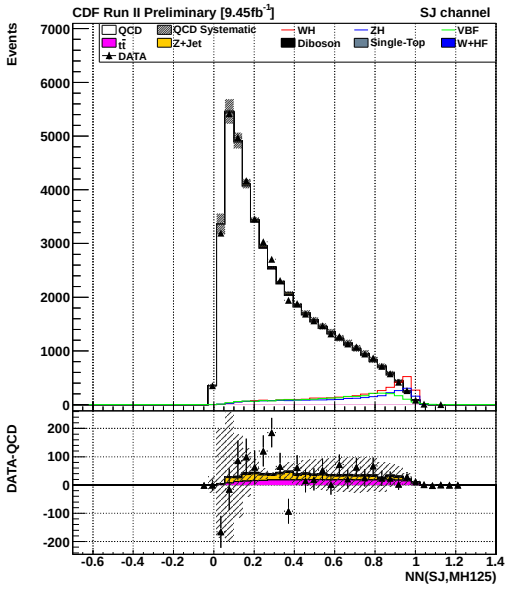

(b) MH125-SJ

Figure 102: Higgs-NN distribution for m_H=125 GeV/c^2. The left plot are from the SS b-tag category and the right plot is from the SJ b-tag category. All backgrounds are stacked and the superimposed Higgs signal is scaled by x1000. As the QCD background is large, plots of the DATA-QCD are plotted with stacked plot of non-QCD background and QCD systematic.

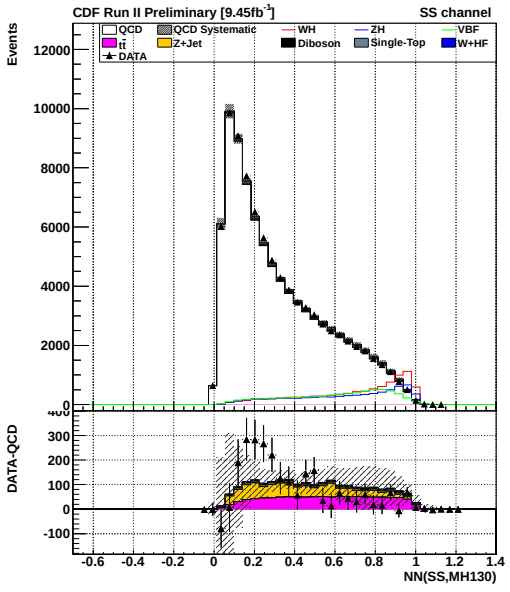

(a) MH130-SS

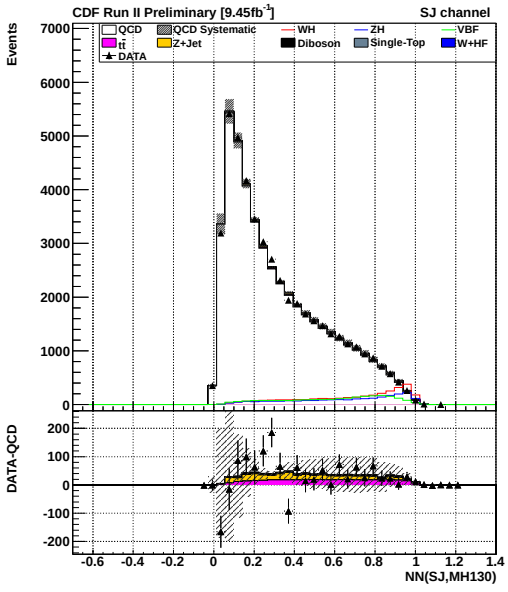

(b) MH130-SJ

Figure 103: Higgs-NN distribution for m_H=130 GeV/c^2. The left plot are from the SS b-tag category and the right plot is from the SJ b-tag category. All backgrounds are stacked and the superimposed Higgs signal is scaled by x1000. As the QCD background is large, plots of the DATA-QCD are plotted with stacked plot of non-QCD background and QCD systematic.

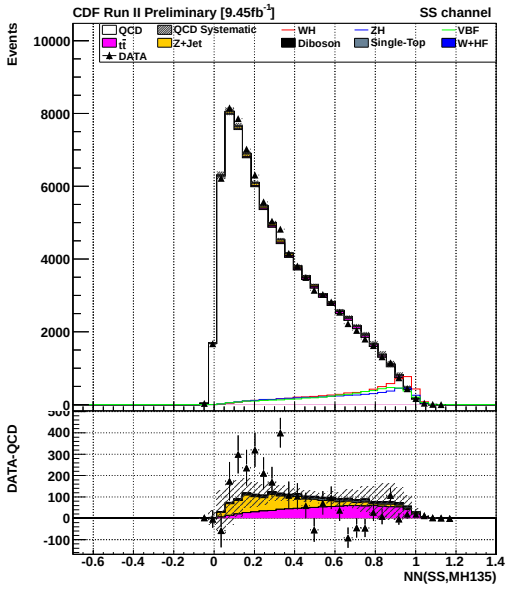

(a) MH135-SS

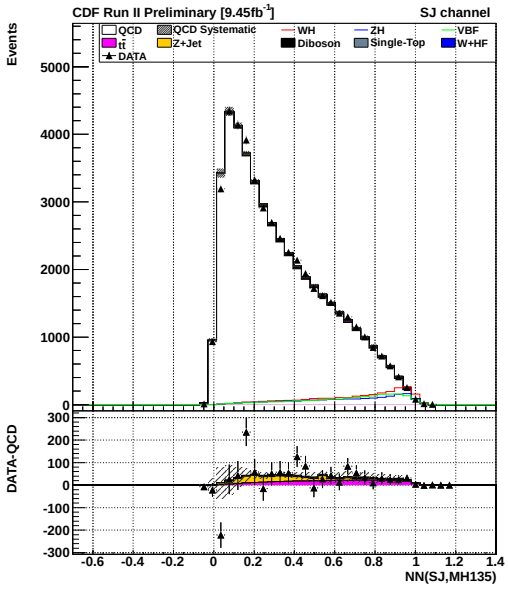

(b) MH135-SJ

Figure 104: Higgs-NN distribution for m_H=135 GeV/c^2. The left plot are from the SS b-tag category and the right plot is from the SJ b-tag category. All backgrounds are stacked and the superimposed Higgs signal is scaled by x1000. As the QCD background is large, plots of the DATA-QCD are plotted with stacked plot of non-QCD background and QCD systematic.

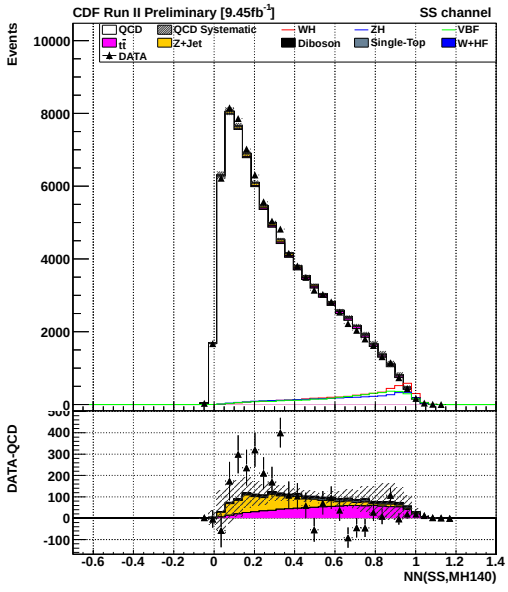

(a) MH140-SS

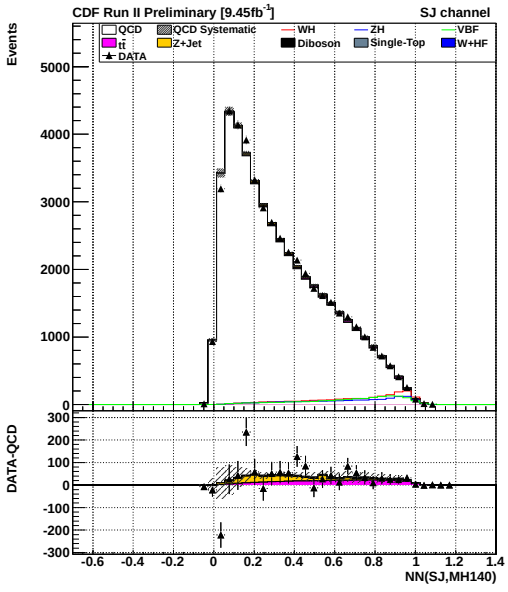

(b) MH140-SJ

Figure 105: Higgs-NN distribution for m_H=140 GeV/c^2. The left plot are from the SS b-tag category and the right plot is from the SJ b-tag category. All backgrounds are stacked and the superimposed Higgs signal is scaled by x1000. As the QCD background is large, plots of the DATA-QCD are plotted with stacked plot of non-QCD background and QCD systematic.

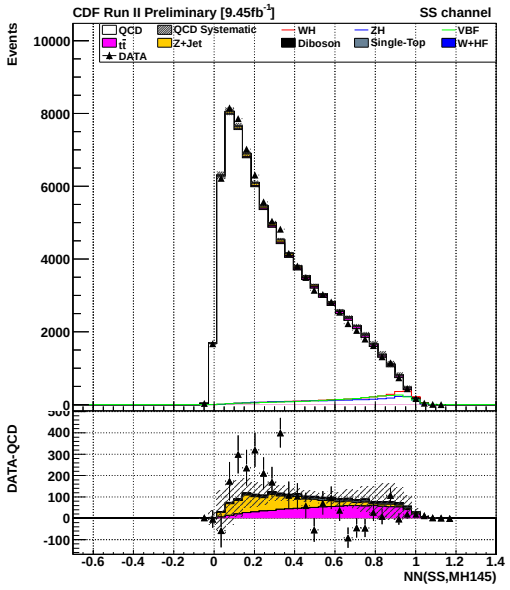

(a) MH145-SS

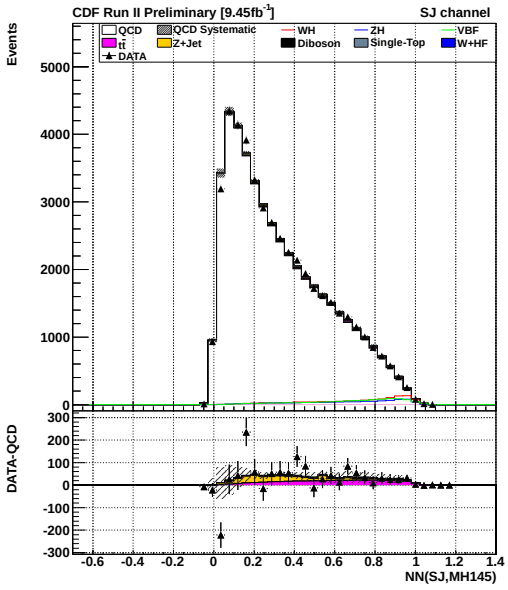

(b) MH145-SJ

Figure 106: Higgs-NN distribution for m_H=140 GeV/c^2. The left plot are from the SS b-tag category and the right plot is from the SJ b-tag category. All backgrounds are stacked and the superimposed Higgs signal is scaled by x1000. As the QCD background is large, plots of the DATA-QCD are plotted with stacked plot of non-QCD background and QCD systematic.

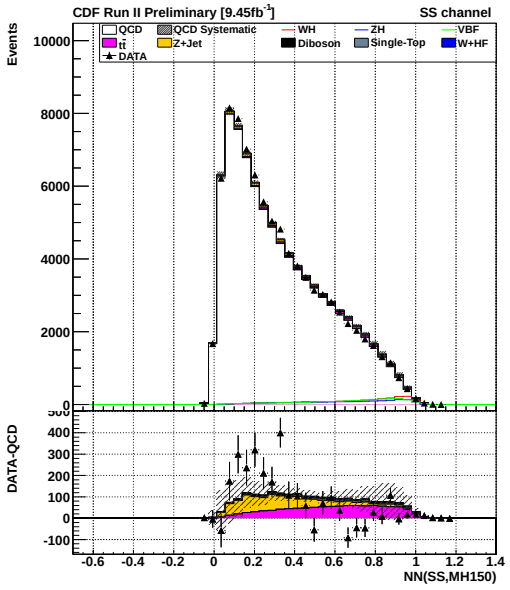

(a) MH150-SS

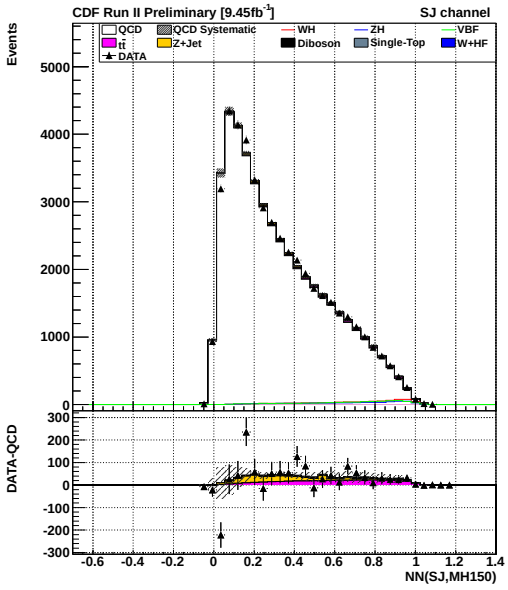

(b) MH150-SJ

Figure 107: Higgs-NN distribution for m_H=140 GeV/c^2. The left plot are from the SS b-tag category and the right plot is from the SJ b-tag category. All backgrounds are stacked and the superimposed Higgs signal is scaled by x1000. As the QCD background is large, plots of the DATA-QCD are plotted with stacked plot of non-QCD background and QCD systematic.

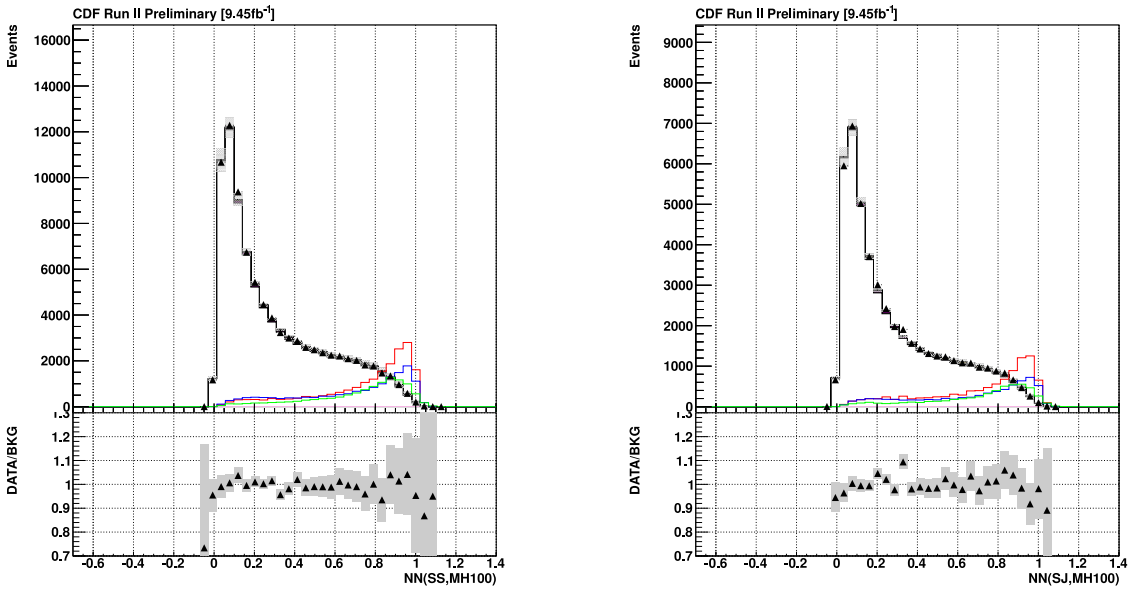

(a) MH100-SS (b) MH100-SJ

Figure 108: Higgs-NN distribution for m_H=100 GeV/$c^2$with a ratio plot of DATA/Total-Background to compare the shape of the background prediction with the DATA. The average ratio is ~ 1 which confirms the background models the data well.

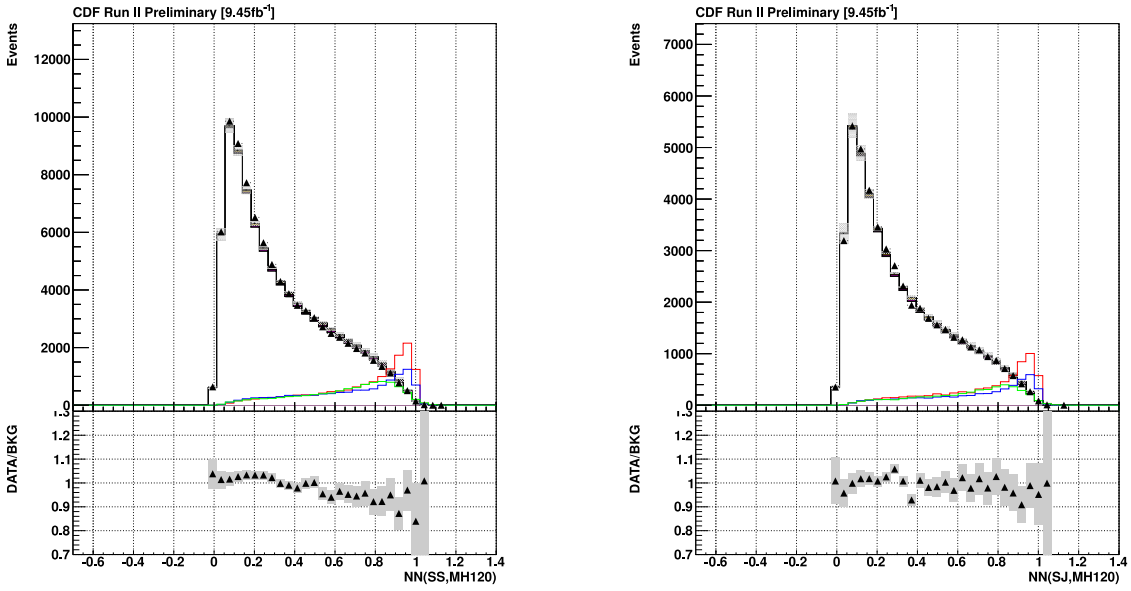

(a) MH120-SS (b) MH120-SJ

Figure 109: Higgs-NN distribution for m_H=120 GeV/$c^2$with a ratio plot of DATA/Total-Background to compare the shape of the background prediction with the DATA. The average ratio for SJ is ~ 1 for which confirms the background models the data well. However the SS distribution shows a slight over prediction of the background for NN>0.6 which results in a ratio $\lesssim 1.0$.

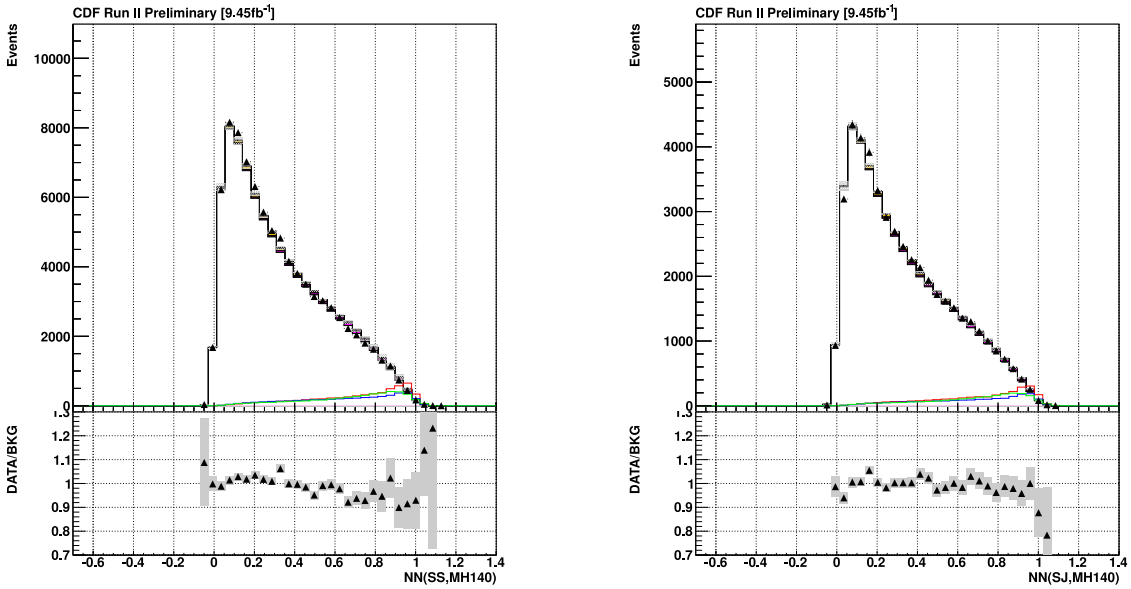

(a) MH140-SS (b) MH140-SJ

Figure 110: Higgs-NN distribution for m_H=140 GeV/$c^2$with a ratio plot of DATA/Total-Background to compare the shape of the background prediction with the DATA. The average ratio is $\sim$ 1 which confirms the background models the data well.

11 Results

No indication of a Higgs signal is observed in the data and 95% confidence limits (CL) are quoted. Table 11 has the limits from the combination of the SS and SJ channel plotted in figure 111. Tables 12 and 13 are limits for the SS and SJ channels, respectively with the limits plotted in figures 112 and 113. All the limits in the tables are normalised to the expected Higgs signal cross-section. Pseudoexperiment and observed posterior PDF distributions are available in section 13.2

Table 11: Summary of MCLimit for each Higgs mass from combining the SS and SJ channels

Higgs mass	-2σ	-1σ	Median	$+1\sigma$	$+2\sigma$	Observed
100	1.4	3.6	7.7	14.5	24.4	10.9
105	1.8	3.8	7.5	13.6	22.3	7.5
110	2.0	4.0	7.6	13.2	21.7	7.0
115	2.3	4.4	8.3	14.5	23.4	7.2
120	2.4	4.6	8.9	15.6	25.3	8.4
125	2.8	5.7	11.0	19.5	31.6	9.0
130	3.4	7.1	13.8	24.3	39.5	13.2
135	5.3	10.8	19.5	32.2	49.6	21.2
140	7.3	14.3	25.8	42.7	66.1	26.2
145	10.2	20.4	36.7	60.5	93.4	35.1
150	17.7	32.5	58.7	98.2	152.0	64.6

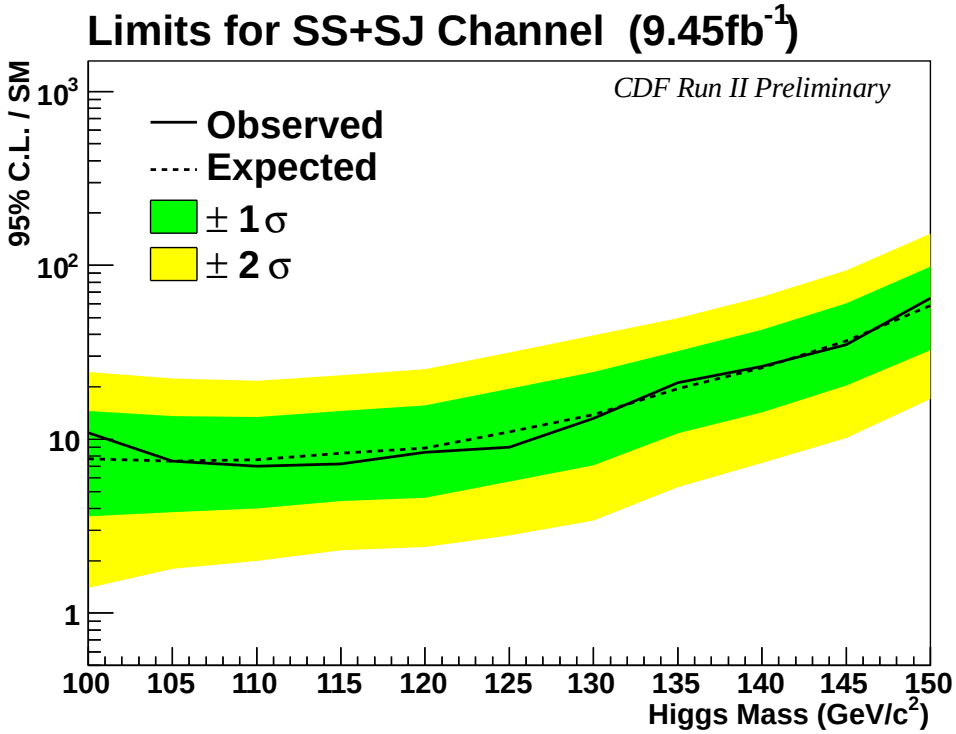

Figure 111: Limits for combined SS & SJ channels: The expected & observed limits are plotted as a function of the Higgs mass. The limits are normalised to the expected Higgs cross-section.

Table 12: Summary of MCLimit for each Higgs mass from combining the SS channels

Higgs mass	-2σ	-1σ	Median	$+1\sigma$	$+2\sigma$	Observed
100	3.6	6.7	10.9	16.6	23.7	15.9
105	4.3	6.7	10.1	14.9	21.2	8.2
110	4.6	6.7	9.8	14.2	20.1	8.3
115	4.8	7.3	10.8	15.5	21.7	8.9
120	5.3	7.8	11.6	16.8	23.6	10.2
125	6.4	9.5	14.0	20.4	29.0	11.6
130	8.2	12.2	18.3	26.8	38.1	14.6
135	12.4	18.4	27.3	39.5	55.6	25.6
140	17.0	24.8	36.5	52.7	74.1	34.8
145	23.9	35.1	51.6	74.1	103.9	50.9
150	39.6	57.7	84.3	121.0	167.6	84.1

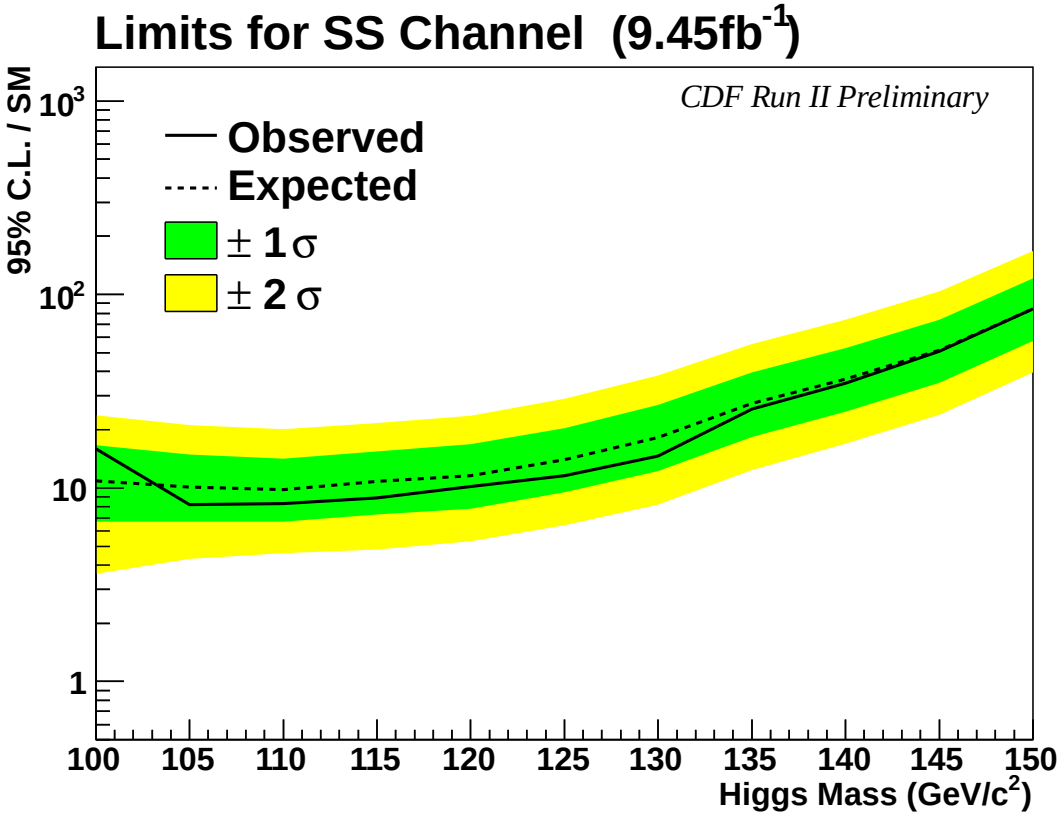

Figure 112: Limits for the SS channel: The expected & observed limits are plotted as a function of the Higgs mass. The limits are normalised to the expected Higgs cross-section.

Table 13: Summary of MCLimit for each Higgs mass from combining the SJ channels

Higgs mass	-2σ	-1σ	Median	$+1\sigma$	$+2\sigma$	Observed
100	7.8	10.9	15.5	22.0	30.6	12.2
105	8.7	12.2	17.3	24.5	34.2	15.0
110	8.4	11.7	16.7	23.5	32.5	13.8
115	9.3	12.7	17.9	25.2	35.1	14.7
120	10.3	14.3	20.3	28.9	40.3	15.4
125	12.7	17.6	25.1	35.5	49.3	19.4
130	16.2	22.4	32.2	46.1	65.1	24.7
135	18.6	25.6	36.2	50.8	70.2	26.1
140	24.1	32.9	46.3	65.3	90.7	33.9
145	34.8	47.6	67.0	95.2	130.6	48.0
150	56.0	76.1	104.8	142.9	185.6	78.2

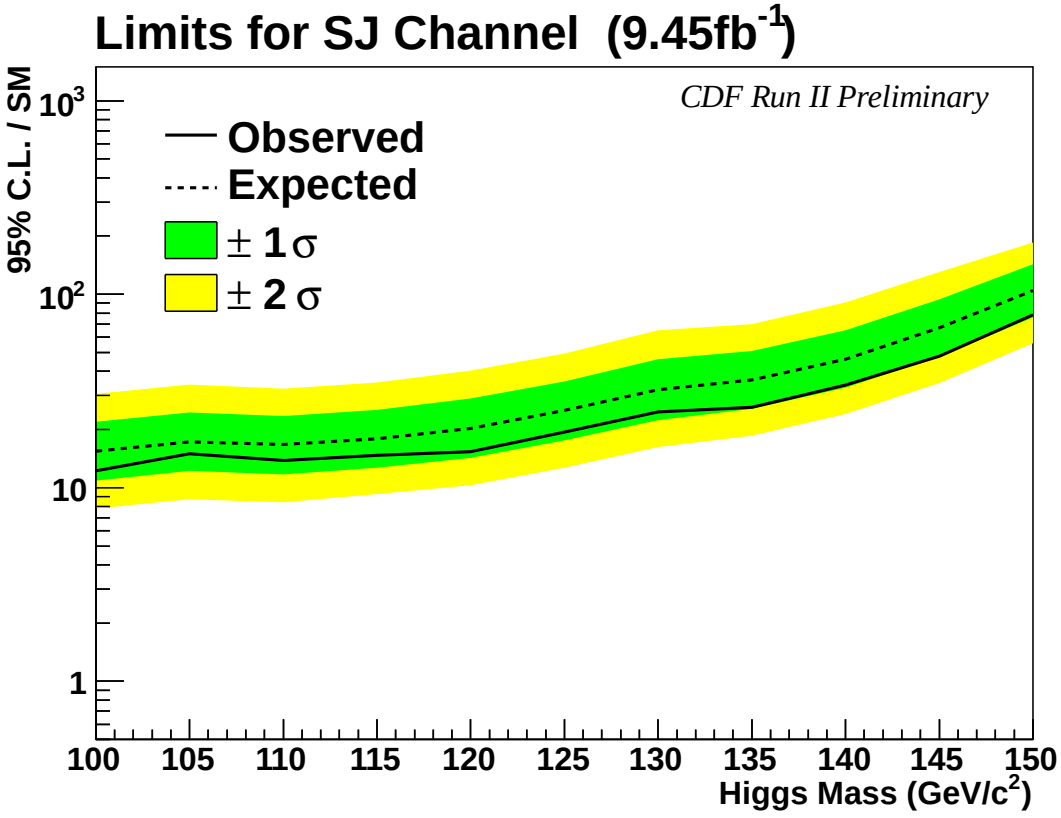

Figure 113: Limits for the SJ channel: The expected & observed limits are plotted as a function of the Higgs mass. The limits are normalised to the expected Higgs cross-section.

12 Conclusions

A search for the Higgs boson in the all hadronic mode was conducted using $9.45\,\mathrm{fb}^{-1}$of data. A Neural Network was used to separate the background events from the signal. As the presence of a Higgs signal was not observed, 95% confidence limits were calculated.

A number of improvements were included in this search which are:

- increase of analyzed data from $4\,\mathrm{fb}^{-1}$to $9.45\,\mathrm{fb}^{-1}$.
- improvements to the b-jet energy resolution
- new jet-width measurement
- improvements to QCD modeling (TRF).
- unification of VH and VBF signal regions
- more variables used in NN: result of improved TRF modeling
- improved NN training
- tuning of TRF NN output using information from control regions.

13 Appendix

13.1 Z+jets Generator Level Filter

The large cross-section for Z+jets would produce an extremely large number of events; of which many would be rejected by the trigger. A filter was devised to select events which were likely to pass the trigger.

- At generator level, select events with ≥ 1 b or c parton.
- ≥ 3 jets with $E_T >$ 5 GeV. The jets were defined by cone sizes of 0.4, 0.7 and 1.0.
- The Sum-$E_T$for the 0.4, 0.7 and 1.0 jets are calculated. Accept the event if any of these sums $\geq$ 60 GeV

13.2 Pseudoexperiment distributions and observed posterior PDF

The pseduoexperiment distributions used to extract the expected limits and the observed posterior PDF used to measure the observed limit are in this appendix.

13.2.1 SS channel

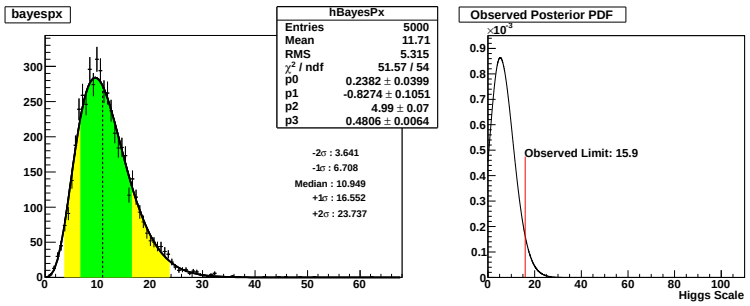

(a) MH100 - Expected (b) MH100 - Observed

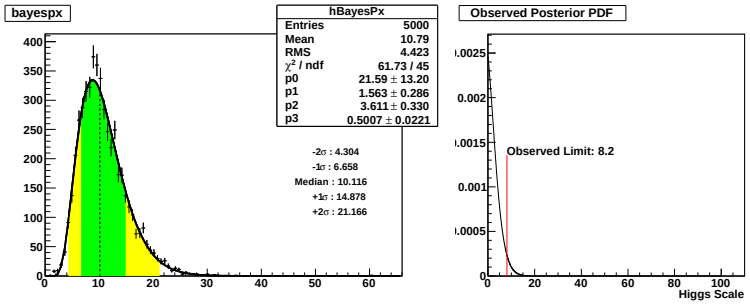

(c) MH105 - Expected (d) MH105 - Observed

Figure 114: Pseudoexperiment distributions and observed posterior PDF for the SS channel. The expected limits are taken from the pseudoexperiment distribution and the posterior PDF is used to measure the observed limit.

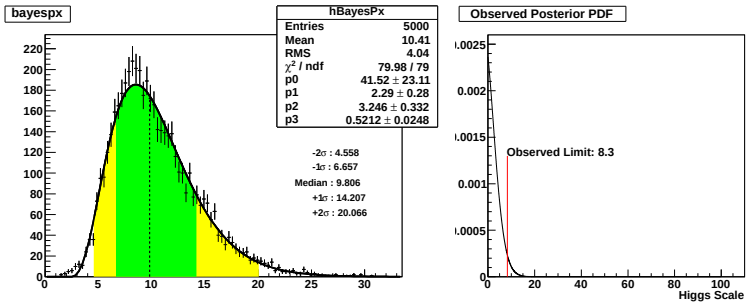

(a) MH110 - Expected (b) MH110 - Observed

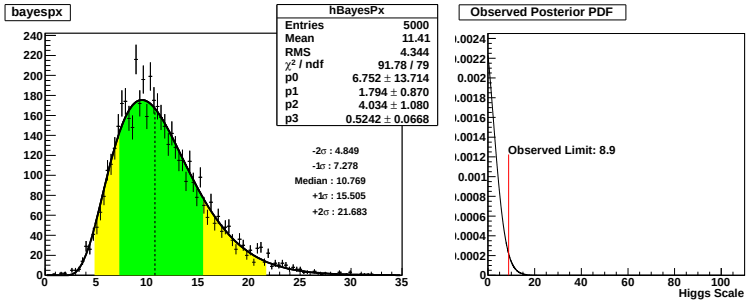

(c) MH115 - Expected (d) MH115 - Observed

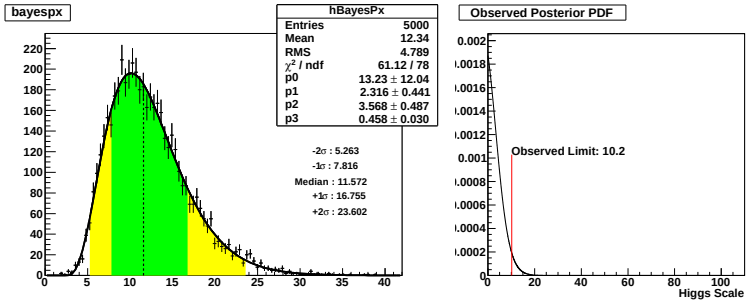

(e) MH120 - Expected (f) MH120 - Observed

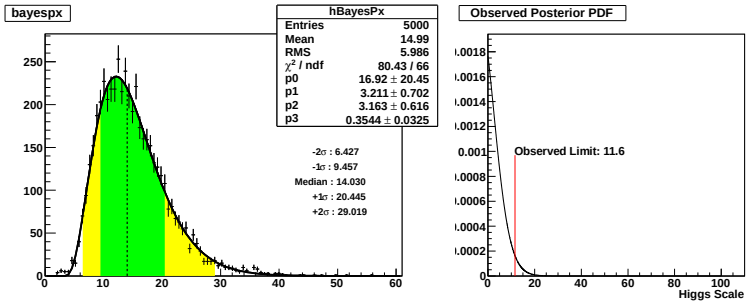

(g) MH125 - Expected (h) MH125 - Observed

Figure 115: Pseudoexperiment distributions and observed posterior PDF for the SS channel. The expected limits are taken from the pseudoexperiment distribution and the posterior PDF is used to measure the observed limit.

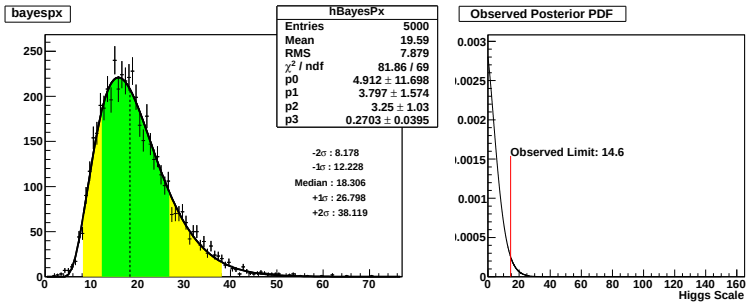

(a) MH130 - Expected (b) MH130 - Observed

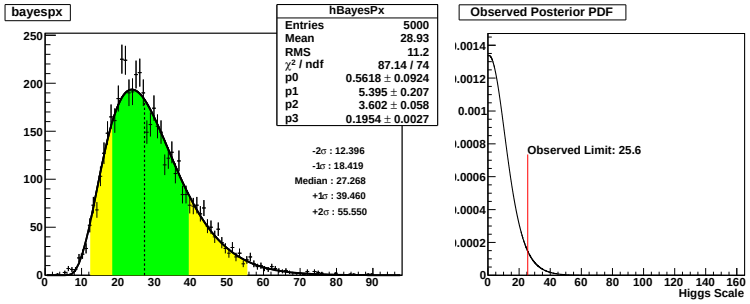

(c) MH135 - Expected (d) MH135 - Observed

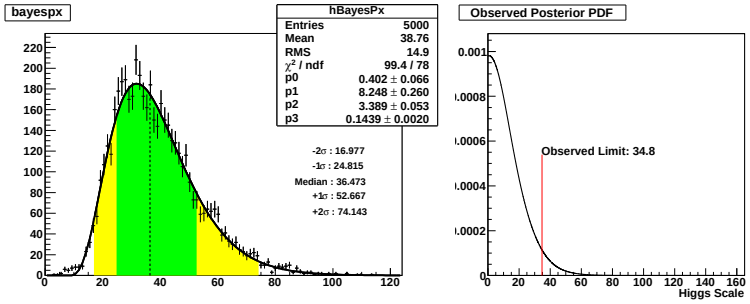

(e) MH140 - Expected (f) MH140 - Observed

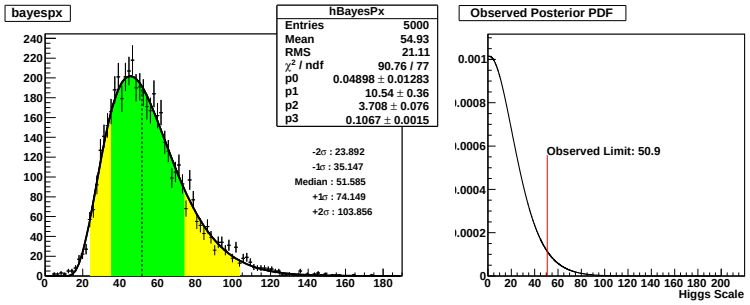

(g) MH145 - Expected (h) MH145 - Observed

Figure 116: Pseudoexperiment distributions and observed posterior PDF for the SS channel. The expected limits are taken from the pseudoexperiment distribution and the posterior PDF is used to measure the observed limit.

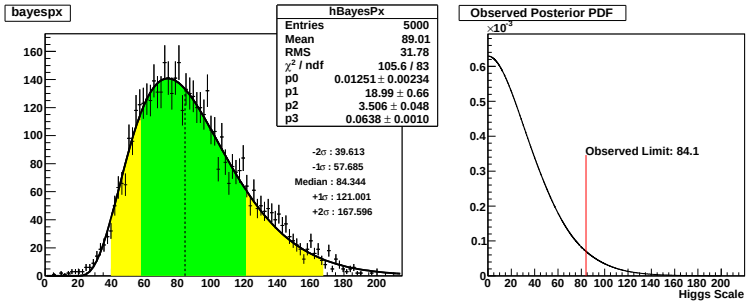

(a) MH150 - Expected (b) MH150 - Observed

Figure 117: Pseudoexperiment distributions and observed posterior PDF for the SS channel. The expected limits are taken from the pseudoexperiment distribution and the posterior PDF is used to measure the observed limit.

13.2.2 SJ channel

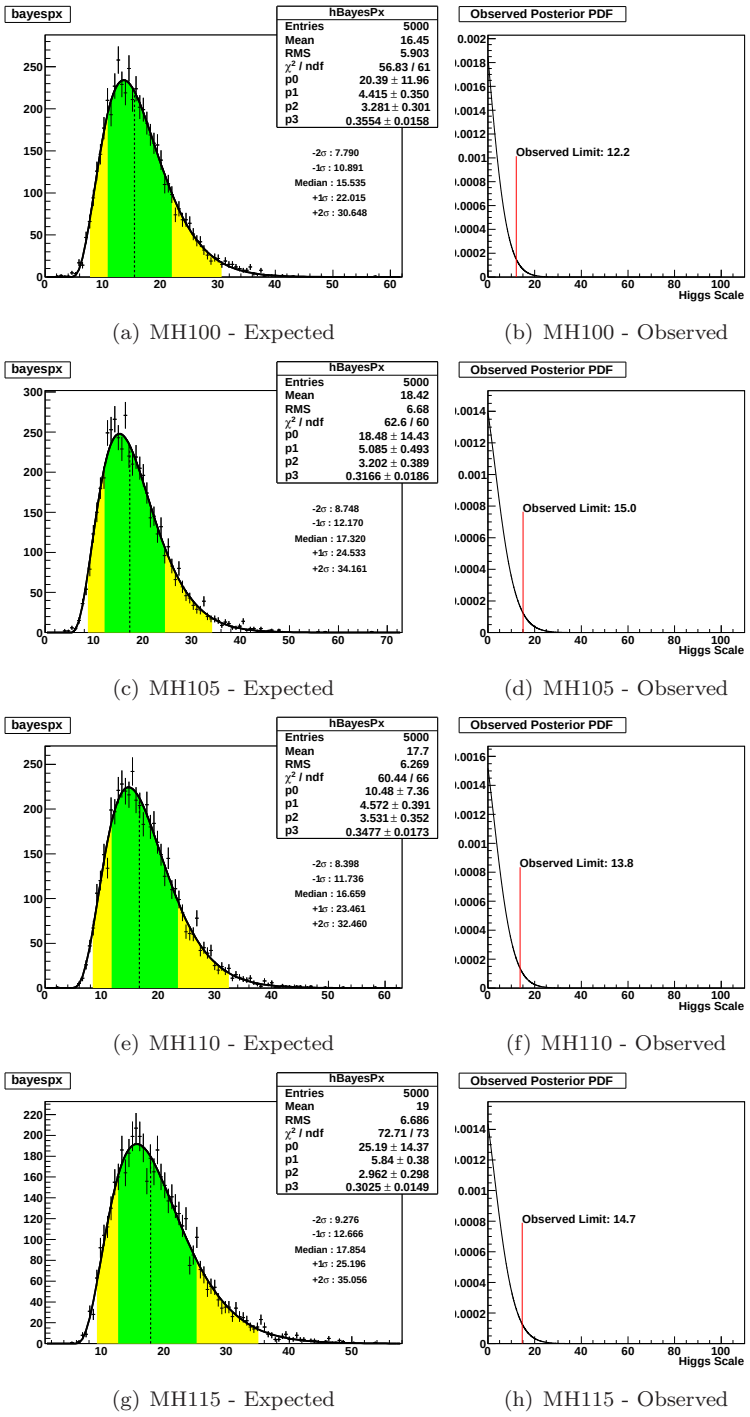

(a) MH100 - Expected (b) MH100 - Observed

(c) MH105 - Expected (d) MH105 - Observed

(e) MH110 - Expected (f) MH110 - Observed

(g) MH115 - Expected (h) MH115 - Observed

Figure 118: Pseudoexperiment distributions and observed posterior PDF for the SJ channel. The expected limits are taken from the pseudoexperiment distribution and the posterior PDF is used to measure the observed limit.

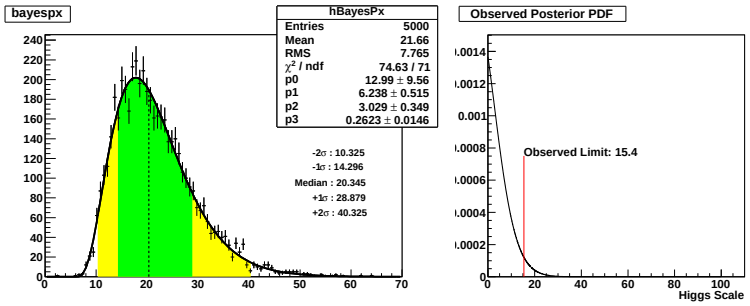

(a) MH120 - Expected (b) MH120 - Observed

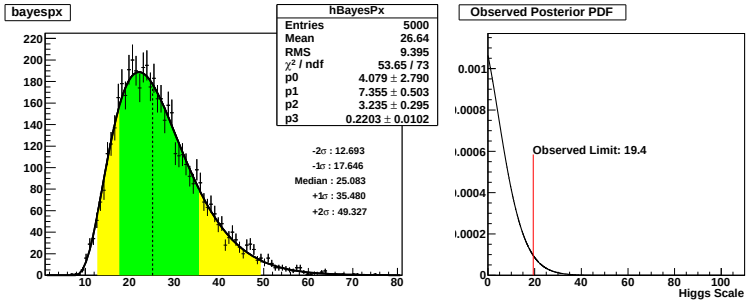

(c) MH125 - Expected (d) MH125 - Observed

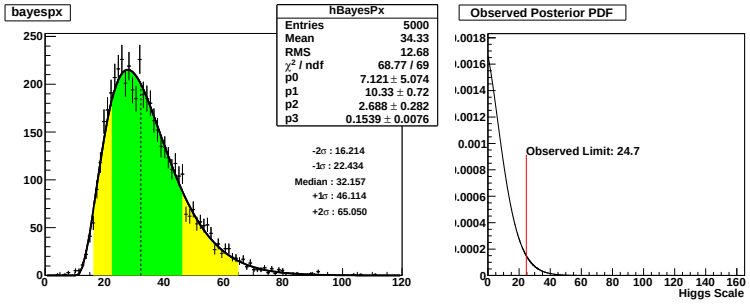

(e) MH130 - Expected (f) MH130 - Observed

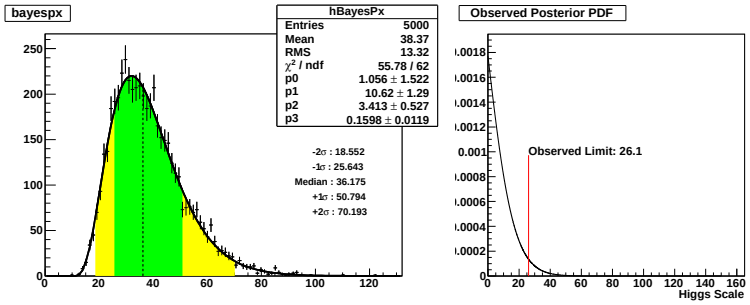

(g) MH135 - Expected (h) MH135 - Observed

Figure 119: Pseudoexperiment distributions and observed posterior PDF for the SJ channel. The expected limits are taken from the pseudoexperiment distribution and the posterior PDF is used to measure the observed limit.

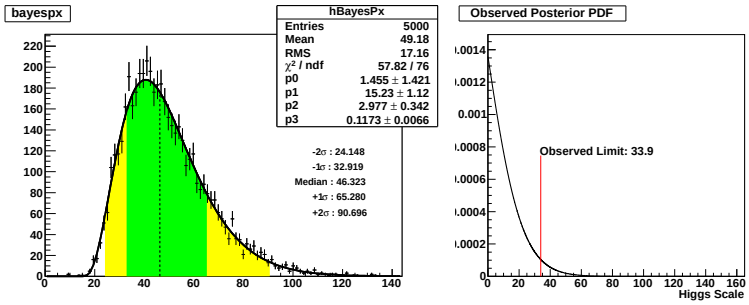

(a) MH140 - Expected (b) MH140 - Observed

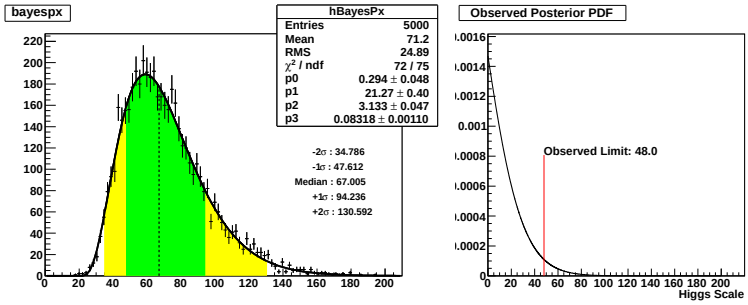

(c) MH145 - Expected (d) MH145 - Observed

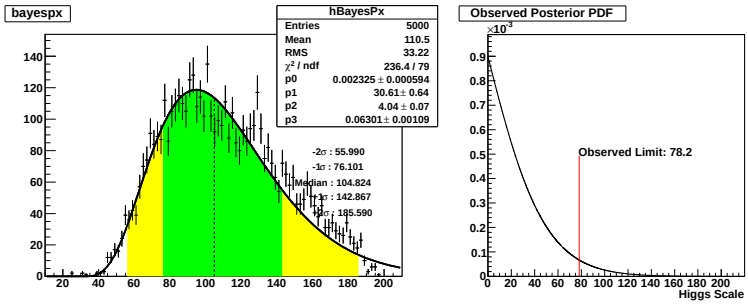

(e) MH150 - Expected (f) MH150 - Observed

Figure 120: Pseudoexperiment distributions and observed posterior PDF for the SJ channel. The expected limits are taken from the pseudoexperiment distribution and the posterior PDF is used to measure the observed limit.

13.2.3 SS+SJ channel

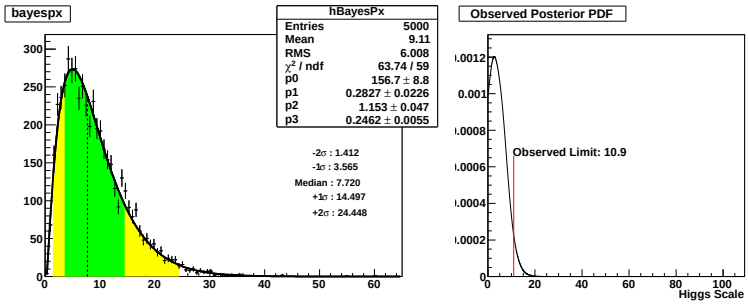

(a) MH100 - Expected (b) MH100 - Observed

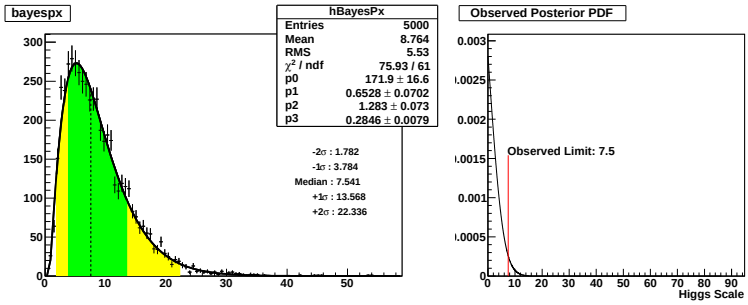

(c) MH105 - Expected (d) MH105 - Observed

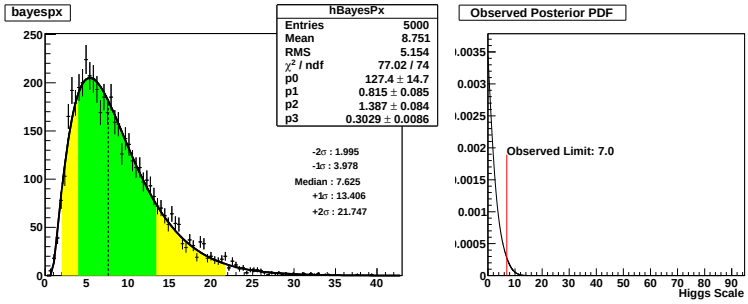

(e) MH110 - Expected (f) MH110 - Observed

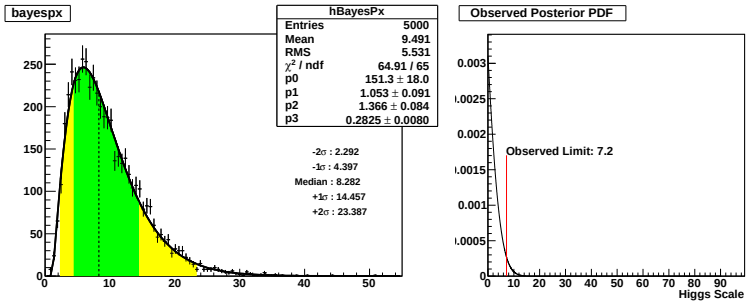

(g) MH115 - Expected (h) MH115 - Observed

Figure 121: Pseudoexperiment distributions and observed posterior PDF for the ALL channel. The expected limits are taken from the pseudoexperiment distribution and the posterior PDF is used to measure the observed limit.

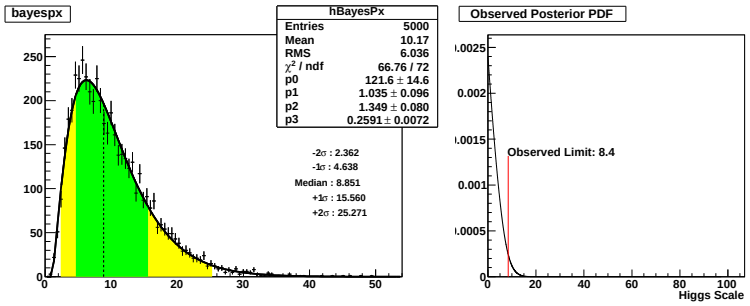

(a) MH120 - Expected (b) MH120 - Observed

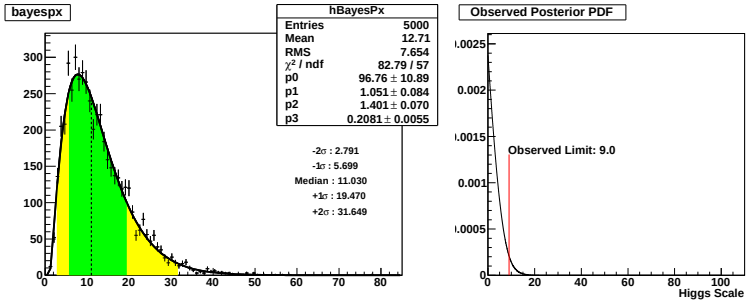

(c) MH125 - Expected (d) MH125 - Observed

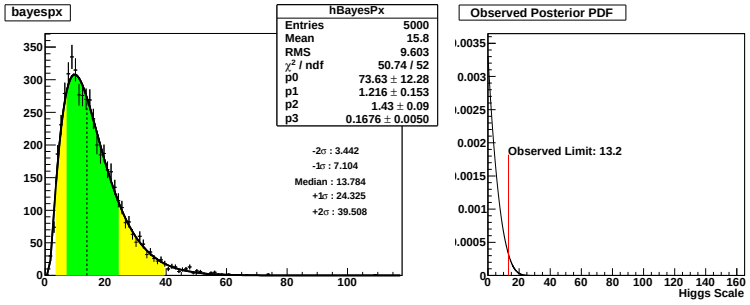

(e) MH130 - Expected (f) MH130 - Observed

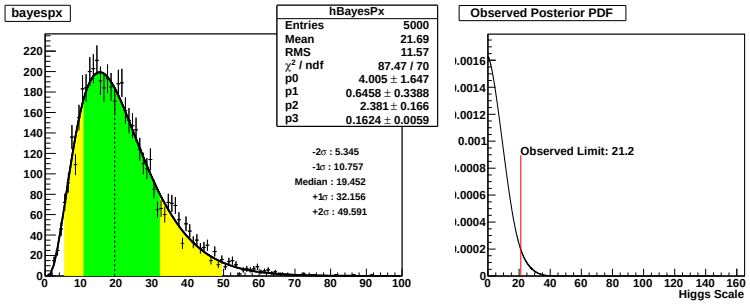

(g) MH135 - Expected (h) MH135 - Observed

Figure 122: Pseudoexperiment distributions and observed posterior PDF for the ALL channel. The expected limits are taken from the pseudoexperiment distribution and the posterior PDF is used to measure the observed limit.

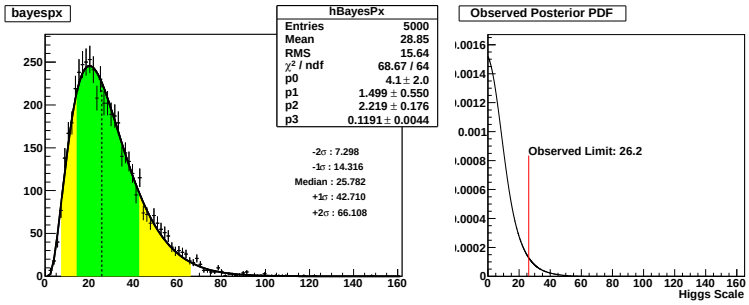

(a) MH140 - Expected (b) MH140 - Observed

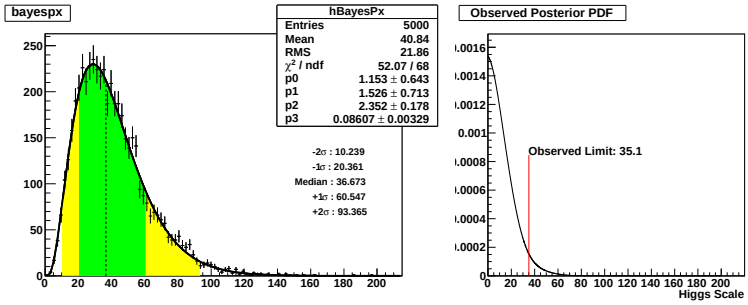

(c) MH145 - Expected (d) MH145 - Observed

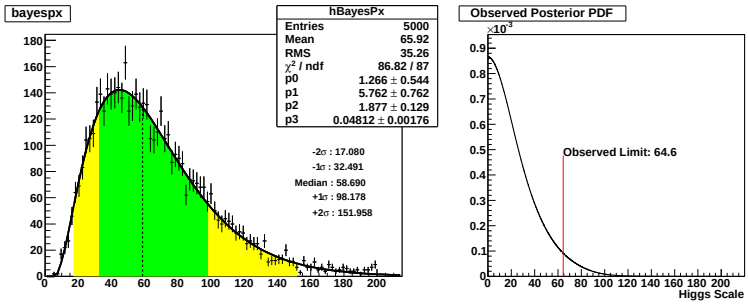

(e) MH150 - Expected (f) MH150 - Observed

Figure 123: Pseudoexperiment distributions and observed posterior PDF for the ALL channel. The expected limits are taken from the pseudoexperiment distribution and the posterior PDF is used to measure the observed limit.

References

[1] A. Djouadi, J. Kalinowski, and M. Spira. HDECAY: A program for Higgs boson decays in the standard model and its supersymmetric extension. *Comput. Phys. Commun.*, 108:56–74, 1998. 4

[2] Ankush Mitra, Shang-Yuu Tsai, and Song-Ming Wang. A search for the higgs boson in the all hadronic channel with data sample of $4\,\mathrm{fb}^{-1}$. CDF/ANAL/EXOTIC/CDFR 9955, Academia Sinica, December 2009. 4, 17, 18

[3] T. Aaltonen. Search for the higgs boson in the all-hadronic final state using the cdf ii detector". *Phys. Rev. D; Physical Review D*, 84(5), 2011. 4, 17

[4] Ankush Mitra, Shang-Yuu Tsai, and Song-Ming Wang. Study of multijet triggers for the all-hadronic higgs search. CDF/PHYS/TRIGGER/CDFR 9954, Institute of Physics, Academia Sinica, Taiwan, October 2009. 5

[5] Torbjorn Sjostrand, Leif Lonnblad, and Stephen Mrenna. PYTHIA 6.2: Physics and manual. 2001. hep-ph/0108264. 8

[6] Michelangelo L. Mangano, Mauro Moretti, Fulvio Piccinini, Roberto Pittau, and Antonio D. Polosa. ALPGEN, a generator for hard multiparton processes in hadronic collisions. *JHEP*, 07:001, 2003. 8

[7] Sebastian Grinstein and D Sherman. Secvtx scale factors and mistag matrices for the 2007 summer conferences. CDF/DOC/SEC_VTX/CDFR/ 8910, Harvard University, July 2007. 8

[8] The TEVNPH Working Group. Combined cdf and d0 upper limit on standard model higgs boson production with up to 8.6 fb−1 of data. FERMILAB-CONF-11-354-E 10606, 20 September 2011. 9

[9] Eric James. Private communication. 9

[10] Thomas Schwarz, Andrew Ivanov, and Robin Erbacher. Measurement of the top pair cross section in the lepton plus jets decay channel with 2.7 fb^{-1}. CDF/PUB/TOP/PUBLIC/ 9462, University of California, Davis, July 2008. 18

[11] A. Hocker et al. TMVA: Toolkit for multivariate data analysis. 2007. 41

[12] S. Geer and T. Asakawa. Analysis of multijet events produced at high energy hadron colliders. *Phys. Rev. D*, 53(9):4793–4805, May 1996. 43

[13] 2005. ISR/FSR Prescription : http://www-cdf.fnal.gov/internal/physics/joint_physics/agenda/20050527-minutes.html. 82